Titre: Title:	A geometallurgical approach for gravity separation for spodumene
Auteur: Author:	Teemu Laitinen
Date:	2025
Type:	Mémoire ou thèse / Dissertation or Thesis
Référence: Citation:	Laitinen, T. (2025). A geometallurgical approach for gravity separation for spodumene [Mémoire de maîtrise, Polytechnique Montréal]. PolyPublie. https://publications.polymtl.ca/68481/

POLYTECHNIQUE MONTRÉAL

affiliée à l'Université de Montréal

et

l'Université du Québec en Abitibi-Témiscamingue

A geometallurgical approach for gravity separation for spodumene

TEEMU LAITINEN

Département des génies civil, géologique et des mines

Mémoire présenté en vue de l'obtention du diplôme de *Maîtrise ès sciences appliquées*

Maîtrise en génie minéral - profil Recherche

Août 2025

POLYTECHNIQUE MONTRÉAL

affiliée à l'Université de Montréal

et

l'Université du Québec en Abitibi-Témiscamingue

Ce mémoire intitulé :

A geometallurgical approach for gravity separation for spodumene

présenté par **Teemu LAITINEN**

en vue de l'obtention du diplôme de *Maîtrise ès sciences appliquées*

a été dûment accepté par le jury d'examen constitué de:

Rahim BARZEGAR, président

Marc LEGAULT, membre et directeur de recherche

Jean-François BOULANGER, membre et codirecteur de recherche

Brian Kawenski COOK, membre externe

DEDICATION

I dedicate this thesis to my beloved grandmother Siiri.

Although she was nervous when I left alone for a new life abroad, she never stopped encouraging me. She always remembered me, celebrated my achievements, and often spoke about the day I would graduate. Sadly, she passed away before I could finish this work, but her support and pride have stayed with me through every step of this journey.

ACKNOWLEDGEMENTS

First and foremost, I would like to sincerely thank my supervisors, Professor Jean-François Boulanger and Professor Marc Legault, for their continuous guidance, support, and encouragement throughout this project. Their expertise has been invaluable at every stage of this thesis.

I am also deeply grateful to Darren Smith and Patrik Schmidt from Patriot Battery Metals, as well as Ryan Cunningham from Primero Group, for their collaboration, for providing access to drill core samples, and for their helpful insights.

Special thanks go to my best friend Neila Seray, whose geological knowledge and practical assistance greatly contributed to this work. I also wish to acknowledge the staff of URSTM, whose technical support and dedication ensured that all laboratory work could be conducted safely and effectively.

I would like to thank the Natural Sciences and Engineering Research Council of Canada (NSERC), the Chaire de recherche institutionnelle en géochimie environnementale des ressources minérales critiques et stratégiques, and Le Centre d'excellence sur les métaux stratégiques Éléments08 for their financial support of this research.

Finally, I extend my heartfelt appreciation to my family and friends for their unwavering support, patience, and belief in me throughout this outstanding journey.

RÉSUMÉ

Ce projet fut réalisé en collaboration avec Patriot Battery Metals Inc. et visait à développer un cadre géométallurgique pour évaluer le comportement du minerai de spodumène d'origine pegmatitique lors de la séparation gravimétrique. Une attention particulière a été portée à la description des carottes de forage et à la subjectivité inhérente aux observations géologiques, puisque les données produites par les géologues sont utilisées pour évaluer les performances des tests de séparation par liquide lourd (*heavy liquid separation ou HLS*). Étant donné que la HLS est étroitement liée à la séparation par milieu dense (*dense media separation ou DMS*), et que la taille des grains de spodumène montre une forte corrélation avec la récupération en HLS, on s'attend à ce que les performances du DMS puissent également être prédites à partir de l'analyse des carottes.

Comme l'entreprise capture déjà des images RGB haute résolution des carottes, cette étude vise en premier lieu à réduire la subjectivité des observations des géologues en appliquant des techniques de traitement d'image à ces visuels existants, limitant ainsi le besoin de travail manuel supplémentaire. Les images traitées ont été analysées à l'aide d'algorithmes d'apprentissage machine pour automatiser la détection et l'estimation de la taille des minéraux. Étant donné que la taille des grains a une influence directe sur la récupération au HLS, et par extension sur la performance du DMS, cette intégration de la description des carottes, de la géométallurgie, du traitement d'image et de l'apprentissage automatisé devrait améliorer la précision et l'efficacité de la caractérisation du minerai de spodumène. En fin de compte, le projet vise à optimiser les opérations de traitement du minerai.

Cette approche intégrée a conduit à plusieurs résultats notables. Le modèle d'apprentissage automatisé a permis de détecter et de quantifier la taille des grains de spodumène à partir d'images RGB des carottes avec une forte corrélation par rapport aux observations des géologues et aux résultats des tests HLS. Plus précisément, le diamètre équivalent moyen (d_{eq}) a montré une corrélation plus forte (R^2 = 79,72 %) avec la récupération de lithium que les estimations visuelles des géologues (R^2 = 71,78 %). De plus, l'analyse automatisée a permis de générer des courbes complètes de distribution granulométrique, ce qui était auparavant très fastidieux avec les méthodes traditionnelles. Ces distributions suivent bien les modèles classiques utilisés en fragmentation tels que ceux de Gates-Gaudin-Schuhmann et Rosin-Rammler, renforçant ainsi la crédibilité de la méthode automatisée. De plus, la méthode basée sur l'analyse d'image a fourni des estimations

plus fiables du pourcentage de spodumène par rapport aux observations de géologues, avec un coefficient de détermination presque deux fois plus élevé que celui obtenu par les estimations humaines. Ces résultats démontrent que l'apprentissage automatisé appliqué aux images de carottes peut améliorer la cohérence, l'objectivité et la précision quantitative des évaluations géologiques, constituant ainsi un outil précieux pour affiner les prédictions géométallurgiques du comportement du spodumène en traitement du minerai.

ABSTRACT

This project was conducted in collaboration with Patriot Battery Metals Inc. and focused on developing a geometallurgical framework for evaluating the behavior of spodumene pegmatite ore in gravity separation. A key emphasis was placed on drill core logging and the subjectivity inherent in geological observations, as the data produced by geologists was used to evaluate heavy liquid separation (HLS) test performance. Since HLS is closely related to dense medium separation (DMS), and spodumene grain size has shown a strong correlation with HLS recovery, it is expected that DMS performance could also be predicted from drill core analysis.

As the company already captures high-resolution RGB-images of drill cores, this study aims to reduce subjectivity in logging by applying image processing techniques to these existing visuals, eliminating the need for additional manual work. The processed images are analyzed using machine learning algorithms to automate the detection and size estimation of mineral grains. Since grain size has a direct influence on HLS recovery, and by extension, DMS performance, this integration of core logging, geometallurgy, image analysis, and machine learning is expected to enhance the accuracy and efficiency of spodumene ore characterization. Ultimately, the project seeks to optimize mineral processing operations.

This integrated approach led to several notable findings. The machine learning model was able to detect and quantify spodumene grain sizes from RGB drill core images with strong correlation to HLS test results. Specifically, the mean equivalent area diameter of spodumene grains showed a stronger correlation (R^2 = 79.72%) with lithium recovery than geologists' visual estimates (R^2 = 71.78%). Moreover, machine-based analysis enabled the generation of full grain size distribution curves – a tedious task in traditional core logging. These distributions were well-fitted with classical crushing models such as Gates-Gaudin-Schuhmann and Rosin-Rammler, increasing the credibility of the automated method. Additionally, the image-based method provided more reliable spodumene percentage estimations compared to manual logging, with a coefficient of determination nearly double that of human estimates. The results collectively demonstrate that machine learning, when applied to drill core images, can enhance the consistency, objectivity, and quantitative resolution of geological assessments, providing a valuable tool for improving geometallurgical predictions of spodumene processing behavior.

PREFACE

As part of this master's project, the main objective was to develop a geometallurgical framework for predicting spodumene behavior in gravity separation processes based on drill core data and high-resolution images using machine learning algorithms. The author of this thesis has been actively involved in the field of mineral processing through several related studies and contributions, exploring analytical and predictive techniques for spodumene and lithium mineralogy beyond the scope of this thesis. The key outcomes include:

Scientific article (testwork conducted as part of an internship at UQAT in summer of 2023):

Laitinen, T., Legault, M., Ojala, S., & Boulanger, J. (2024). "Assessment of Time-Gated Raman Spectroscopy for Online Mineralogy of a Spodumene Ore. Journal of Raman Spectroscopy. https://doi.org/10.1002/jrs.6748

Oral presentation:

The above article was presented at the 35th annual CMPNOQ conference (Rouyn-Noranda, fall 2023), where the presentation was awarded best master's level presentation.

Technical report:

A report based on the article was awarded **first prize** in the Lucky Amaratunga Student Technical Report Competition at the 56th annual CMP 2024 conference (Ottawa, January 2024).

Poster presentation:

Laitinen, T., Legault, M., & Boulanger, J. (2025). Automating mineral grain analysis in drill cores using machine learning for geometallurgical applications. Poster presented at the 57th annual CMP 2025 conference, Ottawa, Canada.

Together, these contributions reflect a coherent effort to develop and share spodumene ore characterization and processing using innovative analytical and machine learning approaches.

TABLE OF CONTENTS

LIST OF TABLES

LIST OF FIGURES

LIST OF SYMBOLS AND ABBREVIATIONS

Area	Projected two-dimensional grain area (mm^2)
BWI	Bond Work Index
CART	Classification and Regression Tree
D_{10}	Grain size at which 10% of the sample volume is finer (mm)
D_{50}	Grain size at which 50% of the sample volume is finer (mm)
D_{90}	Grain size at which 90% of the sample volume is finer (mm)
DMC	Dense Media Cyclone
DMS	Dense Media Separation
d_{Fmax}	Maximum Feret diameter (greatest boundary-to-boundary distance) (mm)
d_{ins}	Maximum inscribed circle diameter within a grain (mm)
d_{eq}	Equivalent area diameter; diameter of a circle with the same area as the grain (mm)
GGS	Gates-Gaudin-Schuhmann (distribution model)
HLS	Heavy Liquid Separation
h_{rec}	Height of the bounding rectangle enclosing a grain (mm)
ICP	Inductively Coupled Plasma
ICP-MS	Inductively Coupled Plasma Mass Spectrometry
k-NN	k - Nearest Neighbor
l_{ell}	Length of the major axis of the best-fit ellipse (mm)
LST	Lithium Heteropolytungstate (heavy liquid used in HLS)

MATLAB	Matrix Laboratory (numerical computing software)
ML	Machine Learning
Na_6	Sodium compound (e.g., in albite or sodium minerals)
PBM	Patriot Battery Metals
P_{80}	Particle size below which 80% of the total sample mass is contained (mm)
q_1, q_2	Generic variables used in mathematical equations
R^2	Coefficient of determination (measure of model fit)
RF	Random Forest
ROI	Region of Interest (in image analysis)
RQD	Rock Quality Designation
RRS	Rosin-Rammler-Sperling (distribution model)
SAG	Semi-Autogenous Grinding
s_{ell}	Length of the minor axis of the best-fit ellipse (mm)
SLIC	Simple Linear Iterative Clustering (superpixel algorithm)
TIMA	TESCAN Integrated Mineral Analyzer
UCS	Uniaxial Compressive Strength
URSTM	Unité de Recherche et de Service en Technologie Minérale
VDSR	Very Deep Super Resolution
w_{rec}	Width of the bounding rectangle enclosing a grain (mm)
XRD	X-ray Diffraction
XRF	X-ray Fluorescence

LIST OF APPENDICES

CHAPTER 1 INTRODUCTION

1.1 PROBLEM STATEMENT

Mining and exploration companies operating at the exploration stage benefit greatly from fast and reliable methods for mineralogical quantification. Traditionally, exploration work involves drilling and the subsequent visual assessment of drill cores by geologists. This assessment can be supported by so-called light analytical techniques, such as image analysis or other scanning methods, to determine which minerals are present based on characteristics like color or texture. However, visual estimates of parameters such as grain size or the number of mineral grains, can be subjective and prone to variation between geologists. For example, one common way to do core logging is for geologists to estimate the percentage of certain minerals and their grain size. However, this process introduces two potential sources of bias. First, the estimated proportion of minerals will vary depending on the observer. Second, since not every single geologist measurement can be made using a ruler, the size of the mineral grains can itself be subjectively determined: what one geologist observes as 6 mm, another might estimate to be 7 mm or even 10 mm. These combined inconsistencies can significantly affect the quality of the logging data and, consequently, the decisions made in subsequent stages of the project. While advanced mineralogical methods (e.g., XRD or SEM analyses) can provide more accurate information, these are often time-consuming and costly, especially during early exploration when many samples are evaluated.

Industrial-scale separation of spodumene is typically done using dense media separation (DMS), but its application at test scale is impractical due to the large sample size required. Instead, heavy liquid separation (HLS) tests offer a more feasible alternative for laboratory settings, requiring smaller sample volumes. However, little remains known about how spodumene grain size affects liberation and, in turn, HLS and DMS performance. Hence, to support geometallurgical model developmenent, there is a need to find links between mineralogical data such as spodumene grain size, liberation and specific gravity-based separation performance.

1.2 RESEARCH OBJECTIVES

The primary objective of this research is to improve the understanding of how mineralogical and geological characteristics influence spodumene gravity separation, enabling geometallurgical predictions. The study focuses on drill core samples from Patriot Battery Metals' CV5 lithium pegmatite deposit. The aim is to establish a foundation for predicting the outcomes of metallurgical tests using geological data and/or cost-effective laboratory tests combined with modern machine learning (ML) tools.

To achieve this main objective, three sub-objectives are identified as follows:

1. Establish the link between drill core data and HLS test results.
2. Identify and validate simple tests for prediction of the outcome of HLS tests.
3. Investigate the potential of machine learning based image analysis in improving the consistency and accuracy of visual core logging.

The approach of this research is also summarized in Figure 1.1.

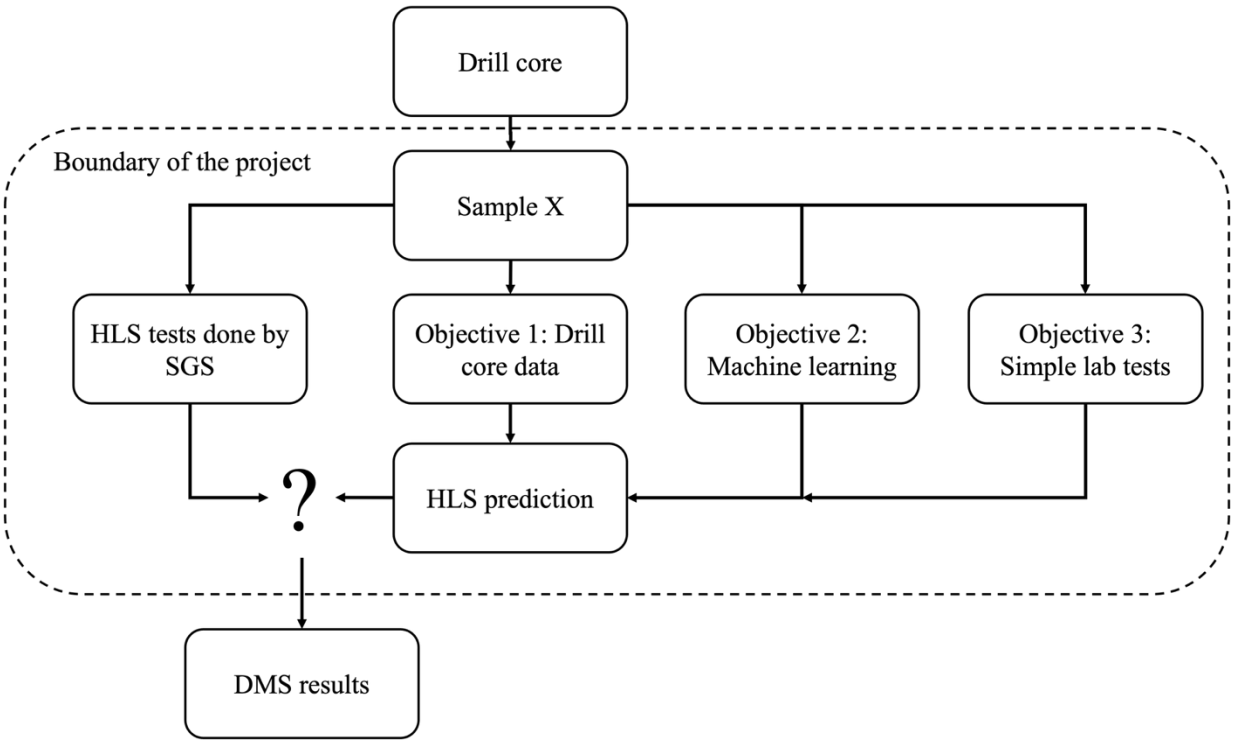

Figure 1.1 Approach of the thesis project.

1.3 HYPOTHESIS AND RESEARCH QUESTION

The hypotheses underpinning this work are as follows:

- Drill core features, such as grain size, color, and texture, are correlated with HLS results.
- A machine learning model based on RGB drill core images can reliably detect, quantify and characterize spodumene grains size.
- Grain size and liberation largely drive specific gravity-based separation performance.

The main research question addressed in this thesis is:

Can better drill core data acquisition methods be used to better predict the gravimetric separation of lithium?

1.4 THESIS STRUCTURE

This chapter (Chapter 1) presents an overview of the problem statement of this thesis and explains the objectives and hypotheses, including the formal research question. Chapter 2 provides a literature review on the topics of geometallurgy of lithium ores and spodumene beneficiation methods, focusing on gravimetric separation. An overview of basic machine learning models and image processing techniques is also presented. Chapter 3 presents the materials and methods used to conduct laboratory test work containing crushing and HLS testing as well as the creation of the ML algorithm for mineral grain identification and grain size estimation. Chapter 4 then covers the obtained results from the laboratory test work, and the achievements of the ML models in terms of mineral grain characterization and geometallurgical implications. Finally, chapter 5 summarizes and concludes the results of this research work and suggests some recommendations for the future.

CHAPTER 2 LITERATURE REVIEW

In modern times, humankind has conquered new fields of study and technology to address global challenges and crises. The greatest threats to Earth are said to be climate change, biodiversity loss, plastic pollution, and deforestation (15 Biggest Environmental Problems of 2024). Groundbreaking technologies, such as Li-ion batteries and various applications of artificial intelligence, have made significant steps in recent years to tackle these issues. However, a common factor for all these technologies and challenges is the need for raw materials, such as lithium, which act as a bridge between brilliant ideas and practical implementation, enabling innovative progress towards the future.

Elemental lithium (Li) belongs to the alkali metals group (Jeppson et al., 1978), which is located on the left side of the periodic table. Lithium is known to be the lightest metal, with only half the density of water (Hodgman et al., 2014). The lithium atom consists of 3 protons, 3 electrons and 4 neutrons resulting in an atomic mass of 6.9410 u (Jeppson et al., 1978). Due to its atomic structure (only 1 electron on “s” orbital), lithium tends to easily lose the electron and thus it easily reacts with anions forming both organic and inorganic compounds (Jeppson et al., 1978).

In its pure form, lithium is a silver white and soft metal (Jeppson et al., 1978; Tadesse et al., 2019). At room temperature, lithium appears as a solid. It has a melting point of 180,54 °C and a boiling point of 1347 °C (Hodgman et al., 2014). Lithium is also flammable and when exposed to sufficient heat, burning with a red flame (Koch & Jennings-White, 2009).

Lithium has long been used for various applications. Traditional usages of lithium have been the glass and ceramic industry as well as grease/casting covering over 30% of lithium usage in 2011 (Bae & Kim, 2021; Meshram et al., 2014). The first commercial lithium-ion battery was built in 1991, and the number of battery applications have increased rapidly ever since (Bae & Kim, 2021). The consumption of lithium-ion batteries has more than doubled in the last 8 years due to the recent growth in demand for lithium applications, such as EV and ESS as well as other electronics (Bae & Kim, 2021). Figure 2.1 represents the lithium usage in different sectors in 2023.

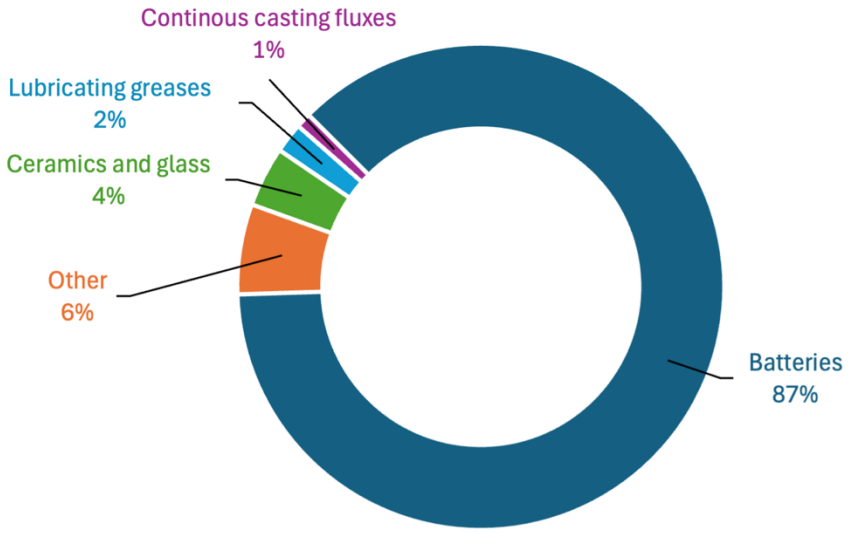

Figure 2.1 Estimated global market for lithium in various sectors for the 2023. Data is taken from (Natural Resources Canada, 2025)

As discussed above, Li easily forms inorganic compounds and therefore pure elemental Li is not found in nature. Therefore, common lithium bearing minerals such as spodumene, petalite, amblygonite and lepidolite are the main sources of Li emanating from hard rock deposits (Bulatovic, 2015; Tadesse et al., 2019). Other Li-bearing minerals such as zinnwaldite, eucryptite and triphylite are also stated in the literature (Colton, 1957; Grosjean et al., 2012).

The coarse-grained hard rock deposits commonly exploited for lithium are also known as pegmatite deposits and constitute the major source of lithium (USGS, 2025). Lithium can also be found in brines and sedimentary rock deposits (Marcinov et al., 2023). The distribution between different resources is presented Figure 2.2a. Lithium brines, commonly found in salt lakes, are a major source of lithium and have historically accounted for 59–62% of global production (Grosjean et al., 2012; Tadesse et al., 2019). However, in recent years, hard rock sources have become increasingly important in terms of production, despite brines still representing the largest global lithium resource (Marcinov et al., 2023).

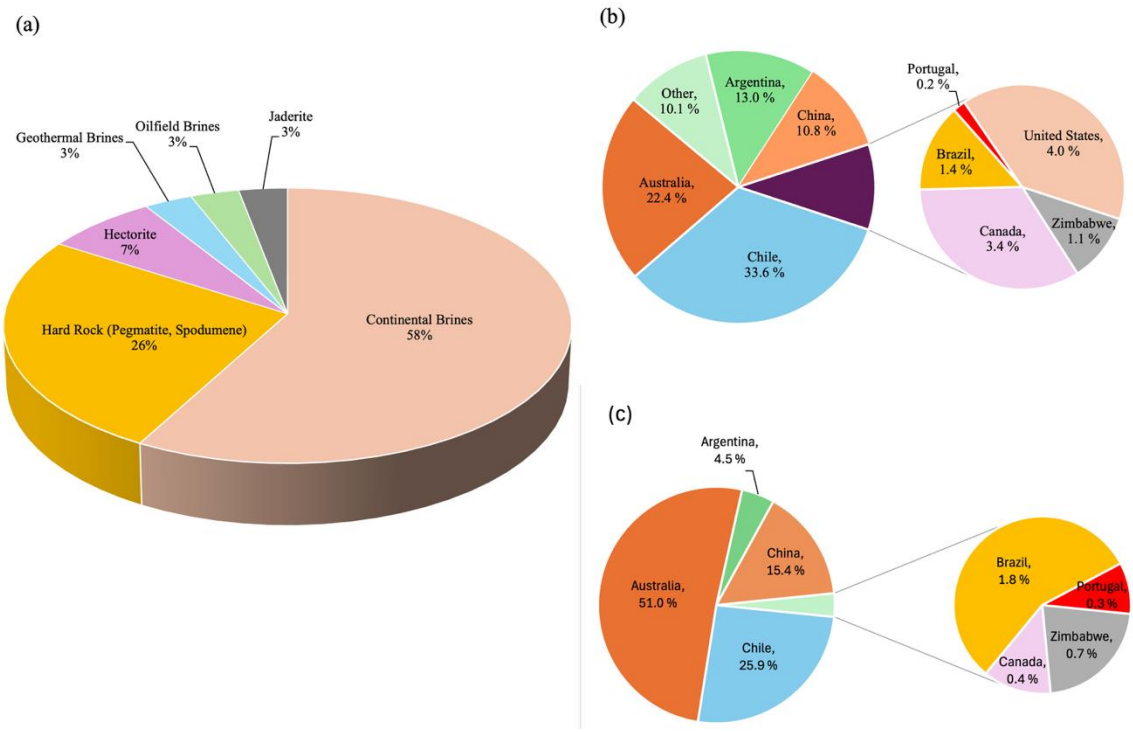

Figure 2.2 (a) Distribution of different deposit types (Gutiérrez et al., 2022), (b) Distribution of lithium wealth (Natural Resources Canada, 2025), (c) Distribution of production of lithium (Natural Resources Canada, 2025).

As presented in Swain (2017), lithium extraction from hard rock deposit minerals (such as spodumene) can be done in three different ways depending on the ore type and the mineral in question. Following the physical separation of lithium-bearing minerals, the produced concentrate is often treated by using a combination of chemical and pyrometallurgical processes (May et al., 1980; Swain, 2017). The most common combinations are roasting/calcination or a chlorination process resulting in the overall Li-recovery of > 85% (Swain, 2017). The second way of extracting lithium is to use pressure leaching. As reported by Zhou et al. (2024) using nitric acid pressure leaching in 1L titanium autoclave, the extraction efficiency and reaction kinetics were improved, resulting up to 95% Li-recovery. Unlike extractive metallurgy and pressure leaching, bioleaching, as the third approach for Li extraction, is an attractive option due to the cost, environmental, and energy efficiency of the process. The downside of this method, on the other hand, is the extremely slow reaction kinetics (Swain, 2017). All three of these methods depend on the production of a high-grade spodumene concentrate (typically >5.5-6% Li_2O, corresponding to 68-75% spodumene).

Lithium resources and production are unevenly distributed. According to Stringfellow & Dobson (2021), the primary commercial hard-rock sources are in Australia and China, while major brine production occurs in Argentina, Chile and China; these countries account for most global production. Estimations of lithium distribution between different resources vary but roughly 65% of lithium is sources in brines, 25% in hard rock deposits and about 8% in sedimentary rocks (Meshram et al., 2014). While brines hold the largest lithium reserves, lithium production is dominated by hard rock mining, particularly in Australia, which has extensive spodumene deposits (Swain, 2016). China follows as the second-largest producer due to its combination of hard rock and brine-based lithium extraction. Current production is driven by hard rock mining due to economic and technological factors (Swain, 2016). Figure 2.2b and 2.2c summarizes the unequal geological distribution of lithium resources as well as the distribution of the lithium production worldwide.

The demand for lithium has seen large spikes in recent years. This is reflected in the fact that the global Li_2CO_3 price, which is often referred to in the lithium market, has increased 5.4 times, from $12 600 per tonne in 2021 to $68 100 per ton in 2022 as shown in Figure 2.3. However, this highest peak has passed due to concern of a short-term lithium oversupply, expiration of the Chinese Government's decade-long program of subsidies for electric vehicle (EV) purchases, and weaker than expected EV sales worldwide caused a clear decrease of the Li_2CO_3 price in 2023, when it settled around $46 000 per ton. (Jaskula, 2024). The consumption of lithium has also increased as well due to rising demand, where a 27% rise has been reported in lithium consumption from 142 000 tonnes to 180 000 tonnes between 2022 and 2023 (Jaskula, 2024). It has been estimated that handheld electronics, such as smartphones, laptops and tablets, contain approximately 2 to 20 g of lithium each, whereas in larger electric equipment, like electrical vehicles (EV) and energy storage systems (ESS), the amount of lithium is thousandfold higher or even more, ranging between 20 kg and 700 kg of lithium (Bae & Kim, 2021).

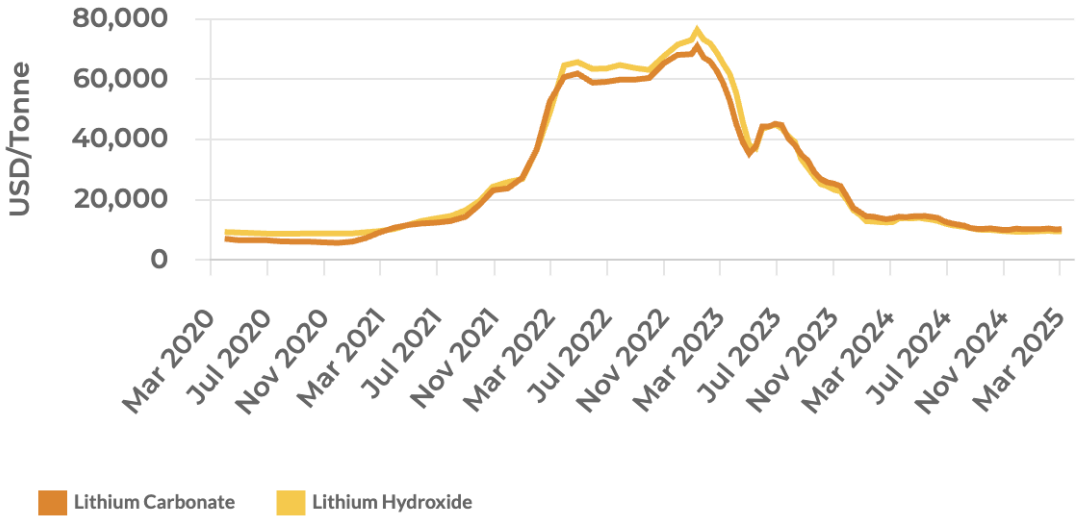

Figure 2.3 Lithium price from 2020 to 2025. Data is taken from (Benchmark Mineral Intelligence, 2025).

Interestingly enough, lithium is the 25th most common element in earth's crust (at 20 mg/kg) and thus it is not a rare element (Meshram et al., 2014). However, not all lithium is easily, and most importantly, economically extractible. The lithium grade, location, resource type (hard rock, brine or sedimentary rock), and lithium market price will have a great impact on the economic viability of a lithium mine.

2.1 MINERALOGY AND GEOLOGY

The Earth's crust contains a wide spectrum of different elements and minerals. However, the crust is not homogeneous and different elements and minerals are more abundant than others depending on the region or geological location on the earth. The goal of geology has been defined by one person as "to explore that part of the earth that is accessible to direct observation and to establish its history" (Gohau et al., 1990). As well, minerology has been defined as "The science that treats of those inorganic species called minerals, which together in rock masses or in isolated form make up the material of the crust of the earth, and of other bodies in the universe so far as it is possible to study them in the form of meteorites" (Dana, 1922). As emphasized, geology and mineralogy are closely related and can be considered more supportive fields of study rather than completely separate scientific disciplines. This section will discuss mineralogy and geology in the context of lithium ore.

2.1.1 Lithium-bearing minerals and typically associated gangue minerals

As reported by Grew (2020), lithium-bearing minerals are found in four different types of geological environments: (1) lithium–cesium–tantalum (LCT) granitic pegmatites and associated metasomatic rocks; (2) highly peraluminous pegmatites; (3) metasomatic rocks not directly associated with pegmatites; and (4) manganese deposits. Although several classification schemes exist, this study focuses on the LCT pegmatite type, which hosts spodumene at (Patriot Battery Metals) PBM's CV5 deposit and is the most relevant for lithium processing in this context.

Ore and gangue minerals of LCT pegmatites a can be affected by alteration which can change colors of the minerals. Alteration is a process in which rocks undergo chemical and mineralogical changes in an open system (Chischi, 2023). While this is similar to metamorphism (usually closed system), the chemical changes caused by alteration are typically more intense. The difference between the two processes can be subtle, especially when deposits form from metamorphic fluids, such as in the case of orogenic gold deposits (Phillips & Powell, 2010). Weathering also causes significant chemical and mineralogical changes, but unlike hydrothermal alteration, it is confined to surface rocks and occurs at lower temperatures (Mathieu, 2018).

There are more than a 100 known lithium bearing minerals in the world (Talens Peiró et al., 2013; Ralph et al., 2025). Despite the high abundance of Li in the Earth's crust (Meshram et al., 2014), the diversity of Li-bearing minerals is relatively low if compared to other common elements. For instance, iron and copper are reported to form 953 and 643 different mineral species, respectively (Krivovichev et al., 2018) which is significantly more than lithium. However, this is partly explained by their much higher natural concentrations in the Earth's crust.

Not all Li-bearing minerals are well known or of interest in terms of economic Li extraction. The most well-known and most widely used Li-bearing mineral is spodumene ($LiAlSi_2O_6$). Other important minerals include petalite, lepidolite, amblygonite, and eucryptite, which are the main sources of Li (Bulatovic, 2015; Tadesse et al., 2019; Talens Peiró et al., 2013). Zinnwaldite and triphylite are also mentioned in the literature (Colton, 1957; Grosjean et al., 2012).

The name spodumene originates from the ancient Greek word *spodumeneos* meaning "burnt to ashes" (Dessemond et al., 2019). This figure of speech is quite an accurate illustration of the

appearance of spodumene's greyish, ash-like form after grinding. However, in nature it is possible for this lithium aluminosilicate to produce two different kinds of gems of different colors. Hiddenite is known as the green spodumene gem, whereas kunzite gems have color of pink and purple (Stuhlman, 1929). In terms of Li_2O grade, spodumene has a theoretical grade of 8.03% Li_2O (Gao et al., 2023). Nowadays, the quantification of spodumene grade (as opposed to chemical Li or Li_2O grade), especially through online analysis, is also of interest and can be accomplished using different analytical methods, such as Infrared spectroscopy (IR), Hyperspectral imaging (HSI) and Timegated Raman spectroscopy (TRS). Out of these, TRS indicates a high potential for online spodumene content quantification from both solid and slurry samples (Laitinen et al., 2024).

Spodumene can exist in three different crystalline structures (Abdullah et al., 2019), of which α-spodumene is the naturally occurring monoclinic structure (C2/c) found in nature. This monoclinic structure can be modified to a tetragonal one (β-spodumene) by heating α-spodumene at 800 – 1100°C for 30 - 60 minutes (Salakjani et al., 2016). The third phase of spodumene (ɣ-spodumene) is metastable (hexagonal) and is formed when α-spodumene is heated at lower temperatures (700 – 900°C). However, it can be converted to β-spodumene if the temperature is raised further (Aylmore et al., 2018; Salakjani et al., 2016). Figure 2.4 illustrates the transformation temperature between different spodumene phases.

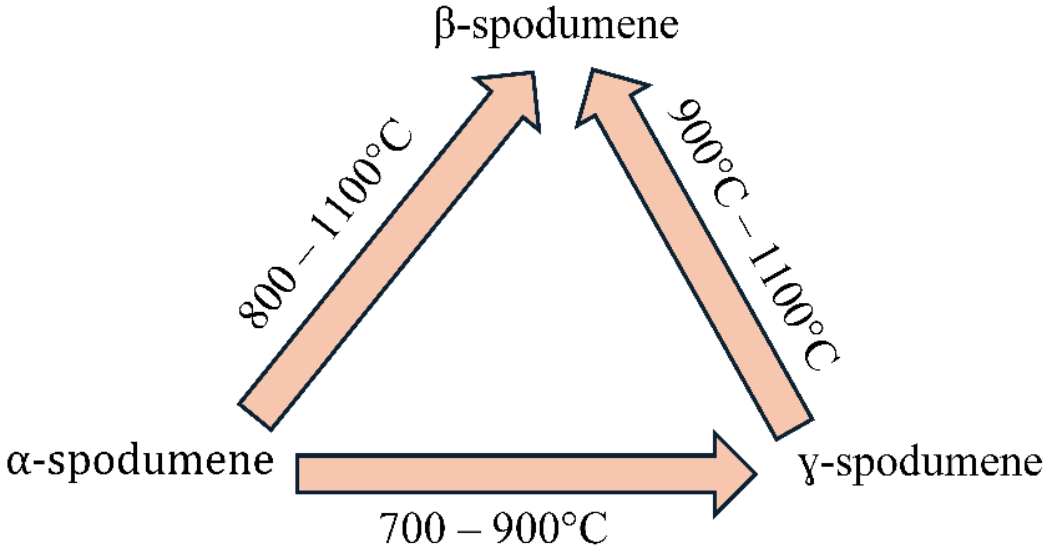

Figure 2.4 Spodumene crystalline modifications transits at different temperature. (Modified from Dessemond et al., 2019).

Petalite ($LiAlSi_4O_{10}$) is a lithium aluminosilicate whose chemical composition consists of Li_2O 4.86%, Al_2O_3 16.65% and SiO_2 78.48% when expressed as individual oxides. Petalite is the high temperature-low pressure phase of spodumene (London, 1984). After spodumene, petalite is the most abundant Li mineral in LCT pegmatite (Grew, 2020). The name petalite is from the ancient Greek word *petalion*, meaning leaf or blade (Stempkowska, 2021). Petalite presents a monoclinic crystallographic system and has a space group P2/a (Stempkowska, 2021) and it tends to form big crystals (London, 2017). In terms of color, petalite can be colorless or yellow, grey or white, depending on surrounding conditions such as elemental substitutions within the crystal structure. Petalite is also known to have highest Li_2O/Al_2O_3 ratio among natural minerals (Stempkowska, 2021).

Lepidolite ($K(Li,Al)_3(Si,Al)_4O_{10}(F,OH)_3$) belongs to the mica group (Ogorodova et al., 2005). As seen from the chemical formula, lepidolite is known to have high variability in its chemical composition due to its tendency for forming solid solutions with muscovite, phlogopite and other lithium micas (Ogorodova et al., 2005). As other types of mica are characterized by their glossy and layered texture, lepidolite also possesses these features and it exists typically in rare-metal granites and pegmatites (Ogorodova et al., 2005). Lepidolite crystals have a unique color varying from pink to purple (Meshram et al., 2021) which is due to traces of Mn^{3+} and it is often observed as an alteration mineral of spodumene. However, the color can also have light hues of yellow, green, or gray based on traces of iron (Fe) or other chromophores (London, 2017). Notably, the color of the mineral is not an indication of the lithium content. Lepidolite deposits often contain other valuable elements such as rubidium (Rb) and cesium (Cs) which usually are separated during lepidolite hydrometallurgical processing (Luong et al., 2013; Ogorodova et al., 2005; Yan et al., 2012). Theoretical Li_2O grade for lepidolite is reported to be 7.7% which is less than spodumene but clearly higher than petalite (Gao et al., 2023).

Amblygonite ((Li,Na)AlPO4(F,OH)) is a fluorine-rich aluminophosphate and is geologically found in pegmatite and fluorine-rich topaz-bearing granite (Choubey et al., 2016). It has a triclinic crystal structure and naturally high Li content, up to ~10% of Li_2O, which is even higher than that of spodumene (Xie et al., 2023; Zhou et al., 2024). Despite the fact that amblygonite has the highest lithium oxide content out of the Li-bearing minerals, the extraction of amblygonite has received

little attention in the literature (Choubey et al., 2016; Zhou et al., 2024), possibly because no economically viable deposits of amblygonite exist.

Eucryptite ($LiAlSiO_4$), rarely occurs alone and is often associated with spodumene and petalite pegmatites. Eucryptite is the low temperature, low pressure phase of spodumene, to which spodumene is usually transformed during alteration. Based on its physical and optical properties, eucryptite closely resembles quartz, making it difficult to distinguish without ultraviolet light, under which it emits a bright red fluorescence (London, 2017).

Gangue minerals often associated with spodumene, and pegmatite ores include quartz, feldspars and micas along with tourmaline, garnet and beryl (Anthony et al., 2003; Aylmore et al., 2018). In addition, economically valuable accessory minerals such as columbite and pollucite may also be present. However, these silicate minerals can be abundant in spodumene deposits with 30-45% each of quartz and feldspar being common (Xie et al., 2021). The abundance of these minerals can cause issues in the pretreatment of spodumene ore, for example, in gravity or magnetic separation (Xie et al., 2021). Micas are common and may be abundant gangue minerals associated with pegmatite deposits (London, 2017). In most cases, micas are volumetrically minor, but some deposits can be very rich in coarse muscovite for example. Abundant mica concentration may cause issues in the flotation of Li-rich minerals but also in the DMS due to particle shape and near density to spodumene (Gibson et al., 2017).

2.1.2 Drill core observations

One of the main ways to obtain critical information from the Earth's crust for the mining or exploration operation is core drilling. Drill cores are important as for the knowledge that they provide of the rock masses under the soil. Based on core data, companies get a comprehensive picture of the geological environment. There are many methods to produce data from drill cores. For example, core data can be merged to create a geological map of a deposit which can be used to calculate ore grades and delineate between economic and non-economic zones. This chapter provides an overview of the analysis of drill cores and what properties geologists typically evaluate.

Geological data is first obtained from what is typically termed as "drill core logging" where collected drill cores are used such as seen in Figure 2.5. The logging data consists of different types

of information, such as alteration, lithology, as well as structural, mineralization, and geotechnical data (Glacialle, 2017). From the literature, the most common information recorded in drill core logging are the length of drill cores, core recovery, identification of rock and mineral types, visual estimation of mineral content, texture, structure, mineralization, alteration, vein and fracture frequency, and rock quality designation (RQD) (Glacialle, 2017). Owing to the fact that they are obtained via visual inspection, most of these measurements present some subjectivity and are therefore highly dependent on the logger's experience and perception. The accuracy of the data is thus usually highly variable and unmeasured, although some systematic logging methods can be found in the literature aiming to mitigate this subjectivity (Bright et al., 2014). However, relying only on visual data, especially in terms of rock and mineral identification, these logging methods have shortcomings and would benefit from the use of supplementary methods, such as portable X-ray fluorescence (XRF) or laser induced breakdown spectroscopy (LIBS), core scanning, and laboratory/chemical analysis (Glacialle, 2017).

Figure 2.5 Drill cores stored in wooden boxes after collection from the site. The core box length is approximately 1,2 meters. Geologists have analyzed these cores visually and marked the location info on the cores. Example from a spodumene-bearing pegmatite of Patriot Battery Metals's Shaakichiuwaanaan project.

The length of the core and location of geological parameters (contact, mineralization, fault, …) are measured using a tape measure. Core recovery refers to the fact that not all cores are recovered due to fractures and breakage. Hence, the total recovered core is calculated by dividing the length of the core by the length of drilled interval. This factor indicates how well the recovery of the core was (Lemy et al., 2013).

Textures are commonly described using various qualifiers, including grain size and internal structures such as mineral alignment, bedding, and deformation degree (Bons et al., 2012; Cacciari & Futai, 2019; Okubo, 2010). These descriptors are used qualitatively to differentiate between lithologies, making the method somewhat subjective. Typically, companies report only the average grain size and sometimes a general range (e.g., Pyrite 10%; 1–2 mm, up to 5 mm). However, in the case of PBM, grain size classification at the CV5 deposit is more detailed and includes estimations of the proportion of grains above or below certain size thresholds. Although this approach is not common industry practice, it provides valuable information. As shown in this study, such classification helps highlight the limitations of standard logging practices, especially in terms of representing full grain size distributions.

Geotechnical measurements such as core recovery, vein and fracture frequency, and RQD are typically assessed first by a technician upon receiving the core. For example, vein and fracture frequency is measured by dividing the number of fractures, counted by technician, by the length of the sample. This method is not reliable because some core are broken during the drilling process or are fractured by the driller while recovering the core from the core barrel, making it impossible to count the exact number of real fractures. Therefore, these factor is calculated based on the fact that non-natural fractures are a low percentage of observed fractures (Séguret et al., 2015). However, a more common factor is usually calculated, the RQD, which gives a better evaluation of rock integrity (Séguret et al., 2015).

Rock quality designation (RQD) is a calculated recovery index which is widely used to illustrate the quality of the rock and to indicate its structural integrity. RQD provides an estimation of the “rock quality” (or competence) and is used as a first indicator of areas of poor-quality ground (Lemy et al., 2013). This method was first presented by Deere (1963). The protocol for calculating the value is to sum the length of all the pieces of core that are over 100 mm long and then divide the sum by the total length of the core (Lemy et al., 2013; Milne et al., 1998). RQD has some

limitations as it is sensitive to orientation and insensitive to widely spaced joints. Another problem arises with the diameter of the core because a smaller core tends to break more easily (Milne et al., 1998). Some other methods for RQD have been presented in the literature, including "Handled Rock quality designation" (HRQD), which is measured the same way as original RQD, first handling the core by twisting and bending, but without using a significant force (Milne et al., 1998).

In addition to RQD, various other empirical correlations have also been suggested to estimate the engineering properties of jointed rock masses using classification indices (L. Zhang, 2016). Rock Mass Rating (RMR) was first introduced by Bieniawski (1973). It is a well-known and widely used index to validate rock mass quality. The use of this index has had a great impact on civil engineering and mining activities (Ferrari et al., 2014). The main applications are to evaluate the geomechanical features and stability conditions in areas of interest. Moreover, in terms of mining, RMR is critical especially in tunnelling and foundations as well as geological risk management. The RMR system can also be used to verify how likely rock slopes are to slide and to find the weaker areas of rock where it might break or collapse (Ferrari et al., 2014). RMR is typically presented as a sum of different factors as shown in equation 2.1 (Bieniawski, 1973). RMR value can be used to describe the rock quality and fracture abundance based on criteria presented in Figure 2.6.

$$RMR = UCS + RQD + SD + CD + GC + OD \tag{2.1}$$

Where UCS = Uniaxial Compressive Strength of rock mineral

RQD = Rock Quality Designation

SD = Spacing of Discontinuities

CD = Condition of Discontinuities

GC = Groundwater Conditions

OD = Orientation of Discontinuities

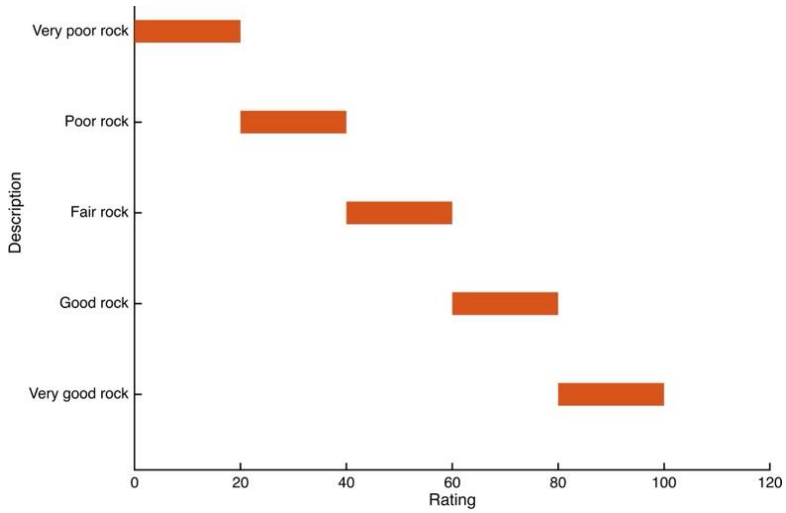

Figure 2.6 Criteria for classification of fracture condition in RMR (Qazi & Singh, 2023).

Another important index for mining and more specifically tunnelling is called “Rock mass quality” also known as Q-system. This method was first introduced by Barton et al. (1974). The Q-system considers six different features to evaluate the quality of rock. These dependencies are presented as follows (Barton et al., 1974):

$$Q = \left(\frac{RQD}{J_n}\right) \cdot \left(\frac{J_r}{J_a}\right) \cdot \left(\frac{J_w}{SRF}\right) \tag{2.2}$$

Where

RQD = rock quality designation

J_n = joint set number

J_r = joint roughness number

J_a = joint alteration number

J_w = joint water reduction factor

SRF = stress reduction factor

A third widely used approach for determining rock quality and characteristics (and used by Patriot Battery Metals on the Shaakichiuwaanaan project) is the globally recognized and standardized ISRM methods, which include 62 suggested procedures for assessing rock quality. These methods, designed for both laboratory and in situ testing, provide definitive guidelines for rock characterization, testing, and monitoring in rock engineering. They enable the identification, measurement, and evaluation of various rock properties, ensuring reliable test results (Ulusay, 2015).

The Schmidt Hammer Rebound Hardness (SHRH) test is a widely used method for estimating the uniaxial compressive strength (UCS) of rock. Its simplicity and broad applicability make it a popular index tool. The revised method emphasizes using the SHRH to measure rebound hardness in both laboratory and in situ conditions, serving as an indicator for UCS and the modulus of elasticity (E). The SHRH operates with a spring-loaded piston that impacts a surface when the plunger is pressed. The rebound height, which depends on the material's hardness and resistance to impact, is measured as a percentage of the spring's maximum stretch before release (Ulusay, 2015).

In addition to the traditional Schmidt Hammer, a similar rebound-based hardness testing method, Equotip, is now widely used for rock hardness assessment. Originally designed for metals, Equotip measures rebound velocity using an induction coil, with results expressed as Leeb Hardness. It is particularly useful for small rock, such as drill core samples and provides digital readouts with automatic impact direction compensation (Viles et al., 2011).

Another example of an ISRM method is the Dynamic Strength (DS) test, which measures the dynamic uniaxial compressive strength of cylindrical rock specimens. This method is primarily used for classifying and characterizing intact rocks. The apparatus, known as the Split Hopkinson Pressure Bar, generates and records stress waves interacting with the rock specimen. In addition to DS, other less common methods for estimating uniaxial compressive strength include the point load test and seismic velocity measurements, which provide indirect assessments of rock strength (Ulusay, 2015).

2.2 MINERALOGICAL PROCESSES FOR CONCENTRATING LITHIUM MINERALS

Before lithium finds its way into the batteries of electrical vehicles, lithium itself needs to be separated from the ore. There are multiple ways to process lithium ores to an end product. The selection of the beneficiation methods is highly dependent on the surrounding factors, such as the type of deposit, its location and the geological parameters (ore and gangue minerals present, grain size, alteration, etc). For example, PBM is proposing a DMS only flowsheet for spodumene recovery due to the CV5's large spodumene grain size. In addition, the market price of lithium will affect the selection of the process equipment and the whole life cycle of the mine site.

2.2.1 Main processes with examples of DMS and crushing

Generally speaking, the beneficiation of a lithium ore starts when the mined ore reaches the mill (concentrator). In some flowsheets the first operation is ore sorting to reject waste or upgrade the feed, but this is not universal and many plants begin directly with crushing. Primary and, if needed, secondary crushing are then used to obtain adequate particle size for further processing. Crushing is typically carried out using open-circuit primary crushing (usually a jaw crusher) followed by closed-circuit secondary cone crushing. In some cases, however, separation techniques may already be applied to the run-of-mine ore prior to crushing, or immediately after primary crushing, such as screening or density-based pre-concentration (Welham, 2019a). Often, the run-of-mine spodumene ore is crushed to 100% passing -16 mm if the flowsheet does not include DMS, and to -12 mm if DMS is included (Tadesse et al., 2019). In practice, however, achieving these particle sizes typically requires tertiary and sometimes even quaternary crushing stages, depending on the ore and circuit design. The optimum particle size is dependent on mineral liberation properties (grain size and how it liberates as it breaks), the grade of the ore and the downstream beneficiation steps. Figure 2.7 presents a typical comminution circuit used in spodumene processing. This sub-section discusses other processes, leaving gravity-based separation processes to be discussed in more details in section 2.3.

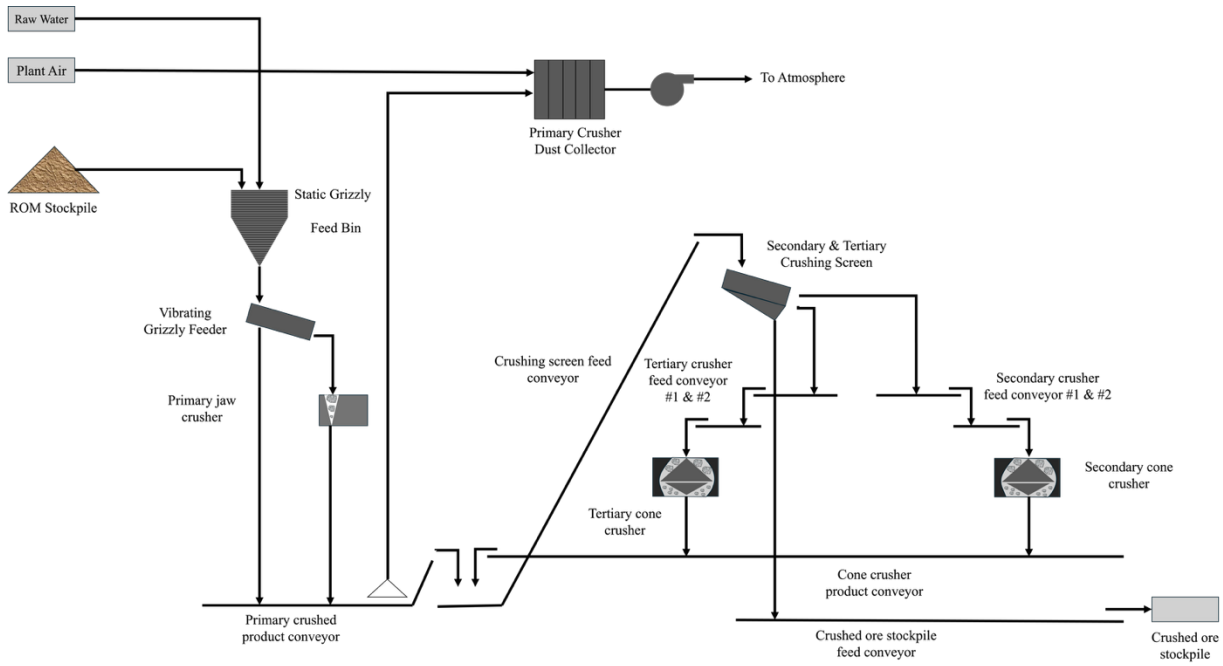

Figure 2.7 Spodumene concentration crushing circuit flowsheet, inspirated by (Oliazadeh et al., 2018).

The crushing stages are usually followed by the dense media separation (DMS) circuit or the grinding circuit (prior to flotation), depending on the layout. The DMS process is highly dependent on particle size and is only applicable to certain size fractions, with circuits often consisting of one or more cyclones with different cut sizes (Tadesse et al., 2019). The flowsheet shown in Figure 2.8. also includes a scrubber, whose role is to wash the crushed ore, remove clay and fines, and condition the material before it enters the DMS circuit, thereby improving separation efficiency through cleaner particle surfaces and more stable media performance.

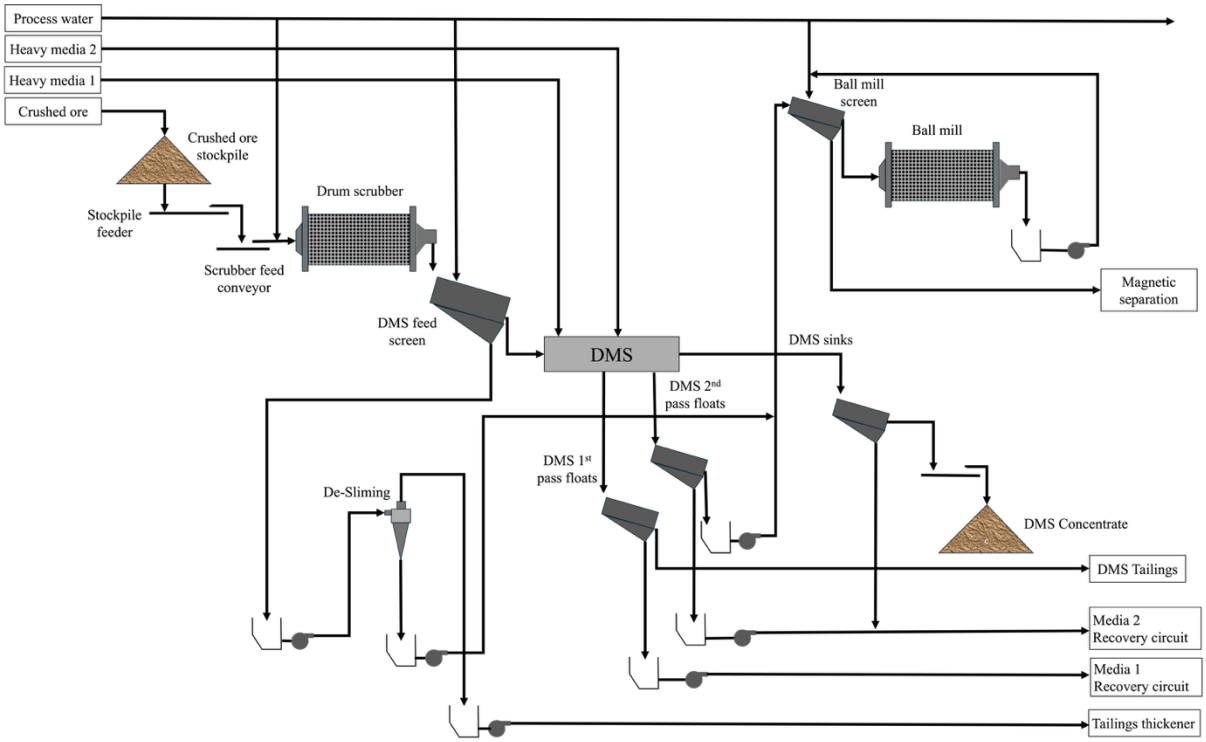

Figure 2.8 An example of preliminary scrubbing and DMS circuit. Inspired by (Oliazadeh et al., 2018).

Regardless of whether DMS is included in the flowsheet, flotation is then typically applied to finer fractions as part of the process flowsheet (Xie et al., 2021). Exceptions include the Bald Hill lithium and tantalum operations in Australia (Tadesse et al., 2019). In these flowsheets, the flotation of spodumene is not included with various gravity-based separation steps being used instead and the fine fractions (< 0.85 mm) being rejected to tails. Another example of a flotation-free layout has been presented for the Shaakichiuwaanaan Project by Patriot Battery Metals (PBM) in Quebec, Canada, who plan to build a mill where the main separation method is DMS. Flotation is, however, a consideration for future use in processing fine particles to be collected at the beginning of the mine's life (Patriot Battery Metals, 2024).

It is also becoming more common to apply classical ore sorting based on color and density differences before the ore processing, as sensor-based sorting has become a more important separation method. Optical sorting can detect differences in color and morphology of the minerals. While grain size variations may influence sorting efficiency, the sensors primarily rely on optical properties rather than direct size measurements (Brandt & Haus, 2010; Tadesse et al., 2019). In addition, the rise of artificial intelligence (AI) has enabled even more accurate sorting applications

which are based on either machine learning (Maitre et al., 2019) or deep learning (Latif et al., 2022).

The DMS circuit, when complemented by other means, is usually followed by a grinding circuit where the material is ground to reach a higher degree of liberation and thereby enable higher recovery rates and upgrading in subsequent flotation. Typically, grinding is conducted in a ball mill (down to 500 µm), since the feed material is already crushed to a sufficiently small size, and the particle size is not enough to justify SAG or AG milling. Notably, 500 µm also marks the lower practical limit for conventional gravity-based separation methods such as DMS, as efficiency tends to decline below this threshold (Ait-Khouia et al., 2021). As in most hard-rock grinding circuits, hydrocyclones are used to recirculate the coarser material and achieve a consistent product particle size. The basic principle of separation in hydrocyclones uses centrifugal sedimentation, meaning the suspended particles are subjected to centrifugal acceleration, which causes heavier or coarser particles to move outward toward the cyclone wall while lighter or finer particles stay near the center of the flow.

Unlike centrifuges or screens, hydrocyclones have no moving parts, and the necessary vortex motion is performed by the fluid itself. The separation occurs due to differences in both particle size and density. Larger and denser particles experience greater centrifugal force and migrate to the outer wall, exiting through the underflow, while finer or less dense particles remain in the central vortex and are carried to the overflow (Svarovsky, 2001). The obtained concentrate (sink fraction) is often subjected to magnetic separation, primarily to remove Fe-bearing minerals that may report to the sinks. In contrast, the dense media (such as ferrosilicon) is usually recovered separately by screening and rinsing the cyclone products and then thickened or dewatered before being recirculated back to the DMS circuit. This distinction is important to ensure efficient media recovery and to maintain concentrate quality before flotation.

DMS is based on density differences of the minerals in the ore and are an example of mechanical separation. Unlike DMS, flotation is considered a physico-chemical separation method, as it relies on the use of chemical reagents to modify the surface properties of particles. As stated before, flotation has been the most commonly reported separation method for spodumene ore. Generally, the surface of spodumene tends to have a negative zeta potential in solution when pH > 3 (Wills & Finch, 2016d). Cationic collectors used in direct spodumene flotation require pH values above 3

for physical adsorption to occur. However, in most cases they are applied in reverse flotation at pH values below 3, where amines are used to float gangue minerals such as quartz, mica, and feldspar, while spodumene remains in the sink product. More commonly, direct spodumene flotation is achieved using anionic collectors, such as sodium oleate, due to the presence of positively charged sites on the spodumene surface. These sites, primarily exposed Al^{3+} ions, can facilitate the chemical adsorption of anionic collectors. Furthermore, the addition of Ca^{2+} ions have been shown to enhance spodumene recovery by reducing its surface charge, thereby promoting the interaction with anionic collectors (Cook et al., 2023; Filippov et al., 2019).

As noted, other reagents, in addition to the collector, can be used depending on the chemical characteristics of the ore and the flotation conditions. Commonly used activators in spodumene flotation are metal ions, such as Mg^{2+} and Ca^{2+} which are used to modify the surface properties to be more favorable for the collector to adsorb onto the surface. Additionally, some reagents, such as NaOH or HCl, are used as pH regulators to affect the pH and thus the zeta potential of the spodumene's surface (Filippov et al., 2019; Wang & Fu-Shun, 2007). In general, a typical spodumene froth flotation circuit can be consist of roughers, cleaners and recleaners: rougher concentrate advances to cleaning, intermediate tails are discarded, and the recleaner concentrate is thickened and filtered as the final product. An example of such a layout is described by (Welham, 2019b).

In industrial processes which uses DMS as a pre-separation step, a magnetic separation process step is usually present after the flotation. The flotation reject is discharged into a tailings management facility while the spodumene concentrate is filtered and sent to a refinery for a second transformation. A general and simplified flowsheet for Li beneficiation, showing all the unit processes described earlier is presented in Figure 2.9.

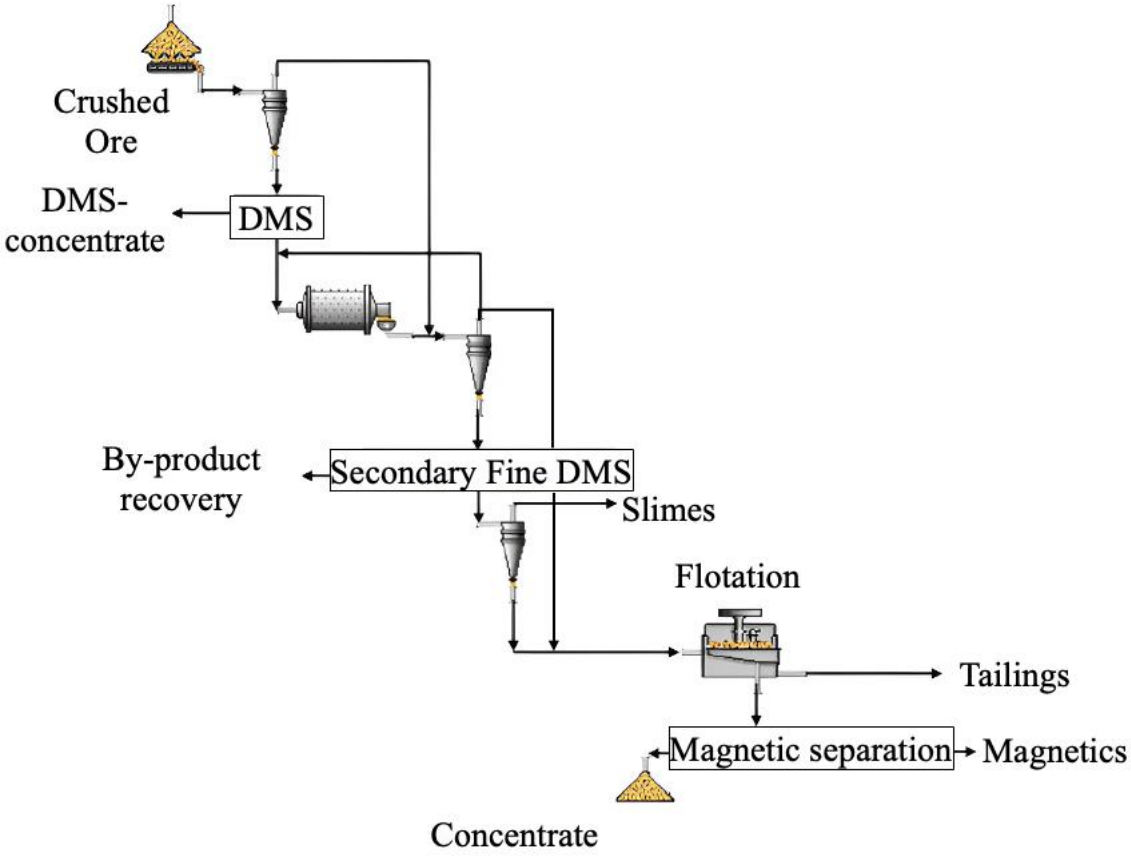

Figure 2.9 General flowsheet of lithium beneficiation circuit (Modified from Tadesse et al., 2019).

The extraction process of spodumene is based on several unit processes and related equipment. Nowadays, the increase in digitalization makes it easier and to achieve more precise to control and monitor the behavior of the process. A wide range of processing instruments, such as sensors (pressure, temperature, flow rate, density and viscosity), control devices (control valves, frequency converters), analyzing devices (pH, gas, moisture), safety alarms (pressure, gas detectors), and control systems (programmable logic controller (PLC), distributed control system (DCS)) play a vital role on the quality of the concentrate (McMillan, 1999). In spodumene extraction, many of these items are used. Atmospheric pressure and temperature do not have a major effect on DMS. In this regard, DMS circuit process control can be said to be fairly simple, although several variables still have to be controlled (Kawatra, 2019).

2.2.2 Characteristics sought in concentrates

Theoretically, the maximum Li_2O content of spodumene is 8.03%, calculated from its molar mass as follows:

$$\mathrm{M(spodumene)} = \mathrm{M(Li)} + \mathrm{M(Al)} + 2\mathrm{M(Si)} + 6\mathrm{M(O)}$$

$$= 6.941\frac{\mathrm{g}}{\mathrm{mol}} + 26.982\frac{\mathrm{g}}{\mathrm{mol}} + 2 \cdot 28.086\frac{\mathrm{g}}{\mathrm{mol}} + 6 \cdot 16.00\frac{\mathrm{g}}{\mathrm{mol}} = 186.09\frac{\mathrm{g}}{\mathrm{mol}}$$

And thus, spodumene has a % of Li_2O as follows:

$$Li_2O\ (\%) = \frac{M(Li) + \frac{1}{2}M(O)}{M(spodumene)} = \frac{6.941\frac{\mathrm{g}}{\mathrm{mol}} \cdot \frac{1}{2} \cdot 16.00\frac{\mathrm{g}}{\mathrm{mol}}}{186.09\frac{\mathrm{g}}{\mathrm{mol}}} \cdot 100 = 8.0289$$

As noted above, the theoretical grade represents the maximum achievable value. In practice, the Li_2O grade achieved is always lower. According to the literature, spodumene concentrates meant for battery use generally aim for Li_2O values above 6.0 % and Fe_2O_3 below 1.0 % (Opoku et al., 2025). In contrast, technical-grade concentrates, used in ceramics, glass, and other industrial applications, typically require even higher Li_2O (e.g., > 7 %) and significantly lower Fe_2O_3 (e.g., < 0.25 %) to meet purity specifications. Higher Li_2O % in the concentrate are more desirable, as the number of impurities and gangue minerals is targeted to be as low as possible. Potential reasons why this theoretical 8.03% Li_2O is impossible to reach are for example the inclusion of quartz and other minerals as studied by Sousa et al., (2019). Meanwhile, (Ralph et al., 2025) demonstrated that post-ore alteration of spodumene produces muscovite, cookeite and quartz as secondary phases, which degrade spodumene grade and impair lithium recovery. Both of these phenomena are relevant in the context of characterizing the PBM's CV5 deposit. There are also always deleterious elements within the spodumene lattice such as Fe^{3+} replacing Al^{3+}, Na^{+} replacing Li^{+}, so that the 8.03% Li_2O can never be reached, even for pure spodumene (Charoy et al., 2001). Moreover, higher concentrations typically come at the expense of recovery, since achieving these high grades usually means rejecting significant quantities of mixed or even pure spodumene particles. Therefore an economic tradeoff between recovery and grade is typical, like in most other mineral separation processes. Some of the minerals commonly found with spodumene are

presented in Table 2.1, showing how most of them have a lower density, compared to spodumene's (3.2 g/cm^3).

Table 2.1: Minerals in spodumene ores and their properties (Wells et al., 2022).

Mineral name	Chemical formula	Density (g/cm^3)	Color	Melting point (°C)	Issues
Quartz	SiO_2	2.65	White/ grey	1610	Fractures during rapid heating tests but no real interaction between quartz and spodumene transformation.
Micas (Muscovite)	$KAl_2(Si_3Al)O_{10}(OH)_2$	2.825	Gray, Silver, white	1100-1200	Melting leads to the formation of clinker, an undesirable material that tends to coat the interior surfaces of the calcine roaster.
Feldspar (albite)	$NaAlSi_3O_8$,	2.62	White, Gray	1060-1200	Melting leads to the formation of clinker, an undesirable material that tends to coat the interior surfaces of the calcine roaster.
Feldspar (microcline)	$KAlSi_3O_8$	2.56	Green, Gray	1060-1200	Melting leads to the formation of clinker, an undesirable material that tends to coat the interior surfaces of the calcine roaster.
Hematite	Fe_2O_3	5.3	Reddish, gray, Black	1565	Hematite forms "vein-like" structures and consolidates into grains within the spodumene.

As can also be seen in Table 2.1, some minerals present alongside spodumene can affect the high-temperature calcination process in various ways. Feldspars (albite and microcline) and muscovite melt at relatively low temperatures (1000–1200°C), leading to clinker formation, which coats

furnace surfaces and disrupts processing efficiency. Quartz, despite its high melting point (1610°C), fractures due to thermal stress but does not chemically interact with spodumene. Hematite, with a melting point of 1565°C, tends to consolidate and form vein-like structures in spodumene grains, which can affect downstream processing (Wells et al., 2022).

2.3 GRAVIMETRIC SEPARATION AND SPODUMENE

Gravimetric separation is a method that utilizes density contrasts of the different particles to separate materials from each other. Gravimetric separation can be applied if the difference in density between ore and gangue minerals is big enough. Spodumene beneficiation is one of these processes where gravimetric separation can be applied. This chapter takes a closer look at different gravimetric separation methods and discusses their main characteristics.

The most significant factor in gravimetric separation, as indicated by the name, is the specific gravity of the particle. Earth's gravitational field pulls the particle downward according to Newton's second law: $G = mg$, where G is the gravitational force, m is the mass of the particle, and g is the gravitational acceleration constant. The density of a particle is defined as $\rho = \frac{m}{V}$, where ρ is density, m is the mass of a particle and V is the volume of a particle. Combining these equations shows that gravitational force G depends on the density (ρ) and volume (V) of the particle, since $G = \rho V g$. The greater the force influencing a particle due to its higher density, the easier it becomes to separate it from other particles that are submitted to a lower gravitational force.

As explained above, the density of a particle as well as its volume influence its path in a gravitational separation process. The greater a volume the particle has, the stronger the force generated. However, in terms of gravimetric separation, another significant factor is the shape. For example, in shaking table separation, flat-shaped particles (like micas) won't be able to roll easily across the table surface in the water film, with such particles sticking to the deck and travelling down to the concentrate discharge (Wills et al., 2016).

2.3.1 Separation by heavy liquids

Heavy liquid separation (HLS), sometimes referred to as dense fluids or solutions, is a well-known method for separating or concentrating particles based on their density differences. In essence, a

particle's density is the ratio of a particle's mass to its volume and if that ratio is lower than the density of the (heavy) liquid, the particle will float and remain at the surface of the liquid. Despite the simple and convenient nature of this method, the toxicity and price of heavy liquids does not allow them to be used for industrial scale separation. Rather, dense-media separation (DMS), in which a water-fine particle mixture is used as heavy media is the common method used effect separation based on a media's density. However, since HLS is still often used at laboratory scale to predict the outcome of DMS (which will be discussed in detail in section 2.3.2), this subsection will provide an overview of HLS testing.

Over time, several reagents have been used for HLS test work. Some of the heavy liquids (HL) possess a high toxicity and thus the usage of these products is limited or requires extreme care during handling. Typical HLs are bromoform, methylene iodide, clerici solution, and tetrabromoethane (Hauff & Airey, 1980).

However, the so-called "first generation" organic heavy liquids listed above have increasingly been replaced with other "second generation" substances which are less toxic, and more stable and thus the usage and handling of these chemicals are much easier. These include sodium polytungstate (SPT), lithium metatungstate (LMT) and lithium heteropolytungstate (LST) (LST Heavy Liquid for Float SinkSeparations, n.d.).

Sodium polytungstate (SPT) ($Na_6(H_2W_{12}O_{40})$) is a nontoxic solid that is water soluble and thus can be mixed with pure water to generate a heavy liquid. The density of this reagent can vary widely from 1 g/cm^3 to a saturated solution at 3.10 g/cm^3. Due to the large spectrum of densities and nontoxicity of the reagent, SPT can be used to separate effectively particles in regular laboratory conditions, even without the use of a fume hood, which is a great advantage compared to "first-generation" heavy liquids. Other advantages of SPT are its noncorrosive nature, stability over a large pH range (2-14), ease of dilution and easily adjustable density, and the possibility of recycling and reusing the reagent. Disadvantages, on the other hand, include its high viscosity leading to longer settling time (Skipp & Brownfield, 1993).

Two other popular heavy liquids that share similar features and are used in the density separation process are lithium metatungstate (LMT) $Li_6OH_2W_{12}O_{40}$ and lithium heteropolytungstate (LST). Both of these reagents are produced by establishing an aqueous solution of tungstate salt. Aqueous

LMT can reach a density of approximately 3.5 g/cm^3 (Duyvesteyn et al., 1994) whereas LST can achieve density of 3.3 g/cm^3 (Mounteney, 2011). Both LST and LMT are non-toxic clear liquids, and they can be used without a fume hood. However, the benefit of LST over inorganic heavy liquids, such as SPT, is its thermal stability which enables it to be heated and thus regain the original density. Hence, quick and easy recycling is possible. Other key benefits of LST compared to SPT include its considerably lower viscosity, better solubility in water, and significantly lower cost, making it a practical and widely used reagent for HLS testing (Mounteney, 2011).

The typical procedure for heavy liquid separation is illustrated in Figure 2.10. Firstly, a separatory funnel is partially filled with heavy liquid (HL), after which the sample is introduced and the remaining HL is added. This sequence minimizes the formation of air bubbles and ensures that all particles start settling from the same point (Chornkrathok et al., 2024). A typical ratio between the sample and HL is 1:5, meaning that 50 g of sample requires 250 g of HL. The settling time varies depending on particle size, mineral density, and the ratio of heavy to light minerals present (Mounteney, 2011).

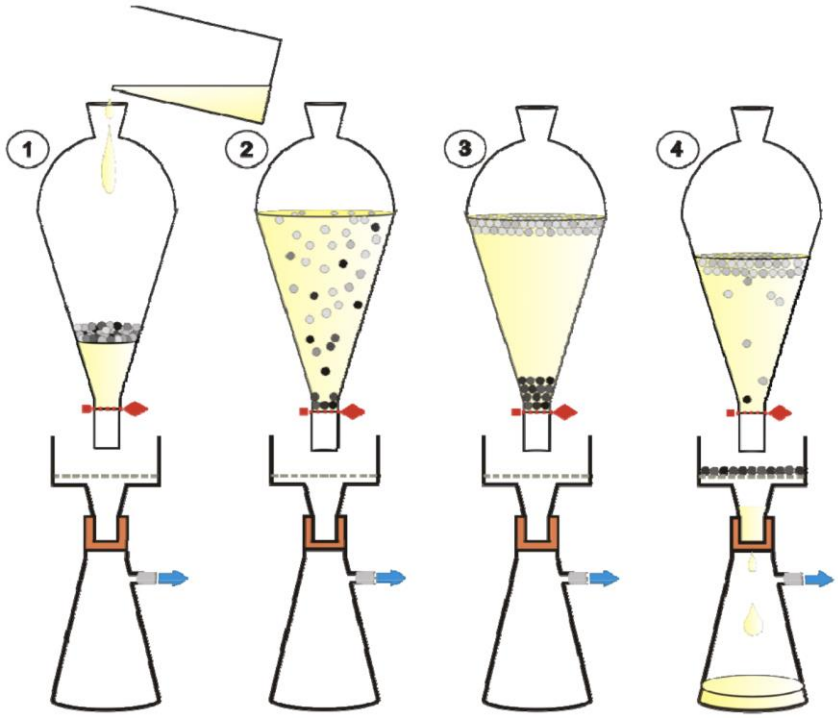

Figure 2.10 Simplified HLS test method. 1) HL is added into separating funnel followed by the sample and lastly the remaining HL. 2) Particle dispersion, 3) Separation of minerals. 4) Recovered mineral concentrate and filtration Courtesy of the British Geological Survey © UKRI [2011] (Mounteney, 2011).

Another important factor which affects the separation efficiency is the mineral liberation. Given a certain HL density between that of two minerals, well liberated minerals will separate more accurately and faster than particles at low liberation stage, owing to the elevated difference in density. Figure 2.11 depicts the impact of mineral liberation on HLS testing. It highlights how incomplete liberation will cause some of the dense minerals to report to the float, and some of the lighter minerals to sink.

There is no universal settling time applicable in all cases, but tests usually take less than 30 minutes (Mounteney, 2011). The separation can be considered complete once a clear division between the light and heavy fractions becomes apparent. After the separation is deemed complete, the sink and float fractions are recovered, using a slotted spoon or by sequentially emptying the container via the bottom, and the samples are rinsed and washed to remove excess HL. Prior to recycling the HL, it is usually pumped through a filter paper to remove all contaminants (Mounteney, 2011).

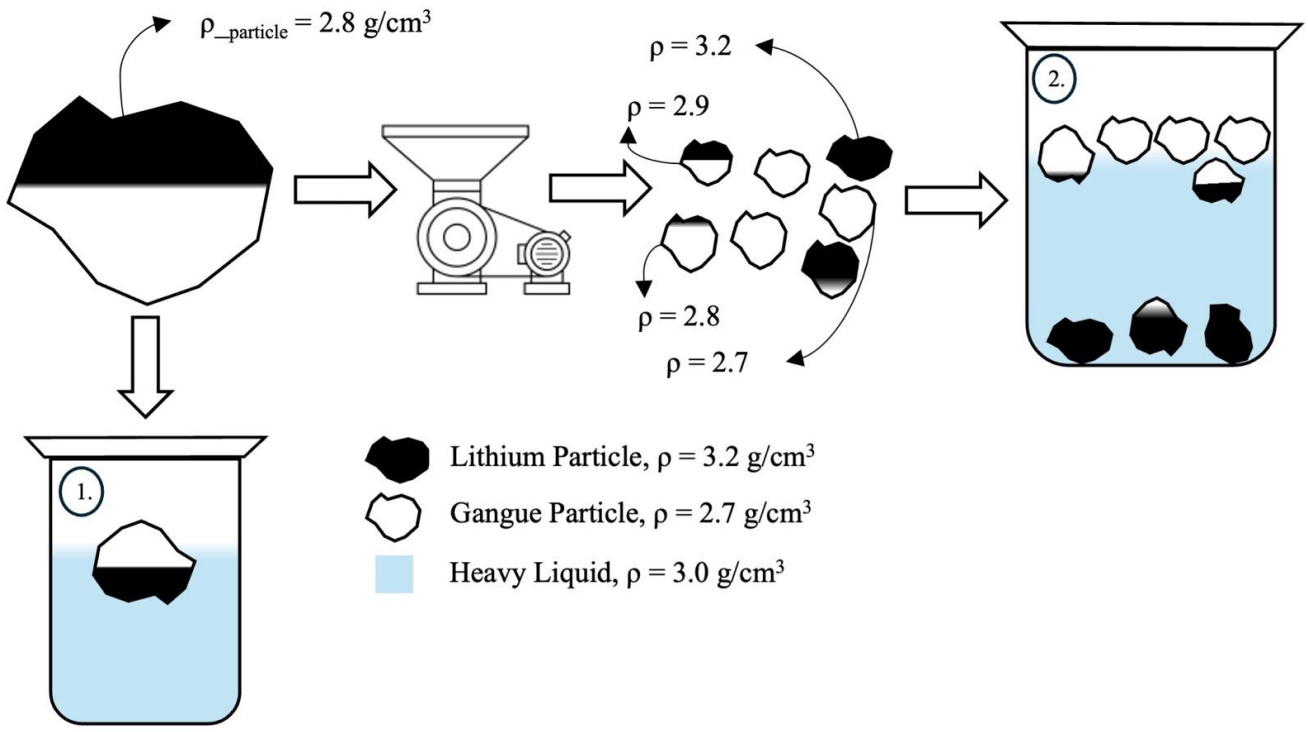

Figure 2.11 The effect of liberation on lithium recovery in HLS test. 1) poor liberation and low recovery. 2) high liberation and high recovery.

2.3.2 Dense medium separation (DMS) and link with HL results

As previously stated, HLS is not used at industrial scale. Rather, dense medium separation (DMS) is the common industrial scale pretreatment process used for separation of minerals based on a media's density, including for pegmatite ores. Since DMS works best if the spodumene is well liberated at big grain size fractions, this process is typically not used in cases where adequate liberation is only reached below 1 mm. If the processed material is already fine and DMS cannot be applied, the flotation only flowsheet can be presented also without this step as presented in Sahoo et al. (2024). There can be one or more pretreatment steps, meaning one or more DMS circuits operating in series (two-stage DMS). This way the cut points of dense media can be adjusted differently for each step, which enables more accurate separation and higher separation performance (Tadesse et al., 2019).

As explained earlier, spodumene beneficiation is a multi-step process that typically combines DMS, magnetic separation, de-sliming, and flotation, with DMS often serving as a pre-separation step before flotation, depending on the deposit's mineralogy (Gibson et al., 2021). A typical DMS circuit is presented with details in Figure 2.12. As observed in Figure 2.12, water is recycled within the process, primarily through wash screens, reducing freshwater consumption and wastewater production. Additionally, a magnetic separator is used exclusively for the recovery of dense media particles, such as ferrosilicon, ensuring its recirculation and minimizing losses.

Typically, ferrosilicon (FeSi) or magnetite, is mixed with water to create a slurry with a specific density. Magnetite suspensions have range from 4.5 g/cm^3 to 5.4 g/cm^3 and ferrosilicon can have densities of up to 6.7 g/cm^3 (Napier-Munn, 2018). These different dense medias can also be mixed together in order to find the optimum cut point. These two media also have the key advantage of being ferromagnetic, which makes it possible to recover the dense media after the DMS by using a magnetic separator. The dense media is recovered after DMS by magnetic separation, which is applied once the mineral particles have been screened out. One drawback of suspended media is that they cannot be used for static separation, since the fine particles would tend to settle, affecting the density and the separation. This explains why HLs remain the main approach used in small-scale laboratory tests.

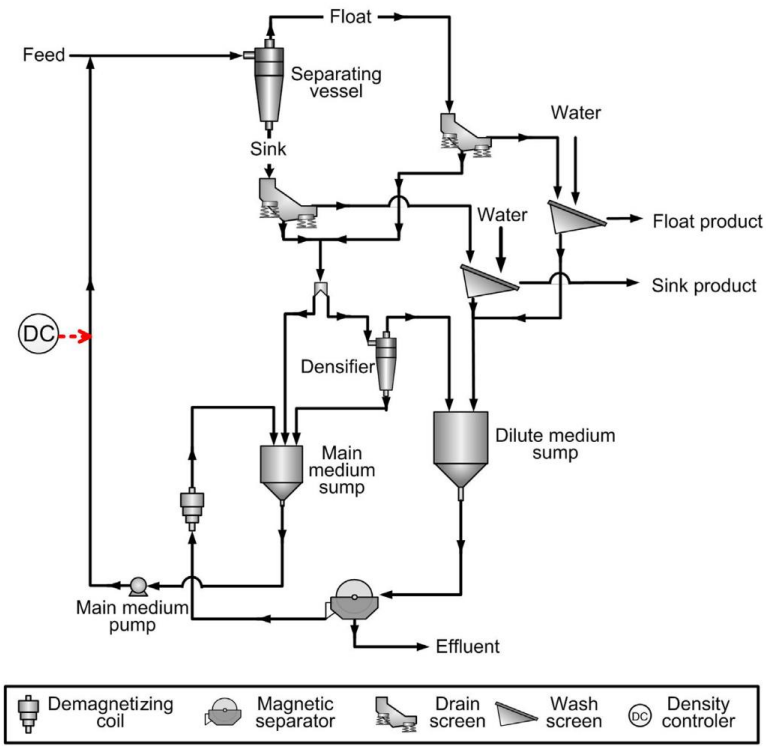

Figure 2.12 Typical DMS circuit (Wills & Finch, 2016).

The DMS process is based on specific gravity (S.G.) differences between the ore and gangue particles. In a DMS circuit, dense media of a known S.G. is mixed with water to produce the medium to be used for separating valuable metals and gangue. This S.G. cut point is a fundamental factor for separation efficiency and needs to be determined accurately for the target mineral. In the case of spodumene ($\rho \approx 3.15$ g/cm^3), separation from the main gangue minerals such as feldspars ($\rho \approx 2.6$ g/cm^3), micas ($\rho \approx 2.9$ g/cm^3), and quartz ($\rho \approx 2.65$ g/cm^3) is relatively easy due to adequate differences in S.G for HLS/DMS context. However, the ore liberation plays a vital role in separation efficiency with a low value reducing separation efficiency (Gibson et al., 2021). In dense medium separation, flat-shaped particles can take significantly longer to settle compared to round-shaped particles. In an even more complicated scenario, if the mineral liberation of a flat-shaped particle is incomplete and denser material accumulates on one side, the particle may behave like a spear, resulting in a much faster settling time than a round particle. Also, the age of dense media can have an effect on the separation performance, owing to the mechanical wear (for example FeSi) particles, which lead to reductions in effective density. Additionally, FeSi can oxidize (corrode) over time, forming iron oxyhydroxide phases, which may dissolve into the medium and alter its

chemical composition and density. Prolonged use can also result in the adsorption of hematite onto FeSi surfaces, affecting its magnetic properties and complicating its recovery (Waanders & Mans, 2003).

Based on Gibson et al. (2021), who conducted DMS tests on lithium-bearing pegmatite dykes from the Hidden Lake deposit (N.W.T., Canada), the DMS circuit reduced the mass sent to flotation by about 50 %, thereby lowering energy consumption and costs. Importantly, the circuit also produced a concentrate, and was not solely used as a pre-concentration step. The study further highlighted that DMS performance is highly sensitive to changes in the media S.G. For example, an interpolated decrease from 2.7 g/cm³ to 2.6 g/cm³, based on HLS results, was predicted to increase the flotation feed mass by 44 %. Therefore, from an economical point of view, the use of DMS as a pre-separation step can decrease the flotation costs, but from an operational point of view, DMS is said to be sensitive to variations in media S.G. (Gibson et al., 2021).

On the industrial scale, DMS is often conducted using hydrocyclones or as they are often referred to in this very context, dense media cyclones (DMC). The early days of DMC date back to the late 1930's in the Netherlands where it was discovered more or less by accident. The local coal company Dutch State Mines (DSM) noticed that a hydrocyclone used to process loess (a clay material) for a dense medium bath in coal cleaning had become blocked. During the cleanup, it was observed that the vortex finder was filled with clean coal, suggesting that the clean coal was being concentrated in the cyclone overflow (Figure 2.13) (Napier-Munn, 2018). The development started and continued, despite the German occupation of the Netherlands, and a patent was applied for in the middle of the Second World War in 1942 (Napier-Munn, 2018).

There are different types of DMCs on the market. The most common is a standard hydrocyclone placed in a more horizontal angled position because this orientation optimizes the tangential feed flow, allows efficient separation of sinks and floats, and provides a compact and practical layout for plant operation and maintenance. The operating principle is the same as that of hydrocyclones used in grinding applications: the high-pressure feed pipe is directed tangentially along the inner surface of the cyclone. Similar to a rifle barrel, the flow follows a spiral path, with dense material moving toward the outer edge of the cyclone and exiting at the bottom. Meanwhile, the lighter particles remain within the center of the fluid vortex and being less dense than the fluid, is discharged through the wider upper end of the cyclone (Figure 2.13) (Ambrós, 2023).

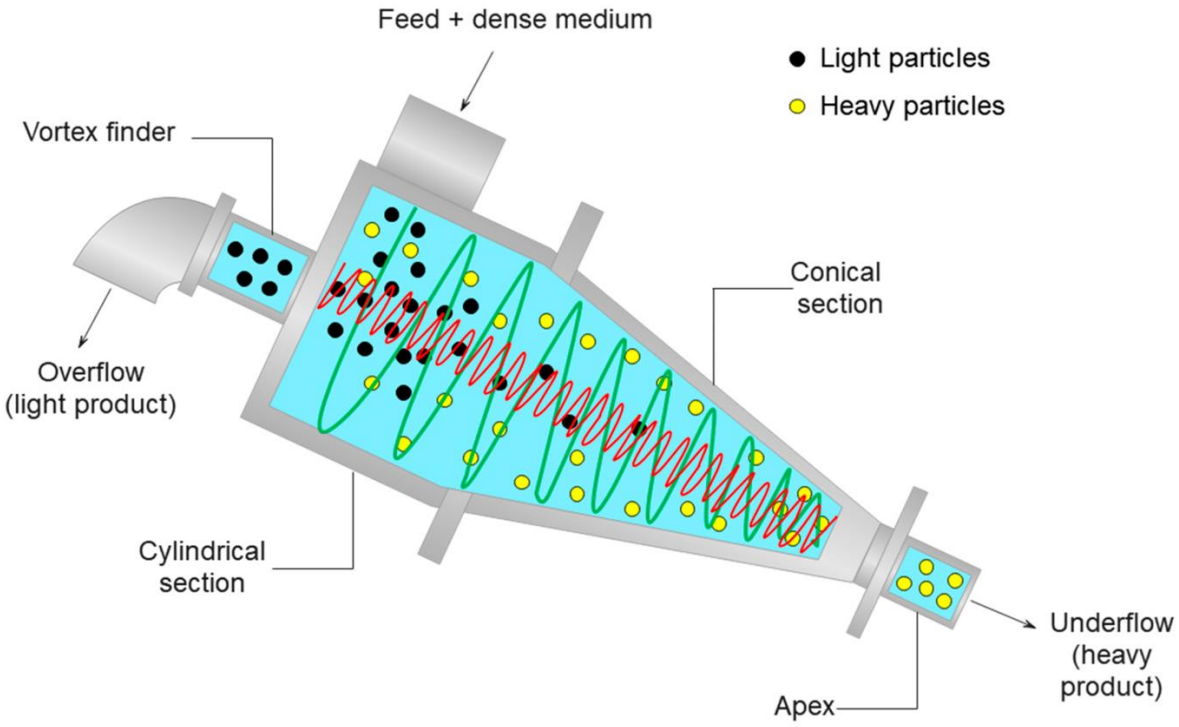

Figure 2.13 Dense medium cyclone (Ambrós, 2023).

Another type of separator is the two-stage equal-density DMC (Figure 2.14). The operating principle of this type of cyclone is similar to the traditional DMC, but instead of having only two outlet streams, it has three products (concentrate, middling and reject). This type of cyclone is suitable for separating the finer particles and is often used in the coal industry. As in the two-product cyclone, the slurry is fed tangentially under high pressure, creating a spiral motion inside. This generates strong centrifugal forces that separate the particles based on their densities. Owing to the geometry inside the cyclone, the materials experience different forces within different portions, which results in three distinct density-based separation zones, heavy fraction, intermediate fraction and light fraction (Wang et al., 2017).

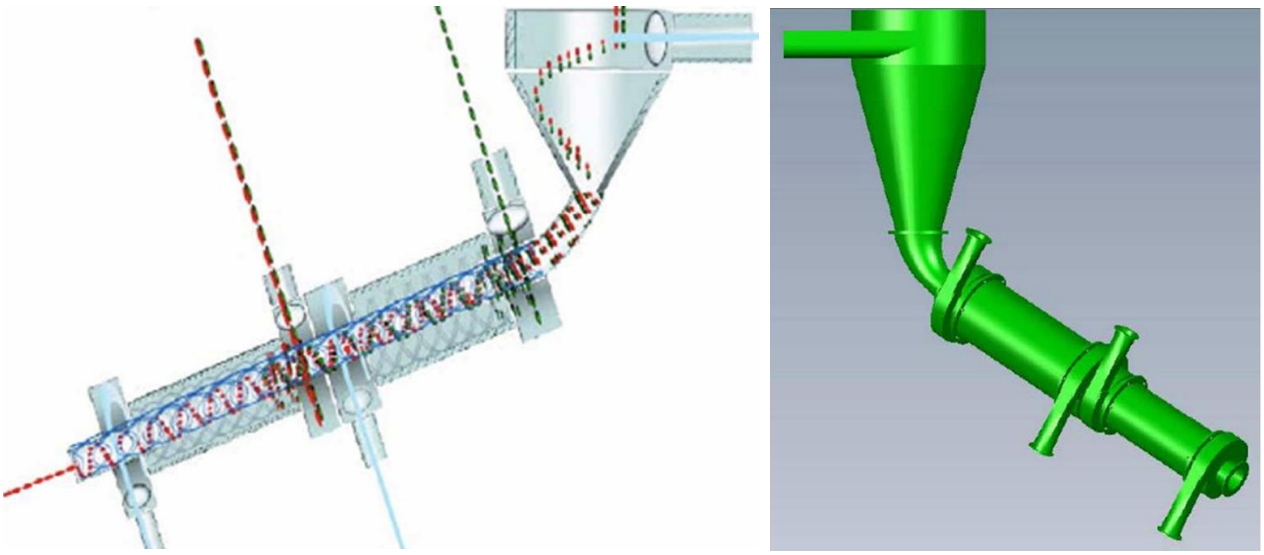

Figure 2.14 Principle of two-stage equal-density dense medium cyclone (Wang et al., 2017).

Like other process equipments, the DMCs also have range of sizes for their use. The sizing of the DMC is a case-specific matter and requires a knowledge of the process in question, as the processed material as well as the planned feed rate will influence the size of the required cyclone. Baruya (2012) reports a few real-life cases where different sizes of cyclones have been installed and used for coal production. In Australia, the biggest cyclones have a diameter as wide as 2 m, a capacity of processing 500 t/h, whereas in South Africa the smallest cyclone diameters can be between 1 and 10 mm (Baruya, 2012).

DMS circuits are largely controlled by the dense medium whose density dictates the cut-point. Thus, choosing the right type of media is extremely important for the effectiveness of the process. As stated above, even a small change in the media's S.G. can cause a large reduction in the grade of the concentrate. Dense media is typically divided into two categories: chemical media and suspended media. The suspended media, where very fine particles (45 to 150 μm) are used (Sahoo et al., 2024; Shi, 2016) can also include finer sizes as reported by Waanders & Mans (2003).

While both HLS and DMS rely on density differences between particles, HLS in laboratory conditions can achieve near-perfect separations due to ample settling time. In contrast, DMS in continuous industrial processes is inherently less efficient due to practical constraints such as limited residence time, the presence of near-density particles, and process factors like particle size, feed rate, vessel design, and medium viscosity. These limitations often lead to misclassification of

particles close to the separating density. HLS is therefore preferred for laboratory testing, where ideal conditions allow for benchmarking and process optimization (Wills & Finch, 2016).

In terms of media and scalability, HLS uses heavy liquids and is suitable for lab-scale applications due to the precision and control it offers. DMS, on the other hand, employs suspended solids (e.g., magnetite or ferrosilicon) and is more practical for large-scale operations. Although heavy liquids can be costly and sometimes toxic, low-toxicity alternatives have been developed in recent years (Figure 16) (Chemical Consulting, 2024).

As mentioned earlier, the mineral liberation of a particle plays a vital role in separation processes. In a perfect world, the ore particles would be completely liberated. Unfortunately, this is never the case in real life applications. In the more common scenario, most of the minerals are adequately liberated to achieve high recovery and grade, while some remain as mixed particles. This phenomenon is called partial liberation. The partial liberation degree depends on many factors, such as the processed mineral (hardness, grain size, etc.) and what kind of preprocesses (number of crushing stages, used grinding media etc.) are used. For a given material or sample, the finer the particles are ground, the higher the liberation. Economics typically drive the compromise between grinding energy expenditure and liberation, to select the best target particle size to achieve the best outcome.

However, excessive grinding can produce problematic amounts of fine particles when targeting high liberation degrees. Instead of improving the separation performance in DMS, grinding can have the opposite effect and decrease efficiency. Ultrafine particles are referred to as slimes, with different studies using different threshold sizes to quantify certain particles as slimes (typically below 20 µm, often below 5 µm). Slimes can cause difficulties in separation owing to the increase in the viscosity of the slurry, which reduces differences in particle settling speeds and, in turn, the sharpness of a separation. The slimes can be removed from the process in a desliming step by using hydrocyclones. In some applications, hydraulic classifiers can give a better outcome since the high shear forces occurring in hydrocyclones tend to cause problems through further degradation of friable minerals (Wills et al., 2016).

A partition curve is a fundamental tool for assessing separation efficiency in density-based processes such as DMS. It plots the recovery of particles as a function of their density, allowing

the estimation of performance and comparison between different separators (Wills & Finch, 2016). In an ideal case (green line in Figure 2.15), all particles with a density lower than the separating density report to the float fraction, while denser particles report to the sink fraction without misplacement. However, in real-life scenarios, separation is not perfect, leading to an error area between the real and ideal separation lines (red and green lines in Figure 2.15). The sharpness of separation, quantified by the slope of the partition curve, directly correlates with separation efficiency. For reference, a perfect separation, such as that obtained using HLS, would result in a vertical line drawn at the S.G. of the heavy liquid.

In spodumene beneficiation using DMS, partition curves help optimize the separation density by evaluating the misplacement of spodumene and gangue minerals. Since spodumene ($\rho \approx 3.2$ g/cm³) is relatively close in density to some gangue minerals like feldspar and quartz ($\rho \approx 2.65$ g/cm³), achieving sharp separation is more challenging compared to high-density contrasts such as gold ($\rho \approx 19.3$ g/cm³). Nevertheless, the density difference is still sufficient for spodumene to be beneficiated using DMS. A well-defined partition curve with a steep slope ensures that spodumene recovery is maximized while gangue misplacement is minimized, ultimately improving the efficiency of the beneficiation process.

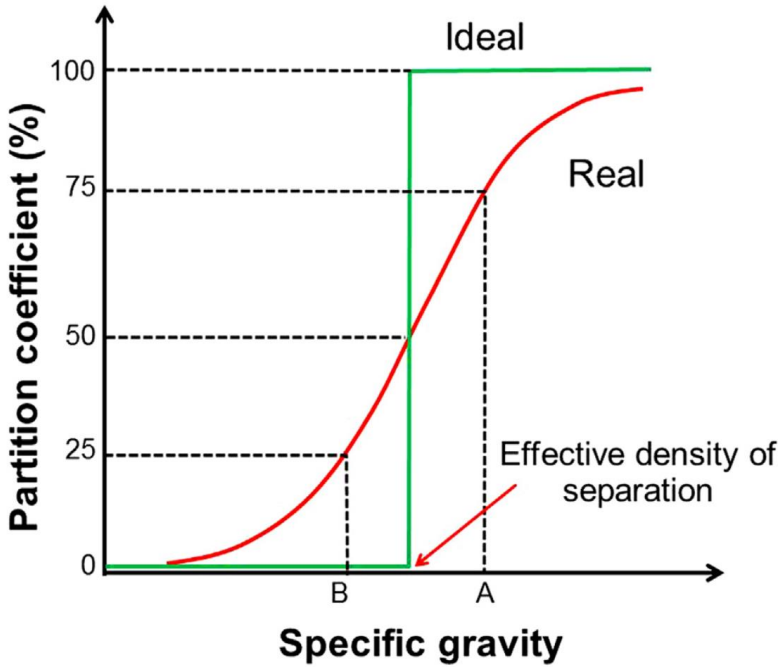

Figure 2.15 Partition or Tromp curve (Wills et al., 2016).

2.3.3 Centrifugal separation (Knelson type) and other proposed gravimetric methods

DMS is not the only available gravimetric method for ore concentrating. Depending on the density of the particle, the shape of the particle and the liberation, other gravimetric separation methods can be applied.

One well-known gravimetric separation method is the Knelson separator which uses a centrifugal force to form a fluidized bed and separate heavy minerals from light ones. Up to 60 times the force of gravity (60 g) affects the particles, with the heavier particles becoming trapped in riffles (a series of rings located in the machine) while the lighter particles are flushed out (see Figure 2.16). The Knelson Separator is typically used with material containing only a small portion (around 0.05% by weight) of dense particles, making it ideal for gold processing (Wills et al., 2016). Higher amounts of heavy minerals would tend to overfill the riffles, reducing heavy particle recovery.

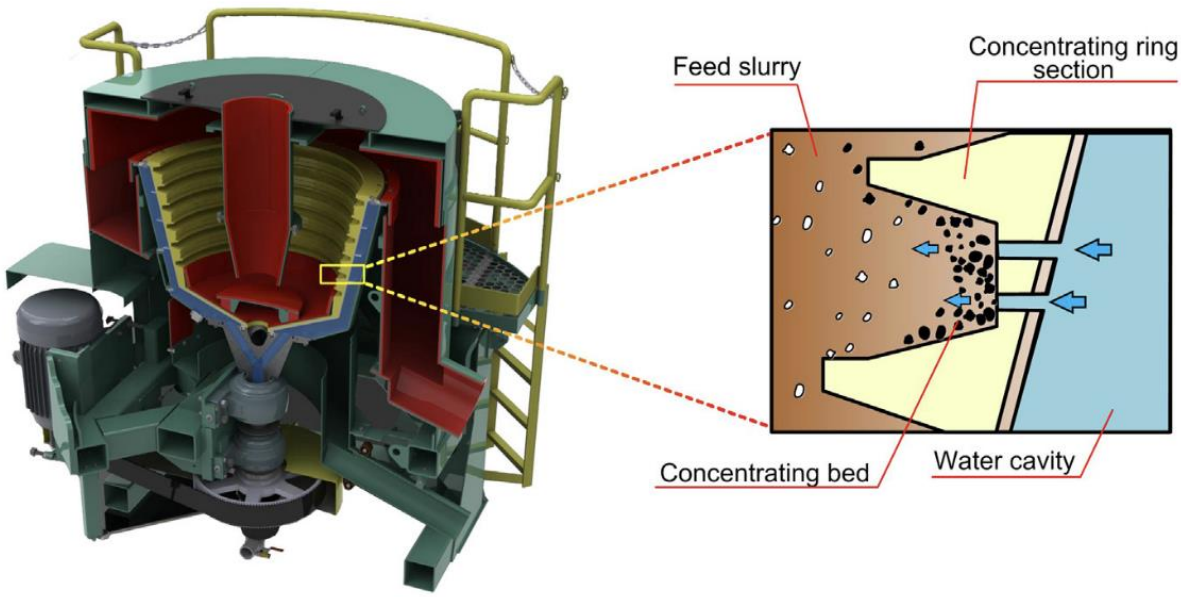

Figure 2.16 Knelson concentrator cutaway; and action inside the riffle (Courtesy FLSmidth) (Wills et al., 2016) .

In terms of operation, the feed slurry is introduced continuously into the concentrate cone through a stationary feed tube. Once inside, the slurry moves to the bottom of the cone, where centrifugal force pushes it outward and up along the cone wall. Fluidization water is injected towards the center of the cone through multiple small holes. This water helps create a concentrating bed by filling the

rings to their capacity while preventing the bed from becoming too compact, an action termed as fluidization. The amount of fluidization water is carefully controlled to ensure the bed is properly fluidized, which is monitored by observing the bed expansion, pressure drop across the bed, and process parameters such as water flow rate and particle movement (Kunii & Levenspiel, 1991). High-specific gravity particles are trapped and held within the cone, while fluidization allows denser particles to replace lighter ones that were previously caught in the riffles. Periodically, when the riffles have filled up, the collected material is flushed out of the cone into the concentrate launder (Wills et al., 2016). Despite the energy efficiency and effective separability of Kneslon concentrator, in the field of spodumene beneficiation it is still quite rarely used likely due to inadequate density difference between spodumene and gangue (Sahoo et al., 2024).

Another centrifugal separator is the Falcon concentrator, whose basic operating principle is the same as in the Knelson, but with the main difference being the centrifugal force, which can reach 200 – 300g for the Falcon (Kundu et al., 2023; Sepro Mineral Systems Corp, n.d.). Thus, the Falcon can operate with finer particles. On the other hand, in spodumene production, the particle size can be fairly large if the liberation allows it. Thus, the Falcon is rarely used as a primary separator for spodumene, but some testwork has been done on the fine particle size fraction as reported by Kundu et al. (2023) and showed that although Falcon concentrator is capable of producing high centrifugal forces (up to 300 g) and is well suited for fine particles, its performance in spodumene beneficiation was limited. The study demonstrated that the Falcon yielded only 1.40% Li_2O in the concentrate from a 1.10% Li_2O feed, due to the low concentration criterion (CC = 1.33) between spodumene and associated silicate gangue minerals. This indicates that the density difference was not sufficient for effective separation at fine particle sizes, reaffirming that Falcon concentrators are not optimal for primary spodumene separation, although they may be useful for recovering lithium from finer fractions in multi-stage processes.

Jigging is another gravity-based separation method where particles are sorted based on differences in their density, size, and shape, utilizing the effect of gravitational forces (Kundu et al., 2023). A jig, as seen in Figure 2.17, is essentially an open tank filled with water, featuring a horizontal jig screen at the top which supports the jig bed. At the bottom, there is a spigot or hutch compartment for removing heavier particles. The jig bed is made up of a layer of coarse, dense particles (called ragging) placed on the jig screen, where the slurry is introduced. As the feed flows across the

ragging, separation occurs within the jig bed. Particles with higher specific gravity pass through the ragging, penetrate the screen, and are removed as the heavy product, while lighter particles are carried away by the cross-flow to form the light product. Key factors influencing this process include the type, density, size, and shape of the ragging material. Jigging relies on a pulsating motion to enhance the natural settling of particles, causing denser minerals to stratify at the bottom while lighter ones rise to the top. This stratification is further aided by the continuous flow of hutch water, which increases the upward water velocity and reduces the downward flow, improving the separation process (Wills et al., 2016). Some laboratory applications for jig machines in spodumene concentration have been reported by Kundu et al. (2023). Their study found that mineral jigging provided promising results, enriching spodumene content up to 3.42% Li_2O, although HLS was found to be more efficient.

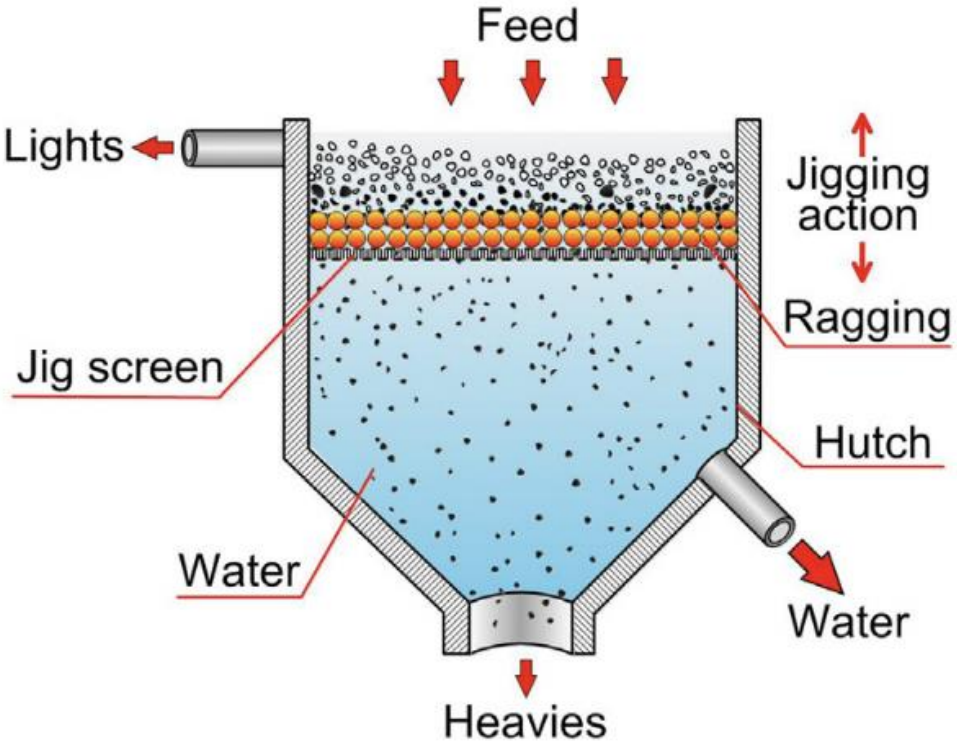

Figure 2.17 Basic jig construction (Taken from (Wills et al., 2016).

2.4 OVERVIEW OF WORK ON LI GEOMETALLURGY IN HARD ROCK

Geometallurgy has become a more and more important field of study during the 21st century. One definition for geometallurgy has defined it as “a scientific discipline in which geological data, mining data, and processing data are co-analysed to generate useful information and knowledge to optimize resource profitability“ (David, 2019). This definition is one possible way to compress a concept as broad as geometallurgy into a single sentence. However, the concept of geometallurgy has changed its meaning and name many times throughout the history of mining, and it will inevitably evolve further as time passes.

2.4.1 Brief description of geometallurgy

While the origins of geometallurgy date back to the 1500s with the early stages of mineral exploration, it did not formally emerge as a word and as a distinct discipline until the late 20th century (Glacialle, 2017). As many other globally recognized concepts, geometallurgy has a variance in its meaning depending on who uses the word in which context. Over the time it has become a broad term, which can be used to describe many sorts of geological measurements and relating them to metallurgical outcomes.

The true meaning of the concept “geometallurgy” is not simply geology and metallurgy as the name may imply, but also embraces the mining. The “geo” in geometallurgy refers to the fact that the ore comes from the ground while the “metallurgy” part refers to all different ways to treat the ore to obtain a revenue stream for the mining company (David, 2019). Geometallurgy requires co-operation and teamwork between different disciplines and a common understanding about all aspects of the project (David, 2019).

Geometallurgy identifies, quantifies, and models ore variability, trying to forecast, optimize operations, and minimize unexpected challenges. By integrating geological, mineralogical, and metallurgical data into an orebody block model, it can support more efficient resource management and more sustainable mining by providing accurate ore characterization data to key stakeholders (Becker et al., 2016; Glacialle, 2017).

Characterizing ore mineralogy across millions of tonnes without statistically averaging its variability is complex, requiring fast, reliable, and cost-effective measurement techniques for large sample volumes (Becker et al., 2016). The demand for geometallurgy has grown due to declining ore grades, increased mineral complexity, volatile commodity prices, and stricter environmental regulations (Glacialle, 2017).

Geometallurgical methods integrate geological and metallurgical data to develop accurate three-dimensional orebody models, allowing for precise predictions of processing performance and reducing technical and operational risks. By tailoring processing methods to ore characteristics, this approach enhances production management, improves scheduling flexibility, and minimizes both environmental impact and unexpected production challenges, ultimately supporting the sustainability and economic viability of mining operations (Butcher et al., 2023; Dominy et al., 2018; Frenzel et al., 2023).

Dominy et al. (2018) proposes a framework for a strategic geometallurgical model. It consists of 4 stages: drilling, testwork, data management and modelling. At the first stage, geometallurgy can be applied for example in core logging, core imaging or down-hole measurements. These actions result in geotechnical and geophysical information, as well as first knowledge of rock type and possible alteration. The testwork stage produces more detailed information about for instance mineralogy (metal/mineral deportment), physical charasteristics (comminution ability, hardness) and recovery (flotability, leachability, gravimetric separation performance). The third stage covers data management where a database is created out of the obtained data. The data validation is also a critical step and performed in this stage. The fourth and last stage is modelling. Here the created databases are combined to form models. Different model types include geological modelling, geostatistical modelling and domain analysis. These models can include information about geology (grade), specific gravity, throughput, recovery and deleterious elements. Depending on the nature of a model, they can be used for numerous purposes, such as financial planning and mine scheduling (Dominy et al., 2018).

The value of geometallurgy arises from more informed resource-to-reserve conversion, followed by improved understanding of orebody knowledge, and finally to more adaptable mine plans and ultimately increasing the project's net present value (NPV) (Dominy et al., 2018). The required

teamwork between different disciplines can also yield non-tangible dividends since different parties are working together and sharing knowledge for common success (Dominy et al., 2018).

2.4.2 Relevant studies on lithium involving geometallurgy

Several studies have explored the application of geometallurgical methods in lithium ore processing, particularly in hard rock deposits such as spodumene-bearing pegmatites. These studies mainly focus on mineralogical characterization, ore variability, and optimization of beneficiation techniques.

A study on the Greenbushes pegmatite deposit (Australia) utilized drill core materials and hyperspectral data to analyze the mineralogical evolution of spodumene-rich zones (Wells et al., 2022). TIMA mineral mapping identified textural changes, spodumene liberation, and elemental variations across ore zones. The study found that spodumene occurs mainly as coarse, elongated grains or smaller irregularly shaped crystals. The efficiency of spodumene liberation is influenced by the degree of intergrowth with quartz and the extent of its alteration. A key observation was the transition from spodumene-rich to sodium-rich albite zones at depths exceeding 120 m, which affects beneficiation performance. These insights help refine recovery strategies by aligning mineralogical characteristics with processing techniques (Wells et al., 2022).

An assessment of spodumene deposits in Mt Cattlin, Bald Hill, Greenbushes, and Pilgangoora (all in Australia) investigated spodumene liberation and its impact on beneficiation. The study demonstrated that spodumene recovery rates exceeding 90% are possible due to its coarse nature in quartz-feldspar matrices. However, partial alteration and spodumene-quartz intergrowths reduce separation efficiency, requiring finer grinding or alternative sorting methods. The findings emphasize the importance of characterizing spodumene textures to optimize flotation and density separation processes (Wells et al., 2022).

A study by Wells et al. (2022) on the thermal behavior of spodumene-bearing pegmatites examined calcination and sulfate roasting effects on lithium recovery. It was observed that mica encapsulation, diffusion constraints, and incomplete phase transformations limit extraction efficiency. The study highlighted that spodumene α- to β-phase conversion occurs between 1050 and 1100°C, and that excessive iron or manganese oxidation can impede roasting efficiency (Wells et al., 2022). These findings are relevant for refining thermal treatment parameters to improve

spodumene processing, but more importantly in highlighting which minerals should be rejected or even avoided by careful choice of mined zones.

Guiral (2018) explored geometallurgical methods for lithium pegmatite deposits, focusing on the Keliber Lithium Project in Finland. The study used image analysis, scanning electron microscopy (SEM), and machine learning to classify spodumene ores into twelve textural categories based on macroscopic and microscopic features. A machine learning model (Random Forest) was applied to predict metallurgical performance in flotation based on these textures, improving lithium grade estimation through automated image segmentation.

A study by Koch (2019), investigated various techniques for lithium ore characterization. Automated drill core scanning using machine learning and image analysis was applied to classify mineral textures and estimate modal mineralogy from drill core samples, improving orebody modeling. Additionally, the study includes the use of different mineral texture classification methods to increase the accuracy of mineral liberation assessments. The research also discusses different ore types based on mineral composition, grain size distribution, and processing behavior, leading to improved predictions for grinding and flotation efficiency. The study also presents a method where mineralogical, geophysical, and chemical assay data are combined using automated drill core imaging and machine learning to build a geometallurgical model that predicts lithium recovery based on ore texture and grain size distribution. A process simulation tool (HSC Sim) was also used to optimize flotation and leaching processes, demonstrating how predictive modeling can support spodumene processing strategies. Table 2.2 summarizes the key aspects of the studies reviewed, including the analytical methods used, the properties assessed, and the predicted metallurgical outcomes.

Table 2.2 Summary of the key aspects of the studies reviewed.

Analytical methods used	**Properties assessed**	**Metallurgical outcome predicted**	**Source**
SEM, hyperspectral imaging, TIMA mineral mapping	Mineral texture, spodumene liberation, elemental composition	Lithium deportment, orebody variability, flotation efficiency	Wells et al. (2022)
SEM, visual assessment, machine learning	Grain size, mineral texture classification	Mineral processing behavior, spodumene flotation recovery	Guiral (2018)
Automated core scanning, image analysis, machine learning	Ore texture, modal mineralogy, grain size distribution	Orebody modeling, mineral liberation, processing optimization	Koch et al. (2019)

2.5 ARTIFICIAL INTELLIGENCE AND MACHINE LEARNING APPLICATIONS IN MINING

Despite the fact that it is discussed in media almost every day, the ease of falling into a pitfall while interpreting and defining what is artificial intelligence (AI) can be deceptive. One could use a simple and concise definition for AI such as "an intelligent machine or device capable of performing tasks and solving problems autonomously". However, upon closer examination, the definition is not a straightforward task to complete after all and requires a deeper understanding of humanity and answers to questions like "What is intelligence?" or "How can one measure intelligence?" (Ertel, 2024). The purpose of this chapter is not to provide a definition of AI but rather to explore basic concepts and functions of different AI related applications particularly those relevant to the context of modern-day mining and mineral processing.

2.5.1 Image processing

An image can be defined as a two-dimensional function, $f(x,y)$, where x and y are spatial coordinates, and the amplitude of function f at any pair of coordinates (x,y) is called the intensity or gray level of the image at that point (Gonzalez & Woods, 2018). Digital image processing refers to the manipulation of digital images using a computer. A digital image consists of a finite number of individual elements, each with a specific location and value. These elements are known as picture elements, image elements, from which the words pels and pixels originate. Among these terms, pixel is the most commonly used to refer to the individual components of a digital image (Gonzalez & Woods, 2018).

It is hard to distinguish between image processing and other related disciplines, such as image analysis and computer vision. Thus, there is no general agreement between authors in terms of where the image processing stops and becomes something else. In some cases, image processing is defined as a discipline where both the input data and output of a process are images but even this is not a comprehensive definition and may limit and become a more artificial boundary than the whole truth (Gonzalez & Woods, 2018). Another mentality regarding the image processing definition is less restrictive and goes as follows: "An image is being processed as soon as information begins to be extracted from it." (Marion, 1991).

Regardless of the exact definition of image processing, images are typically processed due to the need to improve some quality of the images in order to get more or better information out of it. Marion (1991) presents a simple list of things that can be seen as reasons to do image processing.

- The quality of an image may need improvement, either subjectively, to enhance its visual appeal, or objectively, by increasing contrast, sharpening details, clarifying specific areas or shapes, or reducing noise and interference that can hinder information clarity.
- Enhancing image quality can also involve restoring a bad image to its "ideal" state. This includes correcting geometric or photometric issues from camera, minimizing fluctuations caused by atmospheric turbulence, and reducing blurriness from camera shake. Such restoration techniques often utilize various linear and non-linear filters, including inverse filters.
- In some cases, the goal is to detect specific shapes, contours, or textures while disregarding other image details. This process, known as detection, is a fundamental problem in signal theory, where the challenge is to extract a known signal from a background of noise.
- Image processing involves managing large data volumes, where compression optimizes transmission, storage, and equipment use while preserving storage quality. This field covers coding, data compression, and image approximation.
- Image processing enables machines to analyze and interpret images, forming the basis of machine vision and of the application of AI to such tasks. It involves extracting shapes, contours, and textures, segmenting images, and recognizing patterns to support decision-making in robotics and automation.

Naseri & Rezaei Nasab (2023) utilized image processing to automate mineral identification in thin sections. By analyzing color and texture features from images captured under polarized and ordinary light, they applied segmentation and classification techniques. Their machine learning based model achieved 99.25% accuracy, demonstrating that image processing enhances mineral segmentation, reduces manual effort and improves precision in geological studies. Another study

showed a usage of image processing application in mineral processing plant where it was used to monitor froth flotation, using a segmentation method to measure the bubble size and froth stability (Ouanan & Abdelwahed, 2019).

2.5.2 Superpixel segmentation

Segmentation is one among many image processing methods. Segmentation divides the original image into smaller images, called sub-regions or sub-objects from which the relevant information is extracted. The accuracy of the segmentation plays a key role in the final success or failure of the further image analysis (Scott & McCann, 2005).

Image segmentation techniques often rely on discontinuity and similarity. A discontinuity usually represents an abrupt change in intensity, an edge for example. Similarity, on the other hand, can be seen as a region or area whose properties and characteristics are the same based on a predetermined set of criteria (Scott & McCann, 2005). One of the promising methods of segmentation is called superpixel segmentation (Li & Chen, 2015).

The principle behind superpixel segmentation relies on a method where the standard pixel grid of any image is replaced by a collection or group of pixels into primitive regions and areas which are more perceptually meaningful if comparing with individual pixels. The overall objectives of this approach are to reduce the computational load and improve the performance of segmentation algorithms by minimizing the irrelevant details (Gonzalez & Woods, 2018). The following examples of superpixel segmentation characteristics were originally presented by Gonzalez & Woods (2018). One important aspect for feature extraction is how detailed the processed image is. In superpixel segmentation, the main factor that influences the number of details is the number of superpixels. The first example in Figure 2.18a) represents an image of size 1756 × 1790 (3 143 240) pixels including various levels of information and details. Figure 2.18b) illustrates the same image represented by 3000 superpixels and their boundaries (the boundaries are shown for reference, they are not part of the data), and Figure 2.18c) is the superpixel image without boundaries.

One might argue that the level of detail in the superpixel image is sufficient to transmit the same information as the original. However, the superpixel version consists of only 3000 basic units, compared to 3 143 240 in the original. Whether this representation is “adequate” depends on the

specific application. If the goal is to describe the image at a general level of detail, then it is sufficient. However, if the objective is to detect fine imperfections at the pixel level, then it is clearly inadequate.

One key requirement for any superpixel representation is boundary adherence, meaning that the edges between regions of interest must be preserved in the superpixel image. This is clearly demonstrated in Figure 2.18c) where the boundaries remain well-defined. For instance, observe how distinct the edges are between the background wall and the table.

Figure 2.18 a) Image of size 1756 x 1790 (3 143 240) pixels. b) The image consists of 3000 superpixels, with the boundaries between them (in white) overlaid on the superpixel image for reference – the boundaries are not part of the actual data. c) Superpixel image.

As another example, we present the results of brutally reducing the number of superpixels to 1000, 500, 250 and 25. As shown in Figure 2.19, this reduction leads to a significant loss of detail compared to Figure 2.18a). However, the last two images still retain most of the essential details of the original image. One noticeable difference is that the spruce tree and the snowman can only be seen in the last two images, whereas the recognition of these two details becomes almost impossible in the first two images. The first image is useless in terms of recognizing the object in the image, since it is impossible to tell if there is a coffee cup or not. Despite this loss of fine details, the boundaries between the main regions and the overall structure of the image remain intact as can be seen from the first image where the boundary between background and the cup is well defined.

Figure 2.19 Top row: Results of using 25, 250, 500 and 1000 superpixels in the representations of Figure 2.18a). As before, the boundaries between superpixels are overlaid on the image for reference. Bottom row: Superpixel images.

Related studies by Latif et al. (2022) and Maitre et al. (2019) explored the use of superpixel segmentation in mining applications. Maitre et al. (2019) applied this method to mineral grain identification from optical microscopy images of sand. They found that superpixel segmentation improved grain isolation and classification accuracy when combined with traditional machine learning models. However, convolutional neural networks (CNNs) underperformed due to feature extraction challenges and dataset alignment issues. Their findings highlighted the importance of high-quality segmentation for reliable automated mineral analysis.

Latif et al. (2022) extended this approach by integrating deep learning models, such as ResNet, achieving a validation accuracy of 90.5%, outperforming conventional machine learning methods like AlexNet and GoogleNet. Their study demonstrated that deep learning benefits significantly from precise segmentation, though preprocessing remains crucial for maintaining accuracy. Both studies reinforce the value of superpixel segmentation in mineral grain classification, showing its potential to enhance automated analysis while also emphasizing the need for further refinements in dataset alignment and segmentation quality.

2.5.3 Machine learning

Machine learning (ML) is one of the most widely used and trending AI technologies in the modern day world (Suyal & Goyal, 2022). For example, a routine everyday action, such as a Google search, utilizes machine learning even if the user might not know this. Google takes the data based on user's search and by using machine learning, it shows personalized advertisement and search results accordingly (Mahesh, 2020; Suyal & Goyal, 2022). The same principle is applied when searching from YouTube for instance.

In a nutshell, ML is a small part of artificial intelligence. The principle of an ML system (Figure 2.20) is simple: the algorithm requires input data to learn from and ultimately produces an output. In ML, a computer program is trained using input data, and it then produces output data based on that input (Suyal & Goyal, 2022). However, machine learning is not just a computer or algorithm but can also be considered as a field of study that focuses on developing algorithms and statistical models that enable computers to carry out specific tasks without direct programming (Mahesh, 2020).

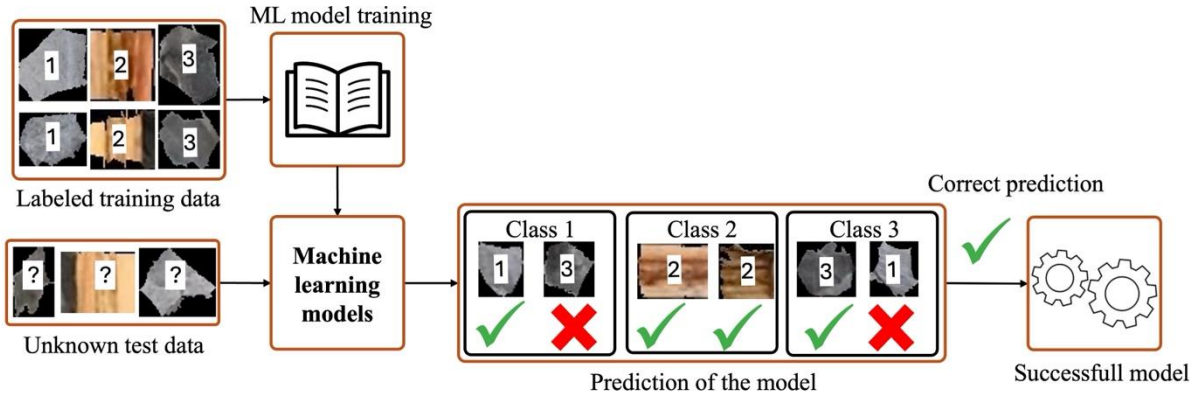

Figure 2.20 A basic principle of ML algorithm.

Machine learning has a wide spectrum of applications and places where it can be used. Typical uses of ML are data mining, image processing, predictive analysis (Mahesh, 2020). ML is a more and more common tool in the modern-day mining industry where it is used for countless purposes. Its applications range from modelling the mineral grade of a given deposit (Kaplan & Topal, 2020) to different applications of mapping of mineral prospectivity (Leite & de Souza Filho, 2009; Rodriguez-Galiano et al., 2015), geological mapping (Cracknell & Reading, 2014; Harvey &

Fotopoulos, 2016), identifying geochemical anomalies (Zuo, 2017; Zuo & Xiong, 2018), drill-core mapping (Acosta et al., 2020; Contreras et al., 2019), mineral grain recognition (Latif et al., 2022; Maitre et al., 2019) and segmenting mineral phases in X-ray microcomputed tomography data (Chauhan et al., 2016; Wang et al., 2015).

Despite the large variety of machine learning applications, there is not just one ML algorithm, but different applications require differently built algorithms to achieve the best outcome. As a generic concept, ML is well-known among various applications, but when diving under the surface, the diversity of different ML structures and methods are revealed. Figure 2.21 represents different types of ML algorithms and gives some examples of each type. The subcategories are presented in order of prevalence, with the most common types on the left and the least common types on the right (Mahesh, 2020).

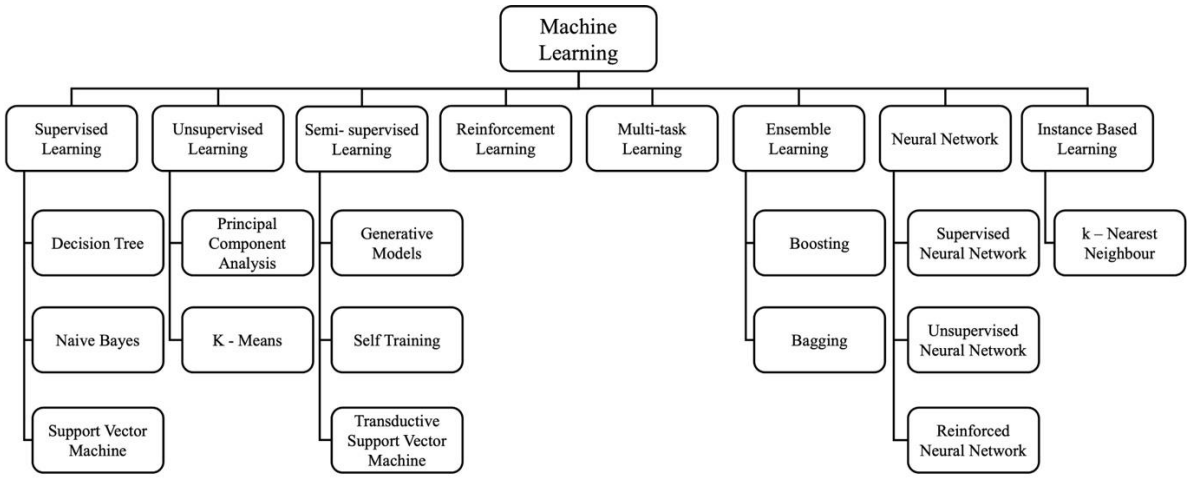

Figure 2.21 Different machine learning algorithms (modified from Mahesh, 2020).

One widely used sub-category of ML is deep learning (DL), which differs from traditional machine learning in its ability to automatically extract complex patterns from raw data using deep neural networks. Unlike ML, which often requires manual feature selection, DL learns hierarchical representations, making it particularly effective for processing high-dimensional data such as images, text, and speech (Janiesch et al., 2021).

2.5.4 Supervised learning

As stated earlier, supervised learning is the most common and essential technique in the field of machine learning. The name refers to the idea of a “supervisor” who instructs the learning system what labels to attach to the training examples (Cunningham et al., 2008). A critical feature of supervised learning is the availability of annotated training data, where labels are typically assigned into particular classes in identification and classification problems. These algorithms generate models from the training data, which can then be used to classify other unlabeled data by learning a mapping between input and output variables (Cunningham et al., 2008; Mahesh, 2020). In this study, supervised learning was selected because the classification of drill core images into mineralogical classes (spodumene, gangue, marker, and undetermined) requires labeled datasets derived from expert geological annotations. The chosen models (CART, k-NN, and Random Forest) are well suited to this task as they are relatively simple, computationally efficient, and require less training time than more complex deep learning architectures, making them practical for iterative experimentation and validation. Moreover, these algorithms can effectively handle heterogeneous features extracted from RGB images, such as superpixel color, texture, and shape descriptors, while also providing interpretable results that are valuable in geometallurgical applications. This approach is consistent with the methodology of Maitre et al. (2019), who applied similar supervised learning models in a comparable mineral classification task.

Supervised machine learning models are those who need external assistance or aid to work properly. Figure 2.22 demonstrates this need since the input data is divided into two categories: training data and test data. As is typical of supervised learning, the training data is labeled. This means that a human has analyzed the data and categorized it into different classes based on its features. Therefore, the training data can be considered perfectly or absolutely correctly classified (Mahesh, 2020).

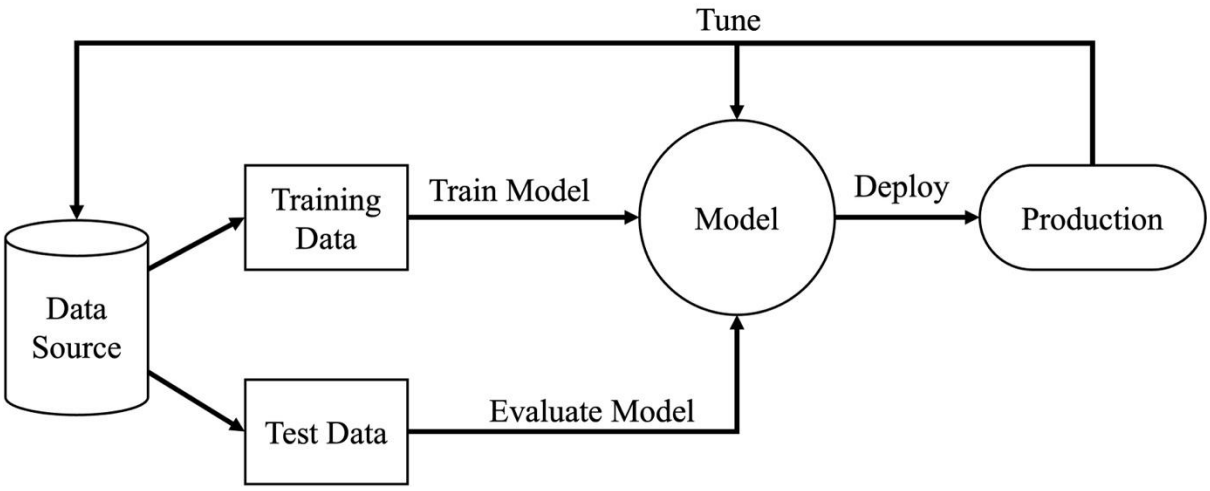

Figure 2.22 Supervised learning workflow (modified from Mahesh, 2020).

Test data in turn can or cannot be labeled depending on the phase of model implementation. In the early phase, where supervised learning models are being created, the test data also requires labels. This way, the performance of the model can be assessed, for example by using typical metrics such as overall accuracy and recall. However, after the learning of the model is finished and the adequate accuracy is obtained, the labeling of the test data is not necessary anymore. In a real application, the model predicts results for new, unlabeled inputs, and these results may be left without manual verification unless there is a specific need to check and update the model with new, correct answers (Mahesh, 2020).

2.5.5 K-Nearest Neighbour (k-NN)

The k-Nearest Neighbour (k-NN) is a simple supervised machine learning algorithm (Halder et al., 2024; Mahesh, 2020) which is also considered as an instance-based learning model (Aha et al., 1991; Halder et al., 2024; Mahesh, 2020). It is typically seen as a subcategory of supervised learning since labeled training data is required. There are also other Nearest Neighbour methods besides just k-NN, but k-NN is most used and well known of these methods (Halder et al., 2024).

The popularity of Nearest Neighbour classification is based on the simplicity and adaptability of the model. The classes are classified based on the class of their nearest neighbour. Typically, classification takes into account more than just one neighbour and thus the name is presented as a k-Nearest Neighbours, where k stands for the number of neighbours which are used for classification (Cunningham et al., 2008).

The k-NN method is sometimes called a memory-based classification since it requires training data at run time, i.e. data needs to be in memory at run time. Because induction is delayed to run-time, it is considered a lazy learning technique. Other names for this method are example-based or case-based classification, since the classification is directly based on the training examples (Cunningham et al., 2008).

The operating principle of Nearest Neighbour methods are based on the likelyhood of similarity. It assumes that similar data points tend to be located close to each other in space. Therefore, the prediction for a new data instance is made based on its proximity to existing instances in the training set (Halder et al., 2024). Figure 2.23 presents a simple, two-class problem in a two-dimensional feature space — an example of the basic principle of the k-NN model. Figure 2.23 shows feature classes O and X as well as q_1 and q_2 which are data points (features) to be classified. The first step is to decide the number of k (number of nearest neighbours) which are used to classify new input data. After that, the distances between the 3 neighbours are calculated, since in the example in Figure 2.23, the k was chosen as 3. Distances between input data (q_1 and q_2) and their nearest neighbours are shown as black lines. The case of classifying q_1 is clear, all of the 3 nearest neighbours belong to a class of O, meaning the q_1 will be classified as an O as well. Classification of q_2, however, is more complicated. Two nearest neighbours for q_2 are members of class X, whereas one neighbour belongs to a class of O. In this case, the classification is not as straighforward as earlier, but the class is chosen by voting between neighbours. Results can be resolved by simple majority voting or by some other voting methods, such as distance-weighted voting where the distance between q_2 and the neighbour is weighted based on how close they are each others. Also, the distance from the “Decision surface” has an impact on classification, since the closer the input data is to the surface, the more confusing the classification will be for the algorithm (Cunningham et al., 2008; Halder et al., 2024).

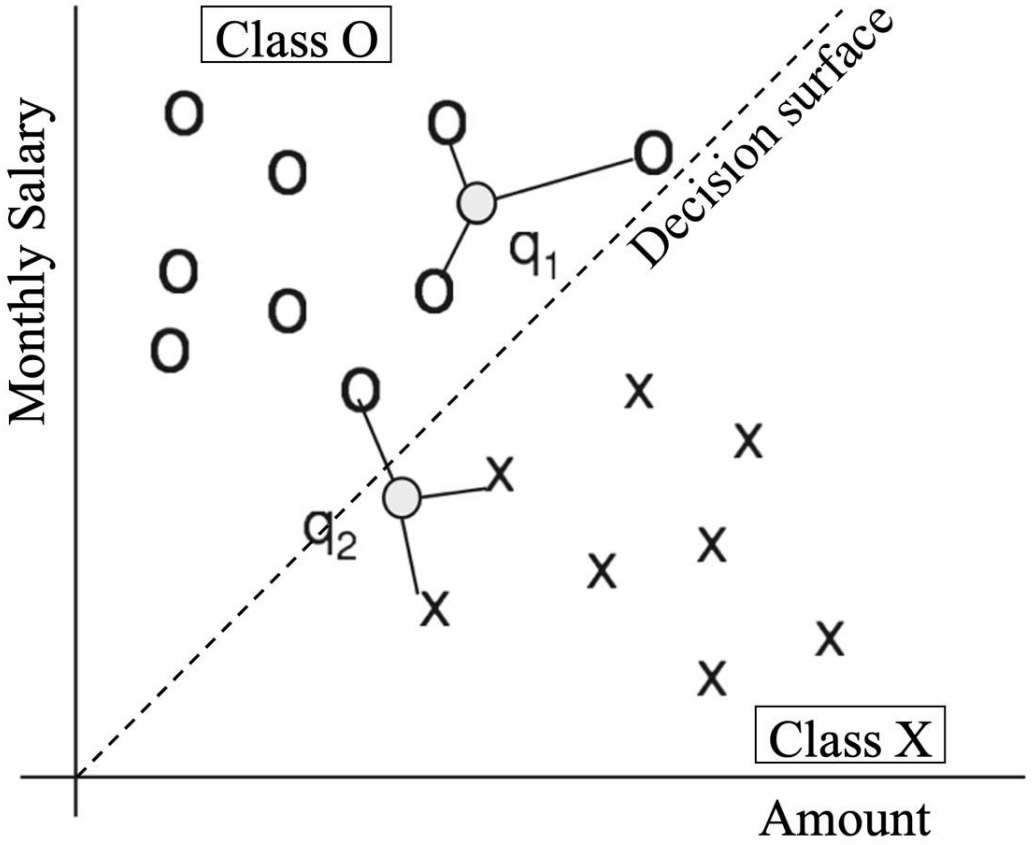

Figure 2.23 A simple example of k-nearest neighbour classification using 3 neighbours. (Modified from Cunningham et al., 2008).

As discussed earlier, the k-NN method is very simple and easy to implement into applications, only the value of k and the distance metrics, such as Euclidean distance (the most common one), Manhattan distance or Minkowski distance needs to be decided. Despite the advantages of this method, there are also some limiting factors which may not make it suitable for all purposes. For instance, the selection of optimal value of k might be challenging in some cases. Computational efficiency and high dimensional data may make the algorithm extremely slow in the case of large amounts of input data. Also, since k-NN is based on the nearest neighbors, it is sensitive to noise and outliers in the data (Halder et al., 2024).

Maitre et al. (2019) investigated the use of computer vision and machine learning for the automated recognition of mineral grains from optical microscope images. Their study proposed an alternative approach using segmentation techniques, feature extraction, and supervised machine learning algorithms, including k-Nearest Neighbors. The k-NN method, being a non-parametric and

instance-based learning algorithm, was assessed for its effectiveness in classifying mineral grains based on extracted features. While k-NN demonstrated reasonable classification performance, it had limitations in handling large datasets efficiently due to its reliance on distance calculations for each new classification. The study concluded that machine learning can effectively identify minerals in particulate materials, offering a faster and more cost-effective alternative to traditional methods (Maitre et al., 2019).

2.5.6 Random Forest (RF)

The Random Forest (RF) algorithm was first proposed by Breiman (2001). Later this algorithm became extremely successful as a general-purpose classification method but also a powerful tool in regression problems (Biau & Scornet, 2016). This method, which integrates multiple randomly generated decision trees and combines their predictions through averaging, has demonstrated outstanding performance in scenarios where the number of variables significantly exceeds the number of observations. In addition, RF is adequately versatile to be used in large-scale problems.

In the same way as k-NN, RF is part of the supervised learning family and thus it requires labeled training data for the best performance. The success of RF traces its roots to the ability of the method to handle a wide range of prediction problems by only adjusting a few parameters. Furthermore, the advantages of this method include a generally recognized high overall accuracy, even in cases where the number of high-dimensional features exceeds the number of samples (training data) (Biau & Scornet, 2016).

As the name implies, a random forest is an ensemble of decision trees. Decision trees, on the other hand, are different mutually independent classifiers which classify subsets of data presented to them (Parmar et al., 2018; Song et al., 2015). Labeled training sets are first randomized by using so called “bagging” method (Bootstrap Aggregating). The basic principle of this approach is to randomly divide the original training data into subsets. In these subsets, the order of the data is random, meaning there can be multiple identical samples, while some samples from the original data may not be present at all. Each of these randomly different subsets is then used to train their own classifier (decision tree). In a RF model, only a random subset of features is used for splitting the nodes (points where data is divided into different branches) of each tree, rather than all features. This increases the diversity of the model and reduces the correlation between the trees. After each

decision tree has reached a conclusion, the final classification result is obtained by voting among the trees. Typically, classification tasks use a so-called majority vote, where the most abundant class wins. However, in the case of regression problems, the voting result is usually determined by averaging the different outcomes from each tree (Cunningham et al., 2008; Parmar et al., 2018; Song et al., 2015). Figure 2.24 illustrates the typical structure of the workflow of the Random Forest classifier.

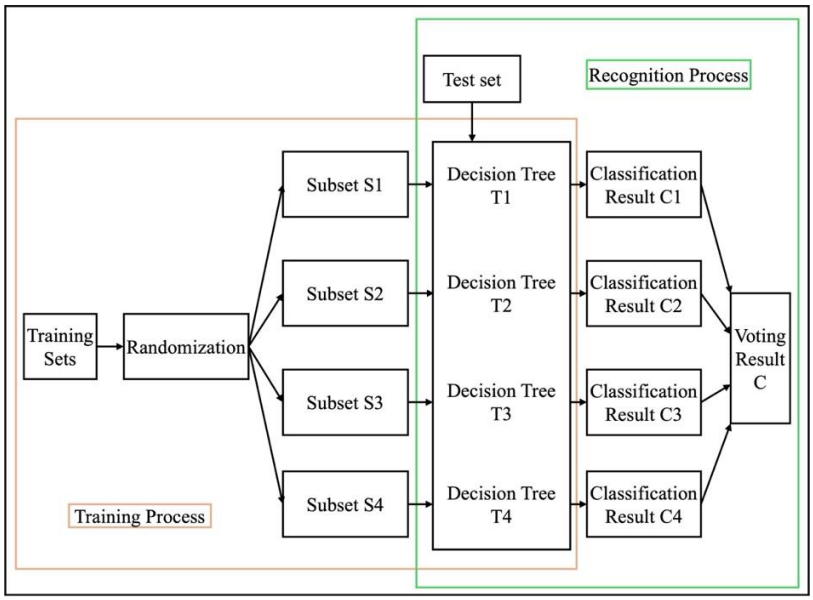

Figure 2.24 The structure of the Random Forest classifier (Modified from Song et al., 2015).

The popularity of RF is most likely due to its high efficiency in terms of processing power. Additionally, the randomization in the Random Forest algorithm greatly improves the classifier's performance. Since each decision tree is constructed quickly, the process of building the entire forest can be parallelized, leading to a significant improvement in classification speed (Song et al., 2015). However, despite the advantages of this model, it has its limitations. Firstly, RF is quite strict in terms of input data. It is built to work on tabular data, so other types of input, such as images, audio, and text, can be challenging. Secondly, RF struggles with categorical variables that have a large number of unique values (high-cardinality categorical variables). When there are too many unique categories, the model may overfit or require excessive computation to find meaningful patterns. Thirdly, RF is less effective when dealing with imbalanced datasets, where one category is much rarer than others. In such cases, the model tends to favor the majority class, leading to poor prediction accuracy for rare cases (Zhu, 2020).

Hood et al. (2018) applied Random Forest for geochemical classification as a way to link altered rocks to their original protoliths. Traditional methods struggle with large datasets, so the study used k-means clustering for grouping protolith samples and RF classification to identify altered samples. RF proved effective, as it handles high-dimensional data, captures variable interactions, and provides confidence levels. The method offered a faster and more objective alternative to traditional geostatistical approaches, though its success depends on high-quality training data and expert validation (Hood et al., 2018).

2.5.7 Classification and regression trees (CART)

Classification and regression trees (CART) is a supervised machine learning algorithm which is not as widely used or well known as the two other algorithms presented earlier. The main principle is based on binary decision tree structure which is built from training data in a recursive way (Maitre et al., 2019). The advantages of this algorithm are the fact that it does not need adjustable parameters or settings to work. The input data can also be numerical values as well as categorical attributes of the dataset (Maitre et al., 2019).

The algorithm's ability to reach a final conclusion (final decision tree) is achieved by following two steps: (1) the construction of the maximum tree and (2) the choice of the right-sized tree (reduction of the maximum tree). In a nutshell, the procedure follows the old rule of divide and conquer, which is used to construct the classification tree (Maitre et al., 2019).

As said before, CART analysis uses binary recursive partitioning, meaning each decision tree node splits into two child nodes. This process repeats recursively, further dividing the data. 'Partitioning' refers to segmenting the dataset into distinct groups. Lewis (2000) originally applied this approach in a different context, but the same classification principle can be adapted to mineral processing. Here, a decision tree model is used to classify spodumene particles in a DMS process based on particle size and density, ensuring efficient separation of valuable minerals from gangue.

In the given example (Figure 2.25), a classification tree is built for spodumene sample classification. The root node (Node 1) contains the feed sample, and first splits based on particle size. As shown in Figure 2.25, feed with a particle size < 0.5 mm is placed in terminal Node -1 and sent directly to flotation. The remaining feed moves to Node 2, where the next criterion is particle

density. Particles with a density < 2.85 g/cm³ go to terminal Node -2 and are sent to tailings, while those with a density > 2.85 g/cm³ go to terminal Node -3 and end up in the concentrate.

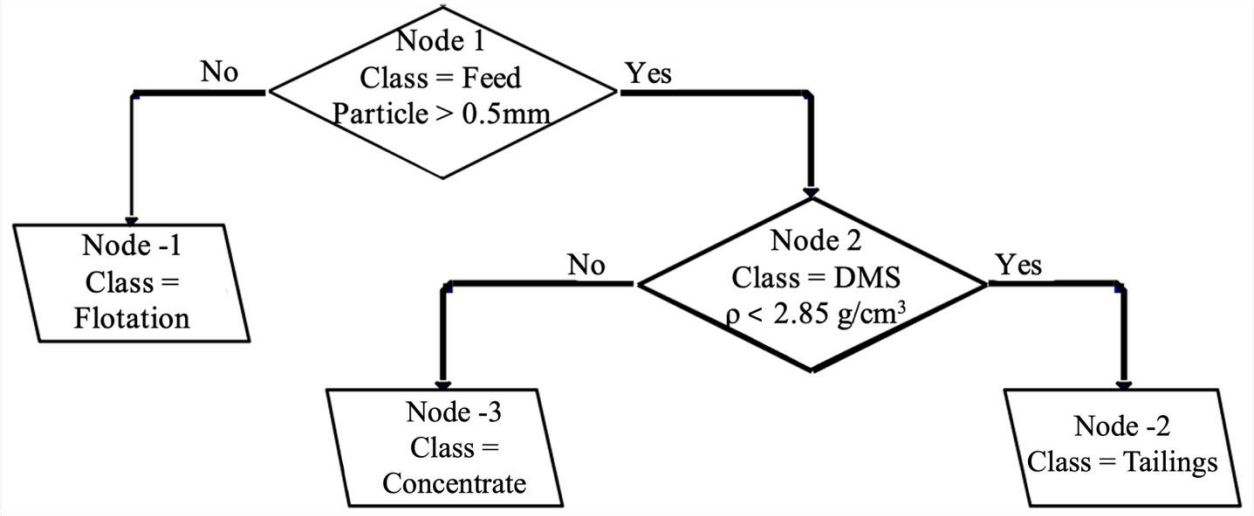

Figure 2.25 The classification and regression tree which results from analysis of the spodumene classification (Modified from Lewis, 2000).

Figure 2.26 below visually illustrates the CART approach. The root node, which includes feed, is split into two. In the first figure on the left, a horizontal line is drawn at a particle size of 0.5 mm. The feed below this line is placed in the first terminal node (Node -1) and sent straightly to flotation circuit. The remaining feed material is further divided by another line (in the second figure on right) at a particle density of 2.85 g/cm^3. Those on the left of this line are discharged to tailings, while those on the right are considered as a concentrate. It is important to note that this second split only applies to the second parent node (Node 2). While this partitioning is easy to visualize with two predictor variables, it becomes difficult or impossible when dealing with five, ten, or more predictors (Lewis, 2000).

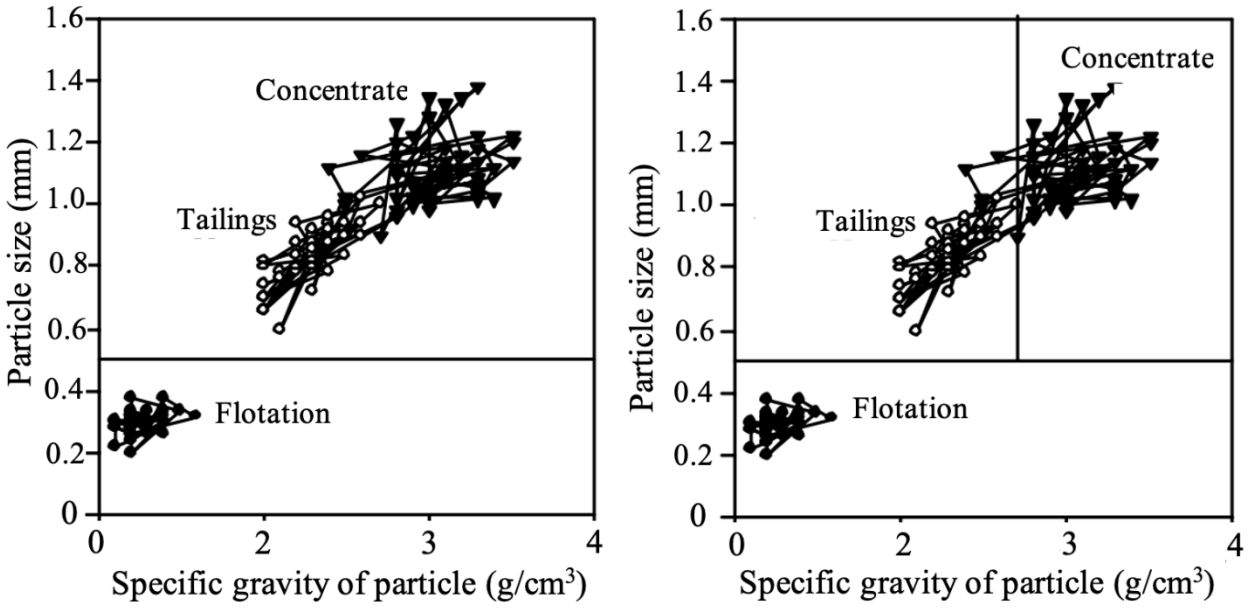

Figure 2.26 A visual illustration of the CART approach (Modified from Lewis, 2000).

In addition to the previous text, other advantages of CART are the ability to handle missing data effectively. Instead of excluding cases with missing predictor variables, CART uses surrogate variables that provide similar information, ensuring that all data points contribute to the analysis and predictions remain reliable. Secondly, the CART analysis is an efficient machine learning method that requires minimal input from the analyst compared to other multivariate models, which often demand extensive adjustments and interpretation (Lewis, 2000). Despite these advantages, the algorithm has also some disadvantages, such as it is not widely recognized, and traditional statisticians may be resistant to adopting it, partly due to skepticism about tree-based methods based on past shortcomings (Lewis, 2000).

Research by Ordóñez-Calderón et al. (2018) applied the CART model to predict alteration facies in the Rosemont Cu-Mo-Ag skarn deposit using geochemical data. A dataset of 882 drill core samples was used to train various machine learning models, including CART, to classify alteration types. The CART model helped segment the dataset by recursively splitting it into decision nodes based on geochemical variables. The results showed that CART provided a clear, interpretable tree structure that helped visualize the classification process. The model successfully identified alteration facies, enabling improved geological modeling compared to traditional visual core logging methods (Ordóñez-Calderón & Gelcich, 2018).

CHAPTER 3 MATERIALS AND METHODS

In this study, a combination of existing data from Patriot Battery Metals (PBM), experimental work by SGS and the author, and data analysis techniques is used to investigate the link between drill core data and HLS test recovery. The methodology includes experimental test work conducted in a laboratory environment as well as numerical modelling and the use of machine learning.

The first part of this study is based on drill core logging data obtained from geologists at PBM to predict the HLS response. The drill core material originates from the CV5 spodumene-bearing pegmatite deposit in the Shaakichiuwaanaan (formerly known as Corvette) Property, Quebec, Canada. The dataset includes a comprehensive characterization of 11 drill cores (Table 3.1), which were analyzed through multiple techniques. The characterization involved visual geological assessment, measured geotechnical parameters, chemical analysis using ICP-MS, and mineralogical analysis via XRD (the latter two being conducted after crushing and grinding of core sections). A detailed sample characterization is presented in a confidential test work report (Aghamirian & Imeson, 2023). Additionally, the company conducted size-by-size basis HLS tests on 16 composite samples (PBM's test work), from the CV5 deposit in an external laboratory, and the HLS Li recovery to sink tests were performed on material crushed to a P_{100} of 9.5 mm. A detailed discussion of these results is provided in the following sections.

Table 3.1 The 11 drill core samples from CV5 deposit.

Composite No.	Drill Hole ID	Interval (m)	Li_2O (%)
Comp 1	CV22-017	9.75	1.4
Comp 2	CV22-019	10	1.16
Comp 3	CV22-025	10	1.14
Comp 4	CV22-035	10.05	1.33
Comp 5	CV22-038	10	1.68
Comp 6	CV22-040	10	0.67
Comp 7	CV22-042	10.05	1.57
Comp 8	CV22-048	9.34	1.35
Comp 9	CV22-052	10	2.04
Comp 10	CV22-054	10	1.2
Comp 11	CV22-070	10	2.73

Another part of the drill core logging process at PBM's facilities is capturing images of each logged drill core. These images can later be used if specific details need to be reviewed. There are two types of images taken: dry images and wet images. Depending on the minerals in question, moistening the drill core surface can improve their visibility. Both wet and dry images are taken after the geologist has logged the cores, and thus, these images also contain notes and marks (with colored grease pencils) on the core surfaces. In this study, only wet images are used due to better visibility of mineral grains. An example of these images is shown in Figure 2.5. These images were taken with an optical camera in a chamber with constant lighting conditions, producing RGB images with a resolution of 4149 × 2780 pixels, weighing 3.9 MB each.

For HLS testing in the course of this thesis, the reagent used was LST heavy liquid, which is a homogenous lithium heteropolytungstates solution with a baseline (initial) density of 2.855 g/cm3. This reagent has a low toxicity, is yellowish clear in color and is easily diluted with water (LST Heavy Liquid SDS, 2016). It is also said to be easy to use at room temperature if the desired

de(Viklund & Aquilina, 2018)/cm3 (Viklund & Aquilina, 2018). HLS tests by SGS were conducted using methylene iodide diluted with acetone on 11 composite samples representing the variability of the CV5 deposit.

3.1 DATA COMPILATION AND STANDARDIZATION

The aim of a geometallurgical model is to establish a link between the ore characteristics and the mineral processing results. For example, defining the link between grain size and mineral liberation or mineralogy and crushability. In order to determine these parameters during drill core description for an entire deposit, a fast, cheap and easy geometallurgical tests need to be developped in order to define domains within the deposit that have distinct characteristics. In our particular case, the objective is to analyze the drill core logging data more thoroughly and identify correlations with HLS test recovery. The standard approach often includes the creation of a numerical model, that helps determine the dependencies in question.

The given dataset for the 11 composite samples consists of 11 core intersections, each containing approximately 10 meters of core from different depths. These core intersections are within pegmatite dykes that have been visually characterized by geologists in a systematic way. Core is usually sampled at approximately 1-meter intervals for chemical and XRD analysis. PBM geologists follow a standardized method for logging to minimize discrepancies between individuals. A way they do this is by providing semi-quantitative classification ranges for certain geological features, such as grain size (<2 mm, 2–7 mm, >7 mm) or inclusions in spodumene (<25%, 25–50%, >50%). Other parameters, such as RQD (Rock Quality Designation) and fracture frequency, are quantitative and therefore should not vary between geologists (see section 2.1.2).

As part of standard practice in this study, data standardization is applied for each parameter prior to analysis. In addition, certain characteristics such as spodumene alteration intensity are recorded as estimated ranges rather than fixed values. For example, alteration intensity may be given as 5–20%, meaning the actual intensity likely falls within that interval. Considering the highly variable grain size and texture in the pegmatite dykes, evaluation of some of these parameters can be quite challenging. Weighted average values for the core intersections used to create the composite samples were calculated in order to compare with HLS test results.

The construction of the database began by averaging the available variables, such as “Spodumene alteration intensity” simply by taking the average of the class. For instance, if the value was 5-20%, the average would be 12.5%. Next, all the data from the drill core intersection is weighted averaged since the length of each sample is not always 1 meter in length. The formula for weighted average (WA) calculation is presented as follows:

$$WA = \frac{SUMPRODUCT(length\ of\ core, variable)}{SUM(length\ of\ core)} \tag{3.1}$$

In a nutshell, equation 3.1 calculates the weighted average of the "variable", where each "length of core" serves as the weight for its corresponding "variable" value. This approach ensures that the contribution of each "variable" value to the average is proportional to its associated core length.

While analyzing data obtained from geologists, it is noteworthy that all the variables should not be handled the same way due to the different number of factors affecting each variable. For instance, in terms of calculating the weighted average based on the length of the core, the variable “RQD”, which is an indication of the hardness of the rock, has only one affecting factor: the length of the core. However, that is not the case for every variable, and thus, for example, in order to calculate a comparable weighted average for spodumene percent dependent parameters such as “Spodumene Alteration Intensity”, “Spodumene Inclusion %” and “spodumene grain size”, the length of the core and the percentage of spodumene need to be taken into account. In other words, the core length for each sample varied, as did the percentage of spodumene. Therefore, these multifactorial variables need to be standardized to ensure comparability with other variables. Consequently, the standardization method for these variables is as follows for the ‘Spodumene Alteration Intensity’ sample:

$$Stantardization = \frac{\sum(Spd\ Alteration\ intensity\ \cdot\ Length\ of\ the\ core\ \cdot\ \%\ of\ spodumene)}{\sum(length\ of\ the\ core\ \cdot\ \%\ of\ spodumene)} \tag{3.2}$$

Equation 3.2 calculates the standardized value of spodumene percent dependent parameters, where each value is weighted by both the core length and the spodumene percentage. This method ensures that the standardization accounts for variations in both core length and spodumene concentration, providing a more representative measure.

3.2 EXTERNAL HLS TEST WORK DATA

Additional characterization test work was conducted on behalf of PBM in an external laboratory for 16 samples (different from the mentioned 11 cores composite samples) from the CV5 deposit. The external laboratory provided a report containing data of performed HLS tests and the XRD info. The goal was to use these data to get a better understanding of spodumene liberation and how the lithium is distributed between different size fractions as well as validate the performance of the prediction models. Table 3.2 summarizes the origin of each sample, the operator responsible for the HLS testing, and the heavy liquid used.

Table 3.2 Sample origin, test operator, and heavy liquid used in HLS testing for each composite sample.

Sample ID	Sample source	Test conducted by	Heavy liquid used
Comp 1	CV22-017	SGS	Methylene iodide
Comp 2	CV22-019	SGS	Methylene iodide
Comp 3	CV22-025	SGS	Methylene iodide
Comp 4	CV22-035	SGS	Methylene iodide
Comp 5	CV22-038	SGS	Methylene iodide
Comp 6	CV22-040	SGS	Methylene iodide
Comp 7	CV22-042	SGS	Methylene iodide
Comp 8	CV22-048	SGS	Methylene iodide
Comp 9	CV22-052	SGS	Methylene iodide
Comp 10	CV22-054	SGS	Methylene iodide
Comp 11	CV22-070	SGS	Methylene iodide
PBM-Comp001	CV23-160A CV23-161 CV23-172 CV23-176 CV23-190	SGS	Methylene iodide
PBM-Comp002, LG	CV23-182	SGS	Methylene iodide
PBM-Copm003, HG	CV23-184	SGS / Author	Methylene iodide / LST

Originally, PBM's test work was conducted on 16 different composite samples (PBM-Comp001 to PBM-Comp016), where "PBM" stands for Patriot Battery Metals. However, since samples PBM-Comp004 to PBM-Comp016 are variability samples and are beyond the scope of this thesis, they are not discussed in this study. Samples PBM-Comp001 to PBM-Comp003 were sieved into five different size fractions using sieve sizes of 9.5 mm, 6.3 mm, 3.3 mm, 1.7 mm, and 0.6 mm.

Additionally, as can be seen in Table 3.2, sample PBM-Comp002 represents low-grade pegmatite, whereas PBM-Comp003 is high-grade material, and PBM-Comp001 is a composite sample representing the average of the two.

For each of the size fractions mentioned above, HLS tests were conducted using a heavy liquid (methylene iodide, diluted with acetone) at eight different specific gravities (S.G.), starting from an S.G. of 3.0 g/cm^3, and processing the collected float (light) fraction progressively, decreasing by 0.5 S.G. units at a time until an S.G. of 2.65 g/cm^3. This approach separates minerals into both size and density fractions.

3.3 LABORATORY TEST WORK

The laboratory test work conducted can be divided roughly into two categories. The main focus was on the HLS testing and related preparation work, mostly crushing, and sieving. The other part of the laboratory phase was the sample characterization using SEM analysis and optical microscopy, as well as a centrifugation test to evaluate the applicability of this method for treating fine (-0.63mm) particles. The goals of these tests were to provide more information on spodumene liberation, the crushability of spodumene compared to quartz and other gangue minerals and also to quantify how Li is distributed between size and density fractions after crushing.

3.3.1 Sample preparation

The material used for HLS testing was stage-crushed to a P_{100} of 12.7 mm top size as explained earlier (see the materials description in CHAPTER 3). From the 1 kg high-grade sample (PBM-Composite003), a sub-sample was taken based on visual mineral abundance and manually sorted using tweezers. The sorting was based on visual color differences between the minerals. To enhance this contrast, the sample was first rinsed in water, which removed dust and surface impurities, making the spodumene appear whiter and the quartz grayer. This color difference is clearly visible in Figure 3.1, where the whiter particles at the bottom are most likely spodumene (also some feldspars can be present), the dark gray particles on top are gangue (mostly quartz, but also some black tourmaline and muscovite), and the middle layer contains unliberated mixed grains, where the color varies from white to gray.

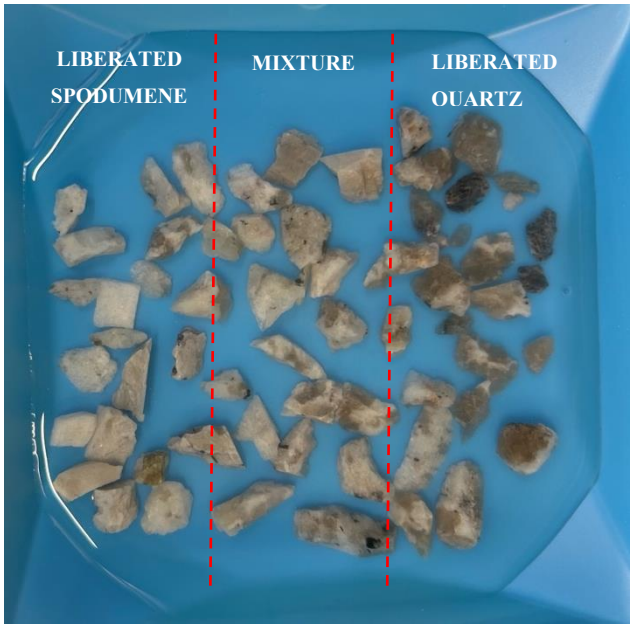

Figure 3.1 Color difference between grains (P_{100} of 12.7mm). White grains on the left are spodumene and dark gray particles are quartz. Between, are the unliberated mixture particles.

The goal of this approach was to divide the sub-sample into four distinct groups based on these visual observations and conduct HLS testing on a size-by-size basis in order to better understand mineral liberation. The four groups are: liberated spodumene (LS, >75% spodumene), liberated quartz (LQ, >75% gangue), mixed grains with a dominant spodumene component (mixed spodumene, MS, 40-75% spodumene), and mixed grains with a dominant quartz component (mixed quartz, MQ, 40-75% gangue). This manual pre-classification allowed the creation of an artificial sample set to investigate how spodumene is liberated and at which density fraction it tends to be found. Furthermore, this approach helped assess the effect of mineral liberation on the outcome of HLS testing. Lastly, the approach allows a qualitative assessment of the differences in breakage and liberation characteristics for different mineral classes. It should be emphasized that precise mineral identification was not essential at this stage, as the purpose was to examine general liberation behavior and its relationship to density separation, rather than to quantify exact spodumene content.

As the manual sorting went further, the grains were classified into four groups as shown in Table 3.3. The spodumene and quartz/gangue groups have fairly different colors whereas a slight general difference in color is present among the mixture samples (with large spodumene or quartz component).

Table 3.3 The result of manual grain (-12.7mm +10mm) sorting from the high grade composite sample (PBM-comp003). Table shows the name, abreviation used in the text, graphical illustration and the real life image.

Liberated Spodumene	Mixed spodumene
LS	MS
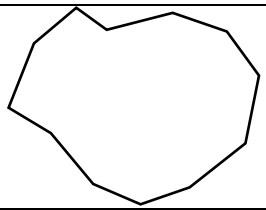	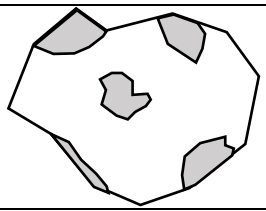
	
Mixed quartz	Liberated quartz
MQ	LQ
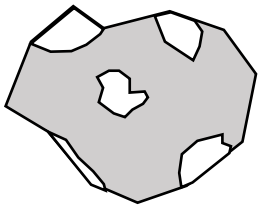	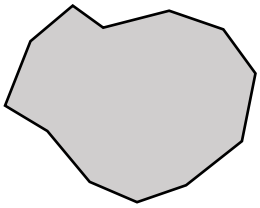
	

After the manual sorting was done, the grains (initially P_{100} of 12.7mm) were crushed to a top size of 9.5mm, typical of HLS test work performed for PBM's project. A laboratory-scale cone crusher with a feed hopper was used (Metso Minerals, Marcy GY-Roll Crusher) (Figure 3.2). The crusher is also attached to a dust extraction system, which mitigates the released dust in the air.

Figure 3.2 Metso Minerals Marcy cone crusher.

The crushed product falls into a product tray located under the mantle. Before starting the crushing process, the closed side setting, which determines the top size (the largest grain size that can pass through the crusher), is adjusted, after removing the bolts next to the feed hopper. Turning the metal disc clockwise decreases the closed side setting, whereas turning it counterclockwise increases it. This machine does not have any indicator which would tell the closed side setting, but the adjustment is based on visual assessment of the gap. Thus, some extra rock samples were used, as a test, to determine the right closed side setting.

After the crusher was adjusted, each of the four samples, weighting roughly 100g, were placed into the feed hopper separately (four crushing runs were performed). Between each run, the crusher was

cleaned by using compressed air to remove fine particles from the mantle, in order to recover the material as well as possible. This also mitigates the cross contamination between samples.

A common standard practice in the field of crushing and particle size analysis is to model crushing behavior based on sieving results. One objective of this testing was to assess how spodumene and quartz break relative to each other and to select the most suitable model for predicting particle size distributions. One of the most commonly used models is the Gates–Gaudin–Schuhmann (GGS) method (Wills & Finch, 2016), which can be mathematically presented as follows:

$$P = 100 \cdot \left(\frac{X}{K}\right)^{\alpha} \tag{3.3}$$

where,

P = Cumulative passing

X = Particle size

K = Top size (theoretical)

α = Distribution coefficient

Another method called Rosin-Rammler-Sperling (RRS) (Alderliesten, 2013; Wills & Finch, 2016) is also widely used in presenting the results of sieve analysis, which in this research were done after the HLS test work. This method has shown to obey the following relationship:

$$P = 1 - e^{-\left(\frac{X}{X_0}\right)^{n}} \tag{3.4}$$

where,

P = Cumulative passing

X = Particle size

X_0 = Particle size at which 63.2% of the material passes through the sieve.

n = Spread parameter of the distribution.

One objective behind HLS testing in the laboratory is to gain an understanding of spodumene liberation in each variety of sample. These size-by-size HLS tests provide insights into the impact of particle size and, therefore, deliver information on mineral liberation, which in turn indicates the optimal top size to which the ore should be crushed. Figure 3.3 illustrates the main idea behind the size-by-size HLS tests. The goal is to find an optimal particle size for maximum liberation without losing recovery due to excessively fine production, since the finest fractions bypass DMS.

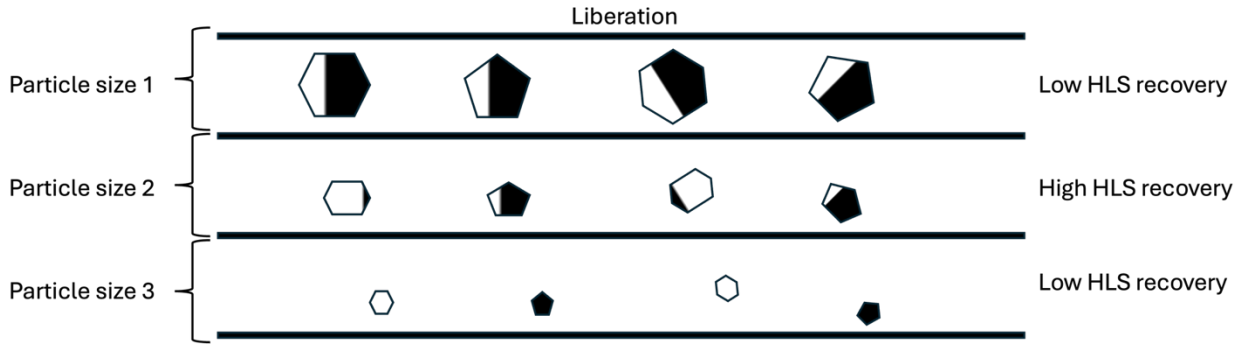

Figure 3.3 Determination of optimal particle size for HLS tests.

3.3.2 HLS Testing

Heavy liquid separation (HLS) tests were conducted using three different heavy liquid (HL, LST in this case) densities (3.0 g/cm^3, 2.85 g/cm^3 and 2.7 g/cm^3), to evaluate the distribution of spodumene between size-density fractions, which should relate to their liberation. The HL used had an initial density of 2.85 g/cm^3 and was used as-is for one of the tests. Different densities were prepared and measured before each separation test using a small (10 ml) volumetric flask and a scale to determine the exact density each time, following the formula $\rho = m/V$. The density of the HL was adjusted by diluting the original HL by adding 8.8 ml of water into a 100 ml of HL, resulting in a HL at density of 2.70 g/cm^3. This value was calculated by using equation 3.5:

$$V_{\text{diluted}} = V_{\text{initial}} \cdot \frac{\rho_{\text{final}} - \rho_{\text{initial}}}{\rho_{\text{water}} - \rho_{\text{final}}} \tag{3.5}$$

where,

$V_{diluted}$	=	Total volume of diluted HL
$V_{initial}$	=	Initial HL volume before dilution
ρ_{final}	=	Desired final HL density after dilution
$\rho_{initial}$	=	Initial density of the HL before dilution
ρ_{water}	=	Density of water

The higher HL density of 3.0 g/cm^3 was obtained by heating the HL to evaporate water. However, evaporating the water was notably more difficult to execute due to the saturation factor of LST HL. As indicated in Figure 3.4, the saturation curve shows a maximum density that can be reached at certain temperatures. In other words, the density of 3.0 g/cm^3 can be obtained if working above 30°C. Laboratory conditions were not suitable for handling HL at density of 3.0 g/cm^3 and thus special arrangements were required.

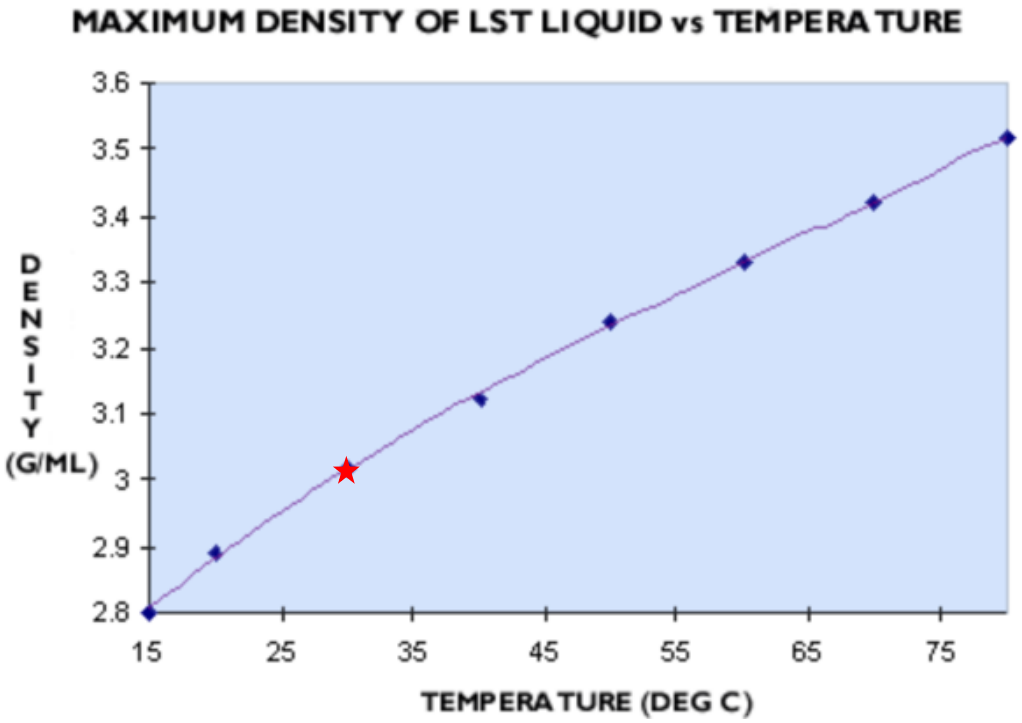

Figure 3.4 Saturation curve of LST heavy liquid indicating the temperature and density at that point (Central Chemical Consulting, 2024).

Firstly, 100 ml of HL was measured into a 150 ml beaker and placed in a drying oven set to a temperature of 60°C. Another method previously used for heating the HL involved a hot plate, but based on previous experiences, handling the reagent on a hot plate is much more demanding since the heat comes from under the beaker, causing uneven heating, with the bottom of the beaker being hotter than the surface. In contrast, in the oven, heat is distributed evenly from all directions around the beaker, resulting in a more consistent overall heat transfer. This way, the impact on density caused by crystallization was mitigated even though the required time was much longer.

The workflow of these HLS tests was as shown in Figure 3.5. Each of the four sample types was crushed and roughly 50 g of each sample was used for the tests. This relatively small sample size was chosen due to limited sample availability and to conserve HL, of which only a small amount was available. Therefore, the smallest available beaker that could accommodate the perforated recovery scoop was used to ensure the HL surface level remained high enough for effective separation, while minimizing HL consumption. Specifically, this setup allowed the HL level to be sufficiently high for the sink fraction to settle and the float fraction to be visible, facilitating recovery using a plastic scoop. Firstly, the samples were introduced to HL at a density of 3.0 g/cm³ while maintaining temperature. After 10 minutes, the sink fraction was collected. Then the float fraction was used as a feed for the 2.85 g/cm³ density test. Similarly, the next float fraction was used as a feed in the last HLS test at a density of 2.7 g/cm³. Finally, all fractions of each sample (4 samples × 3 sinks and 1 float) were sent to the sieving phase.

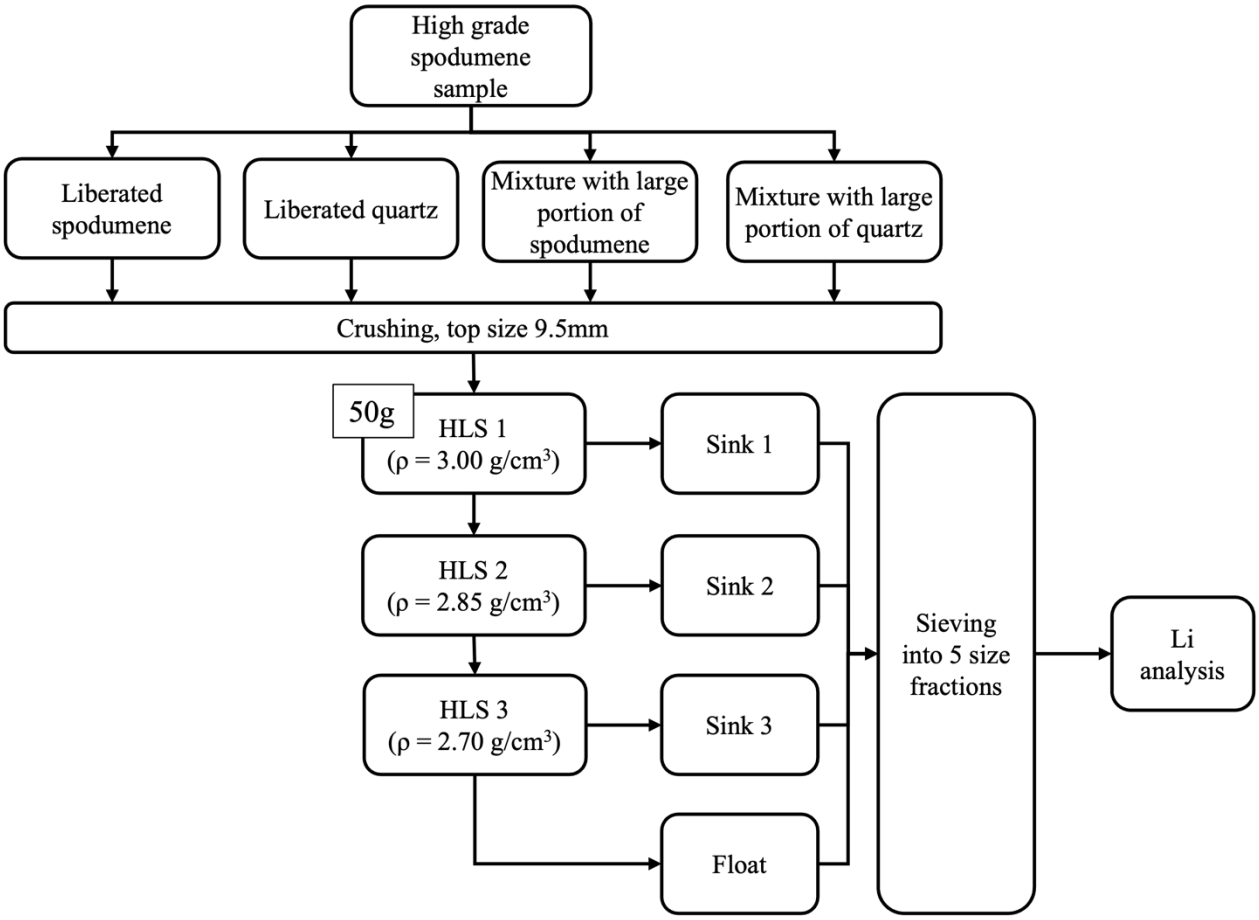

Figure 3.5 Workflow of HLS tests.

In the oven, the HL reached the target density after approximately 4.5-5 hours, and then the HLS test work could be started. However, due to the saturation factor mentioned earlier, the tests had to be conducted quickly and partially inside the oven to mitigate crystallization and to obtain results that were as representative as possible. The heated beaker was taken from the oven, and both the sample and the heated HL were added to the beaker. After quickly mixing the HL and the sample, the beaker was placed back into the oven, where the actual separation occurred.

The density of the HL was monitored during the tests and adjusted as required after each test. A 10 ml volumetric flask was kept in the oven to ensure it was at the same temperature as the HL and to mitigate crystallization. The 60°C HL was pipetted into the volumetric flask inside the oven until the surface reached the meniscus. Then the mass of the flask was measured, and the density was calculated using formula:

$$\rho = \frac{m}{V} \tag{3.6}$$

Where ρ is density in g/ml, m is the mass of HL in grams and V is the volume of the HL in ml. Density control plays an important role in HLS, especially if the tests are done inside the oven, where the evaporation of water is accelerated. Additionally, at lower densities, the density can change due to the moisture in the samples. The float fractions were not fully dried between tests at different densities, and thus, any remaining water could have diluted the HL if not monitored.

After roughly 10 minutes of separation, two phases were visible, and the process was considered complete, as shown in Figure 3.6. The fractions were recovered using a plastic scoop strainer and then placed in their respective sample plates. These plates were filled with water to prevent the HL remaining on the surface of the particles from crystallizing. The same method was applied to the scoop strainer and other tools, which were placed under water when not in use. After the separation, all the tools, as well as the sink and float fractions, were rinsed with a sufficient amount of water to remove any remaining HL, thus preventing crystallization.

Figure 3.6 Completed HLS test showing a clear separation of particles into sink and float fractions.

The next step was to determine the particle size distribution for these samples by sieving in order to see their crushability. The size fractions used were the same as PBM's HLS tests to be able to compare results more easily. Thus, the used sieve sizes were 9.5 mm, 6.3 mm, 3.3 mm, 1.7 mm, and 0.63 mm.

The sample was placed inside of the top size sieve and the sieve set (the other sieve sizes being below) is put in the Ro-tap sieve shaker. The sieving time can influence the outcome, and in this test, the time was set to be 5 minutes due to relatively small sample amount and the coarse nature of the samples. After the time is finished, the sieves were lifted out and one by one, each sieve was overturned on the piece of paper and brushed to remove all particles from the sieve. After each overturn, the material was weighted and the mass written down. The total mass of the sample as well as the mass of each fraction was later used for crushing curve figures (see chapter 4). Next, each sieve fraction was pulverized using a planetary ball mill (Pulverisette 5) with iron ball media. The rotation speed was set to 200 rpm and the milling time to 3 minutes. After pulverization, all samples were prepared and sent for external lithium analysis using ICP.

In order to get an idea of what minerals could be present in the samples, the common procedure is to measure them by XRD. However, in this research a comprehensive XRD study of all samples weas not possible due to the low sample amount (less than 10 g are needed for XRD) and limited budget. One way to confirm if the estimation of minerals are plausible is the overall particle density. For example, if a particle falls into a density range of 2.85 – 3.0 g/cm^3, meaning the particle needs to have an overall density within these limits. So for instance, if particle has an overall density of 2.92 g/cm^3, it cannot be 100% spodumene and thus is not fully liberated either. The overall density can be calculated using the density data of each mineral (Ralph et al., 2025) and equation 3.7 as follows:

$$Overall\ density = \frac{\sum(\rho_{mineral} \cdot m\%_{mineral})}{\sum m\%_{sample}} \tag{3.7}$$

The idea of performing an HLS test on the fine particles was raised during the project. The typical issue with HLS is that if the particle size is too fine, for example -630µm, the separation is not possible, or it is extremely slow. Also, the surface tension increases with the finer material. This is also part of the reason why fine fractions are typically screened and removed before DMS processes to be sent to a flotation circuit or discarded (see Chapter 2.3). However, the use of centrifugation in order to separate spodumene from gangue in the finer particles was tested as a possible solution.

The centrifugation is a very simple procedure. A 50 ml test tube was filled with fresh LST HL (ρ = 2.85 g/cm^3) followed by the fine material. The test tube was placed in a centrifuge and the settings

were adjusted (4000 rpm and 3 minutes). Only one density was selected, as the purpose was to assess whether extra fine particles (-630µm) could be separated effectively. Traditional beaker-scale HLS testing was not successful, as the settling time required for fine particles was much longer than the 10 minutes typically used for HLS tests with coarser fractions. After centrifugation, the sink and float fractions were collected and washed with water to remove any remaining heavy liquid. The entire sample was then dried. Both fractions were examined under an optical microscope to visually assess the separation performance.

3.4 MACHINE LEARNING

The other part of this study involves the use of machine learning for mineral grain identification and size estimation. This part of the work was conducted using a MacBook Pro (14-inch, 2021) equipped with an Apple M1 Pro chip and 16 GB of memory, running macOS Sonoma 14.7.4 and MATLAB (Version 24.2.0.2863752, R2024b). MATLAB was chosen as the coding language due to the author's valid license and previous experience with the software. In addition, standard toolboxes for image processing and machine learning were used, including the Computer Vision Toolbox (Version 24.2, R2024b), Deep Learning Toolbox (Version 24.2, R2024b), Statistics and Machine Learning Toolbox (Version 24.2, R2024b), and Image Processing Toolbox (Version 24.2, R2024b). An online AI tool, specifically a generative artificial intelligence chatbot (ChatGPT by OpenAI), was also utilized during the coding process. It was used to support the development by providing code structure suggestions, explaining specific programming functions, and assisting in troubleshooting when encountering errors in MATLAB.

The MATLAB code is more than 1500 lines long, consisting of 13 different steps. The code is available in GitHub (*https://github.com/LaitinenTeme/Drill-core-image-analysis-tool*). These 13 steps can be divided roughly into 3 groups: 1) image processing, 2) machine learning and classification, and 3) mineral grain segmentation and grain size estimation. Human intervention is only required during the initial image processing phase. Each of these steps is built for different purposes and they collectively form a comprehensive workflow for analyzing drill core images.

3.4.1 Image processing

The beginning of the code (steps 1–5) covers the method of image processing. The objectives of these steps are, firstly, to prepare the raw test images for further analysis, and secondly, to segment these images into smaller units called superpixels, which are later used for classification and grain reconstruction. In this context, training images refer to those images that are manually labeled by a human expert and used to train the classification models, while test images are unseen images that are used to evaluate the performance of the trained models.

Step 1 involves loading and selecting the test images that are to be analyzed. The user is asked to choose either all available images or a subset of them from a specified folder. These selected images will form the basis for all subsequent processing and analysis. The filenames and paths of the selected images are stored in a specific variable for later use in steps such as segmentation and classification. This step ensures that only relevant and correctly formatted input images are accepted for further processes.

In **step 2**, the raw training and test images are loaded and preprocessed to improve the quality of the image and make them suitable for segmentation and further analysis. The key parts of this step include noise reduction, contrast enhancement, and improving the image's resolution. These operations are executed through a sequence of image processing functions, including filtering, sharpening, and the use of a pre-trained VDSR (Very Deep Super-Resolution) neural network (MATLAB's Deep Learning Toolbox). The image quality plays an important role in image processing and thus many different techniques are used to make the image quality as high as possible. For example, uneven lighting can make it hard to distinguish minerals like spodumene and quartz, which look similar in color.

After the enhancement, each image is segmented into a set of superpixels using the SLIC (Simple Linear Iterative Clustering) algorithm (Achanta et al., 2010). The SLIC algorithm works by clustering together neighboring pixels that share similar color (typically RGB values) and spatial proximity, forming compact and visually coherent regions known as superpixels, which reduce the complexity of the image and makes it easier to classify and study individual mineral grains in the image. This segmentation is set to use 750 superpixels for large images and 300 for smaller images, respectively. These numbers define the approximate number of superpixels the image will be

divided into, depending on its size. Based on visual assessment of the results, a compactness value of 20 was used, which controls the shape of the superpixels. A higher compactness results in more square-like superpixels, while a lower value allows them to better follow the natural edges and structures in the image. However, using very low compactness values (e.g., 1) can significantly increase the computational time and lead to irregular superpixel shapes, which may not always be desirable. Therefore, a value of 20 was chosen as a balance between shape adaptability and processing efficiency. As a result of this step, a set of data structures containing the segmented superpixel labels, boundary images, and binary masks for each input image is created, which are then used in further steps.

In **step 3**, a visual representation of the superpixel segmentation is created for a single core sample image. The resulting superpixel boundaries are overlaid on the original image to show how the segments align with geological features. This visualization allows the user to inspect whether the number of superpixels and the compactness setting are appropriate, and to validate that the segments correspond to meaningful structures within the image. Figure 3.7 illustrates the outcome of step 3.

Figure 3.7 A visual representation of superpixel segmentation carried out in step 3.

In **step 4**, the training and test images are processed into individual groups of superpixels and saved as separate image files for future use. Each image is segmented using the same SLIC superpixel algorithm as in step 2, and the resulting superpixels are saved individually into dedicated folders. In addition to the image files, metadata such as the label matrix, boundary map, and centroid coordinates of each superpixel are saved for later use in the grain merging step. Each superpixel is extracted as a cropped image patch with the background masked out, allowing for cleaner training data and better visualization. The purpose of this step is to produce the actual data instances that will be used in the classification phase and to prepare coordinate information that will support later spatial operations such as grain merging.

In **step 5**, visual features are extracted from the previously segmented superpixel images. These features include color statistics (mean and variance of RGB channels) and basic texture descriptors (mean intensity and standard deviation of grayscale values). The training images are manually classified using a classification tool (presented later with details) into four predefined categories: spodumene, gangue, marker, and undetermined. Spodumene and gangue represent the primary mineralogical components of interest. Marker includes traces of grease pencil markings made by geologists, while Undetermined covers shadows or unclear pixels that cannot be confidently classified.

For each training superpixel, the corresponding label is assigned using the folder structure. The user is prompted to choose whether to use manually labeled or machine-generated test data. If manually labeled test data is used, the corresponding class labels are available and included. If the machine-generated superpixels are used instead, the test data remains unlabeled and is only used for prediction. All feature vectors are normalized to ensure consistent scaling, which is important for most classification algorithms. As a result of this step, two datasets are produced: a labeled training set and a test set, both consisting of extracted and normalized feature vectors ready to be used in model training and evaluation in the next steps.

The classification tool, mentioned earlier, is an interactive system separate from the main code, designed to label superpixels in drill core images. It forms a crucial part of the training data preparation workflow, enabling human experts, such as geologists, to assign correct mineralogical classes to segmented superpixels. Figure 3.8 presents the outcome after the classification where superpixels are placed into different classes (spodumene, gangue, marker and undetermined).

Figure 3.8 Result of classification. Superpixels from classes spodumene, gangue, marker and undetermined.

The primary advantage of the classification tool approach is that images can be used directly without requiring preliminary manipulation, such as cropping or other preprocessing methods. Additionally, it allows the use of already existing drill core imagery, eliminating the need for extra work by geologists, such as scanning sawed or polished core or creating ideal photographic conditions. In contrast to earlier studies that rely on such idealized imaging (e.g., Guiral, 2018; Koch et al., 2019.), the method used in this study enables direct analysis from existing drill core box photos, offering a practical and cost-effective approach readily applicable in industry. This tool is used as follows: original drill core images (Figure 2.5), showing both the cores and their wooden boxes, are introduced into the system. Relevant regions containing drill cores are interactively selected by the user through a graphical user interface implemented in MATLAB (see Figure 3.9). After choosing between training and test datasets, the user selects an image file for analysis. The selected drill core image is then displayed, and the user draws rectangular regions of interest (ROIs) directly onto the image by clicking and dragging. Each ROI corresponds to an individual drill core segment, which is processed separately.

While this manual selection approach offers flexibility, such as focusing on specific depth intervals, it is acknowledged that the process can be time-consuming when all core boxes are of interest. Although automated detection of drill cores could be implemented to reduce user input, this functionality was not developed in this study, as the focus was on validating the overall workflow.

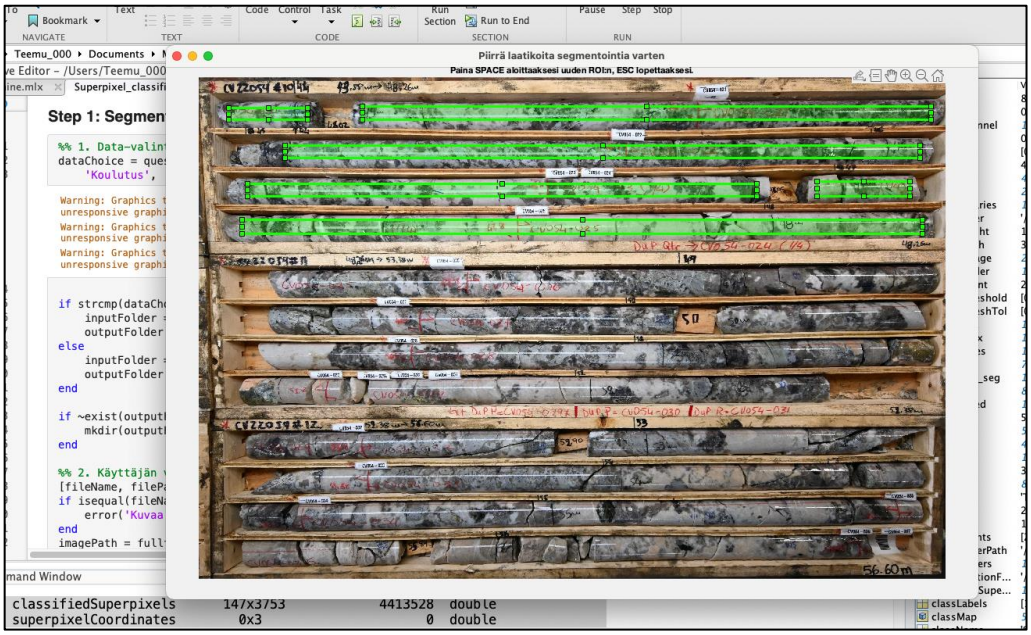

Figure 3.9 Graphical user interface where ROIs can be selected indicating the actual drill cores.

After drawing each rectangle, the user confirms the selection by pressing the SPACE key, enabling the definition of multiple ROI per image. The drawing procedure continues until all relevant drill core regions have been marked, at which point the user finalizes the selection process by pressing the ESC key. These user-defined rectangles serve as initial bounding boxes for subsequent processing, which includes mask refinement and segmentation. Figure 3.10 shows a drill core region and selected ROI. However, the rectangular selection typically does not cover the entire drill core segment accurately, because the cores in the images are often not perfectly horizontal, making precise rectangle drawing challenging. Additionally, ROI selection is subjective and depends on the user's precision. Therefore, each ROI undergoes iterative expansion guided by color-based thresholding criteria to accurately delineate drill core segments from background elements, such as wooden core boxes or dark void areas. After, these pre-segmented drill core images are saved either in a training images or test images folder depending on the type of image. It is worth mentioning that this core detection and segmentation can be done automatically using a wide spectrum of segmentation algorithms or classification models (Kirillov et al., 2023), but in this research, the main focus was not on creating the best possible segmentation code. Therefore, this simpler and less coding required approach was selected.

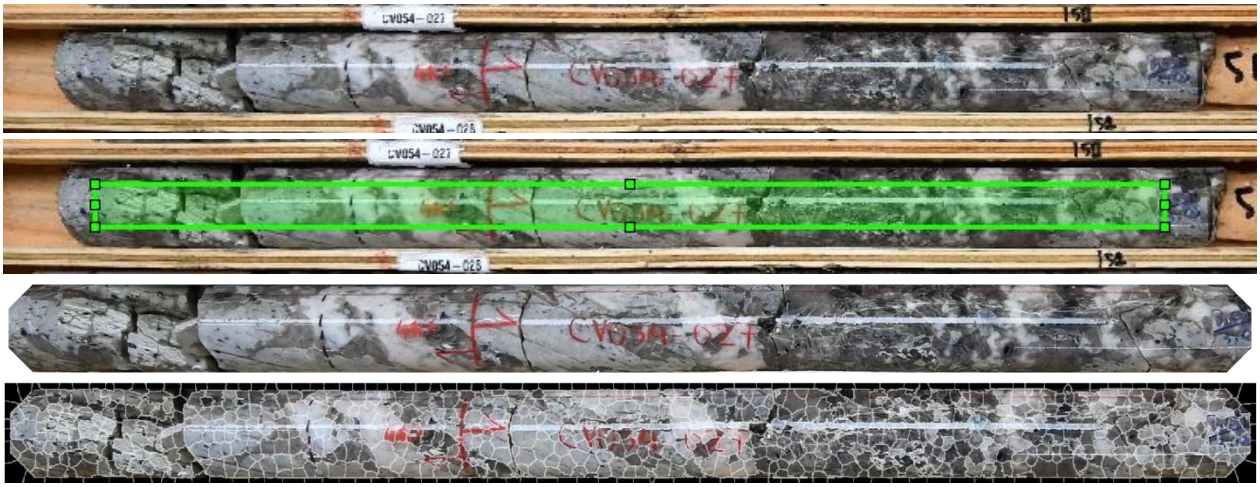

Figure 3.10 An example of the iterative segmentation method enabling more accureate drill core segmentation.

The classification process continues, and the user is prompted to choose whether to classify training or test images. Each image is first preprocessed using noise reduction, contrast enhancement, and resolution upscale using a pre-trained VDSR network (see step 2 above), after which the image is segmented into a number of superpixels using the SLIC algorithm, similar to step 2. The actual number of superpixels may vary depending on the size and resolution of each input image. Once segmentation is complete, the tool enters an interactive labeling mode (see Figure 3.11). Superpixel boundaries are overlaid on the original image, and the user can click on superpixels to select them and assign them to a class by pressing the space bar and entering a numeric category (1–4) representing the predefined mineral classes: spodumene, gangue, marker, and undetermined.

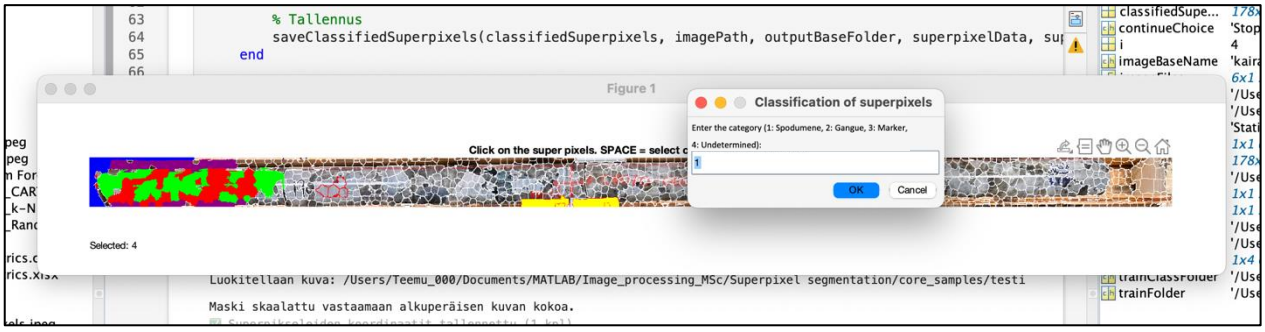

Figure 3.11 Classification tool for superpixel manual labelling.

The selected superpixels are colored according to their class for visual confirmation (see Figure 3.11), and the user can repeat this process for all relevant segments in the image. After

classification, the tool extracts the pixel coordinates of each labeled superpixel, stores the segmented image crops in class-specific folders, and saves the corresponding metadata (class and centroid). This tool ensures that accurate labeled training data is available for supervised machine learning models and also supports validating model performance with manually classified test images.

3.4.2 Machine learning and classification

The second phase of the code (steps 6 - 9) is associated to machine learning classification of the superpixels. Here, the superpixels obtained from previous steps are fed to the machine as a training data set, and the machine tries to learn to sort them based on the features of each superpixel. Then, a new test data set is introduced, and the machine will classify these test superpixels based on what it has learned.

In **step 6**, the feature data extracted in the previous steps is post-processed and saved for later use in model training and evaluation. This step ensures that all training and testing features are normalized and stored in a standardized format. First, the code defines the save directories for both training and test features based on whether the test data is manually classified by user, or generated automatically by the machine. The code checks that the feature matrices and class labels from Step 5 are not empty. If either set is missing, the process stops and notifies the user of the missing data. The actual post-processing is performed in a helper function, which normalizes each feature value to a [0, 1] range. This normalization is essential for many machine learning algorithms to perform optimally, as it ensures that all features contribute equally regardless of their original scale.

In **step 7**, the classification models (k-NN, CART and Random Forest selected based on the work of Maitre et al. (2019)) are evaluated using cross-validation to assess their ability to distinguish between different mineral classes based on extracted superpixel features. Specifically, a 5-fold cross-validation approach is used, where the training data is divided into five equal subsets. In each iteration, four subsets (80%) are used for training and the remaining one subset (20%) is used for validation. This process is repeated five times so that each subset serves once as the validation set. This provides a robust estimate of each model's performance without requiring a separate holdout set. The mean classification accuracy and its standard deviation across all five iterations are calculated to assess the model's generalization capability and stability.

Step 8 focuses on loading and preparing the extracted features for machine learning. The goal is to collect all relevant data from training and test folders and convert each superpixel image into a fixed-length numerical vector. The training data is always manually labeled (using the classification tool) and organized into folders based on classes. The test data can come either from manual classification or machine-generated results, depending on the user's choice made in step 5. Based on this, the code selects the correct folder and loads the images.

In **step 9**, the previously extracted features are used to train the final versions of the machine learning models and to classify superpixel images from the test set. The training is performed using the feature vectors and their corresponding class labels obtained from the training data. Before training, class weights are calculated to balance the dataset in case some classes are underrepresented. Depending on the model type, the code checks whether weighted training is supported and adjusts accordingly. After training, each model is used to predict the class of every test superpixel. The predicted class labels are then stored and used to generate new segmented images where each superpixel is assigned to its predicted class. These classified superpixels are saved into model-specific folders, organized by predicted class, for further use. In a nutshell, this step applies the trained models to unseen data and turns numerical features into meaningful predictions, enabling further analysis and visualization of mineral compositions in drill core images.

3.4.3 Mineral grain segmentation and size estimation

The final phase (steps 10 – 13) of the workflow focuses on the spatial merging of classified superpixels into larger coherent structures referred to as mineral grains. In **step 10**, the previously classified superpixel images are grouped together based on their associated test image. Each superpixel is matched with its centroid coordinates, which were saved in earlier steps. For each test image, neighboring superpixels belonging to the same class are grouped together. As a result, merged grain regions are created that better represent actual mineral grains in the original geological sample. Each resulting grain is reconstructed as an image by combining the pixel regions of the contributing superpixels (Figure 3.12). These merged "supersuperpixels" allows further analysis and estimation of the size of the mineral grain.

Figure 3.12 Final outcome of superpixel merging.

In **step 11** the goal is to visualize and save overlay images that highlight specific mineral classes (e.g., spodumene) detected by the trained classification model across all test images. This step provides an intuitive verification, allowing the user to visually inspect the classification results and assess the model's accuracy and performance. Initially, the user defines a target mineral class of interest (such as spodumene or gangue) and selects directories containing the test images and their corresponding superpixel classification data. For each test image, the original image and its associated superpixel classification data (labels and cordinate information) are loaded. Using these predicted labels, a binary mask is generated that identifies all superpixels classified as belonging to the selected target class. This mask is then overlaid onto the original image, highlighted in red with adjustable transparency, to clearly visualize the spatial distribution and coverage of the identified mineralogical class within the drill core (

Figure 3.13). The resulting overlay images are displayed individually and saved in a dedicated visualization folder.

Figure 3.13 Overlay mask highlighting areas classified as spodumene (in red) and the corresponding extracted grains

Step 12 is built only for getting performance statistics of each model in order to get an understanding how well the prediction works. This step takes manually labelled test data and calculates the percentages of correctly classified superpixels out of all superpixels after the model

prediction. The idea here is that since the models are trained using the same training dataset, the performance of the models should remain the same irrespective of the test data used. So, by using labelled test data, the accuracy can be determined since the correct class of each superpixel is known. Then, the known test data can be replaced with unlabeled new test data (real core images segmented by the machine) and the code performs the classification as usual. Importantly, both labelled and unlabeled test data must be different from the training data in order to get reliable estimation of the performance. Performance results are presented in Chapter 4 with details.

The final part (**step 13**) of the code integrates all previous steps, providing a direct connection between the original drill core images and the actual mineral grain sizes. This step calculates the grain size from the classified superpixels, linking image analysis results to real-world geological characteristics. To achieve this, grain size is calculated using six different metrics, represented in Figure 3.14 which illustrates the key size and shape metrics used to characterize each grain. These include: (1) the equivalent area disc diameter (d_{eq}), defined as the diameter of a circle with the same area as the grain; (2) the maximum inscribed circle diameter (d_{ins}), representing the largest circle fully contained within the grain boundaries; and (3) the maximum Feret diameter (d_{Fmax}), which is the longest distance between any two points on the grain's outer boundary. In addition, (4) the minimum Feret diameter (d_{Fmin}) describes the shortest distance measured across the grain using parallel lines, while (5) the minimum circumscribed circle diameter (d_{cir}) is the diameter of the smallest circle that completely encloses the grain. The grain's overall shape is further approximated by (6) the short (s_{ell}) and (7) the long (l_{ell}) axes of the equivalent-moment ellipse, which represents an ellipse having the same distribution of mass as the grain. Finally, (8) the width (w_{rec}) and (9) the height (h_{rec}) of the minimum enclosing rectangle describes the smallest rectangle, aligned to the grain's orientation, that fully contains the grain. Each metric contributes unique information about grain dimensions and morphology (Back et al., 2025). Each metric provides information about grain dimensions and shape. Results, such as grain size and size distribution, for each classification model and each mineral class are summarized and saved into an Excel file for further analysis.

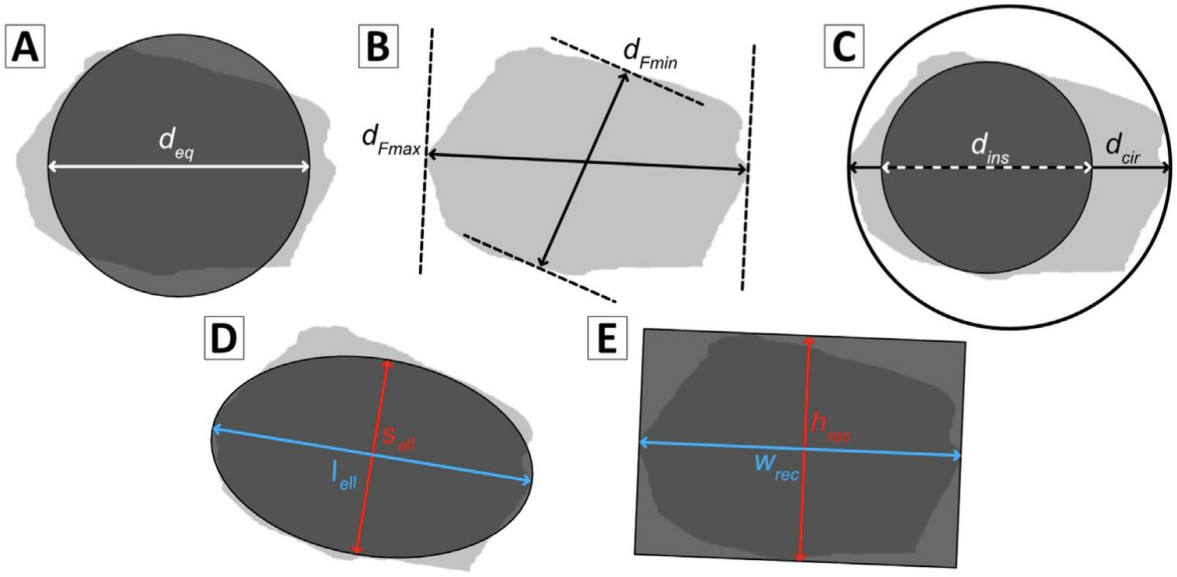

Figure 3.14 Grain size was measured using different methods, including: (A) equivalent area diameter, (B) minimum and maximum Feret diameters, (C) largest inscribed and smallest circumscribed circle diameters, (D) short and long axes of an ellipse, and (E) width and height of the smallest enclosing rectangle. Taken from Back et al. (2025).

An alternative approach would be to calculate the average grain size of all classified mineral grains, not just spodumene. While this was not done in the present study, the same method could be applied using existing data for other mineral classes. This would allow estimation of the overall grain size of the drill core, which could then be compared to HLS recovery to assess possible correlations.

CHAPTER 4 RESULTS AND DISCUSSION

In this chapter, the results of the analysis and experiments are presented, beginning with the outcome of the initial HLS recovery model, followed by a review of external HLS tests (PBM test work), the author's own HLS experiment, and finally the results of the machine learning algorithm and grain size estimation. The raw data of these results can be found to a large extent from appendices but can also be provided upon request by contacting the author or supervisor Prof. Marc Legault.

4.1 OVERALL RECOVERY PREDICTION MODEL

As presented in CHAPTER 3, the HLS test recovery prediction models were created based on logging data from the 11 drill cores of the composite samples and lithium recovery results by SGS (APPENDICES

APPENDIX A, Table A.1). Two types of models were developed: the first incorporated all available data, including visual assessments by geologists and technicians, mineralogical information by DRX, and chemical analyses. Some of this information is only available several weeks to months after drilling, meaning such models would be useful for long-term prediction of processing performance i.e. geometallurgy. The second type of data (Table A.2) relies solely on visual logging information, excluding the more time-consuming and costly laboratory analyses. This second type, while it may not be as accurate given the reduced amount of information it uses, has the advantage of using data which is available up to a few days after core is available, meaning it can be used to facilitate decision making during the exploration phase of a project.

After all variables had been averaged and standardized for each set of core sections making up the composite samples, the data was log-normalized minimize the effect of excessively large values. Here, "standardized" refers to adjusting the values (e.g., number of fractures, alteration intensity, etc.) relative to the total core length, making them comparable across samples of different lengths. The first interpretation of the dataset was carried out by creating a correlation matrix in Excel. A correlation matrix is not a comprehensive or definitive analytical tool, but it can provide a first impression and a general idea for model development. By examining the highest and lowest correlation values between HLS Li recovery to the sink fraction (%) and the different variables, a

preliminary selection of suitable input variables was made for the numerical model. Table 4.1 presents the variables which have the strongest correlation to HLS Li recovery based on correlation matrix. As seen from the table, spodumene grain size has the strongest correlation followed by the Li grade. This result is in agreement with the theoretical expectation that bigger grains, which are found in higher grade sections, should be more readily liberated and hence, provide higher recoveries (Wills & Finch, 2016a).

Table 4.1 Variables that show a strong linear correlation with HLS Li recovery based on the correlation matrix. Both positively and negatively correlated variables are listed, with data derived from logging records, ICP analyses, and other variables that show a strong relationship .

Correlation sign	Variable	Unit	Source	Correlation coefficient (R)
Positive	% Spd grains >7mm	%	Logging data	84.3 %
Positive	Li% in feed	%	ICP and WRA	66.2 %
Positive	Spodumene (wt %)	wt %	XRD	61.5 %
Positive	Ta content	ppm	ICP	48.2%
Negative	Spd grains <2mm	%	Logging data	-85.1 %
Negative	Spd grains 2-7 mm	%	Logging data	-80.1 %
Negative	Spd Inclusion Abundance	%	Logging data	-67.3 %
Negative	K content	%	ICP	-46.1 %

There are many approaches to creating an empirical model. In this study, the selected approach was the so-called step-by-step (also known as stepwise) method, where each parameter is tested and selected based on the response of the model after calibration. This way, the most significant variable can be identified and placed first in the equation, helping to reduce the total number of variables. The creation of the model is essentially a balance between achieving sufficient accuracy and limiting model complexity. Equation 4.1 illustrates the basic structure of the first-order empirical model:

$$Recovery = b_0 + b_1 \cdot x_1 + b_2 \cdot x_2 + b_3 \cdot x_3 \quad (4.1)$$

where b_i values are constants to be evaluated and x_i values represent the different variables from the drill core logging data. The three common ways to have a first impression of the model's performance are to minimize the squared error between the model and the actual Li recovery, and to compute the coefficient of determination (R^2), which should be as close to 1 as possible. In addition, a real statistical significance of each variable can be assessed using statistical indicators such as the p-value, which shows the likelihood of observing the given effect if the null hypothesis (H_0) is true. In general, when a term has a p-value below 0.05, it is considered statistically significant, with a low probability that the variable's influence is due to chance.

Although the first model performed very well thanks to the use of comprehensive data, including mineralogical and chemical analyses, such an approach may be less practical during early exploration stages, where rapid and cost-efficient assessments are preferred. The aim was to create a fast and simple prediction model based merely on visual assessment. In this respect, the second model, despite being less accurate, better serves the purpose of quickly and easily assessing overall drill core characteristics, such as spodumene grain size, abundance, and texture, and using these observations to predict the processability of the material.

The first stage of the modeling process involved identifying which variables contribute meaningfully to the accuracy of the model. Ultimately, it is necessary to determine the point at which including additional variables no longer significantly improves the model. Only statistically significant variables should be included in the final model (Montgomery, 2017), although some were added here for demonstration purposes. As shown in Table 4.2, after six variables, the R^2 value still increases, but only marginally compared to the initial rise seen with the first three variables, indicating that the effect of adding more than three variables is negligible. Thus, optimizing the model by including only the statistically significant variables plays an important role in this study.

Table 4.2 Performance of the two regression models as a function of added variables. Variables are added cumulatively in the order listed, and each row shows the model's performance after including one more variable. Satistically significant variables are shown in bold. Raw data available in Appendix A Tables A.1 and A.2.

Model 1 - All data				
Variable	p-value	Number of variables	Sum of squared error	R^2
% Spd grains >7mm	0.0001	1	2.45 %	71.78 %
Ni ppm	0.0025	2	1.83 %	78.84 %
W ppm	0.0043	3	0.78 %	90.99 %
Co ppm	0.0146	4	0.44 %	94.93 %
Th ppm	0.0673	5	0.21 %	97.57 %
Spodumene % (ICP)	0.20375	6	0.13 %	98.46 %
Model 2 - Logging data only				
Variable	p-value	Number of variables	Sum of squared error	R^2
% Spd grains >7mm	0.000994	1	2.45 %	71.78 %
Spd Alteration Intensity	0.39339	2	0.95 %	89.04 %
Average Natural Fractures	0.60511	3	0.49 %	94.30 %
Average Fracture Frequency	0.71695	4	0.47 %	94.58 %
Average ISRM Rock Strength	0.15942	5	0.42 %	95.15 %
Average RQD	0.79132	6	0.39 %	95.48 %

As a result of manual step-by-step variable selection, multiple variables were identified as statistically significant and retained in the final model. The most significant factor was the proportion of coarse spodumene grains (Spd > 7 mm), which showed the strongest positive correlation with lithium recovery, reflecting the importance of grain liberation in the HLS process. In addition, several geochemical variables, such as nickel (Ni), tungsten (W), and cobalt (Co) concentrations, also contributed significantly to the model. While their individual effects are smaller than that of grain size, they enhance the model's predictive power and help capture compositional variations in the samples. The whole equation 4.2 is represented as follows:

$$Li\ rec\ \% = -5.6 + 3.2 \cdot \log_{10}(Spd > 7mm) + 0.3 \cdot \log_{10}(Ni) - 0.3 \cdot \log_{10}(W) - 0.3 \cdot \log_{10}(Co) \quad 4.2$$

The sign of each constant in equation 4.1 indicates the direction of the dependency between each variable and lithium recovery. The proportion of spodumene grains larger than 7 mm (Spd > 7 mm) shows the strongest positive correlation with HLS Li recovery. Other variables included in the model, nickel (Ni), tungsten (W), and cobalt (Co), concentrations, also contributed statistically, although their relationship to lithium recovery in HLS testing remains dubious. In addition, the low amount of these elements (average < 0.8 ppm for Co, and < 10 ppm for Ni) suggests that these relationships are fortuitous. One reason for elements to be significant can be random coincidence since there was only a few data points (11 samples) and a large number (120) of variables.

These geochemical indicators may be caused by broader differences in the samples, but their effects are less intuitively linked to processability and thus require more test work. The fact that Li grade was not incorporated in the final model is explained by its strong co-dependency with grain size. As shown in Figure 4.13 grain size and grade are strongly correlated. Hence, adding one term to the model means that the other term can no longer improve the model significantly.

When statistical test and p-value was first applied to Model 2 using normalized data based on the core length, two variables stand out: the proportion of coarse spodumene grains (Spd > 7mm) and lithium grade (Li%) were both found to be statistically significant predictors (p-value < 0.05), consistent with Table 4.1. However, these two are so called codependent variables, meaning they are related to each other and thus they both cannot be included into the model, since they don't bring any more value as one of them will bring alone. Since the aim of this work is to identify low-cost, easily obtainable predictors, "Spd > 7mm" was chosen as it is based on visual assessment,

whereas lithium grade requires laboratory analysis and falls outside the scope of this project. After stepwise analysis, similar to Model 1, the only statistically significant variable is the spodumene grain size having p-value of 0.00099444 clearly stating the significance of the variable. Overall, equation 4.3 confirms that grain size is the most reliable and consistent visual indicator for predicting HLS Li recovery

$$Li\ rec\ \% = -4.5 + 2.96 \cdot \log_{10}(Spd\ > 7mm) \quad 4.3$$

Using the aforementioned models (Equations 4.1 and 4.2), their prediction performance was compared against the actual lithium recovery values, as illustrated in Figure 4.1. Overall, both models follow the actual recovery trends fairly well. Model 1, which consists of multiple variables including laboratory data, demonstrates much higher accuracy, with relative errors consistently below 5% in each sample, even for the most challenging samples, such as 1 and 10. This confirms the superior fit of Model 1, which is expected since all mineralogical and chemical data was used.

Model 2, which relies merely on the percentage of coarse spodumene grains (Spd > 7 mm), shows higher relative errors. Notably, in samples 6 and 8, the relative error exceeds 10%, which likely results from their much finer spodumene grain sizes, known to have a direct negative impact on HLS lithium recovery. Still, the average relative error across all 11 samples remains below 5%, indicating that even a single-variable model can yield a reasonable prediction when the selected feature is highly significant.

Interestingly, the same samples, in general, which show larger errors in Model 2 also present challenges in Model 1. This suggests that the discrepancies may not stem solely from the lack of laboratory data but potentially from inconsistencies in the visual grain size assessment itself. Since spodumene grain size is used in both models and is the most influential variable, any inaccuracy in its estimation, such as subjective variation between logging geologists, could affect the prediction accuracy. Additionally, a portion of the error might be attributed to uncertainties in HLS recovery measurements, which depend on accurate weight measurements and Li grade determinations.

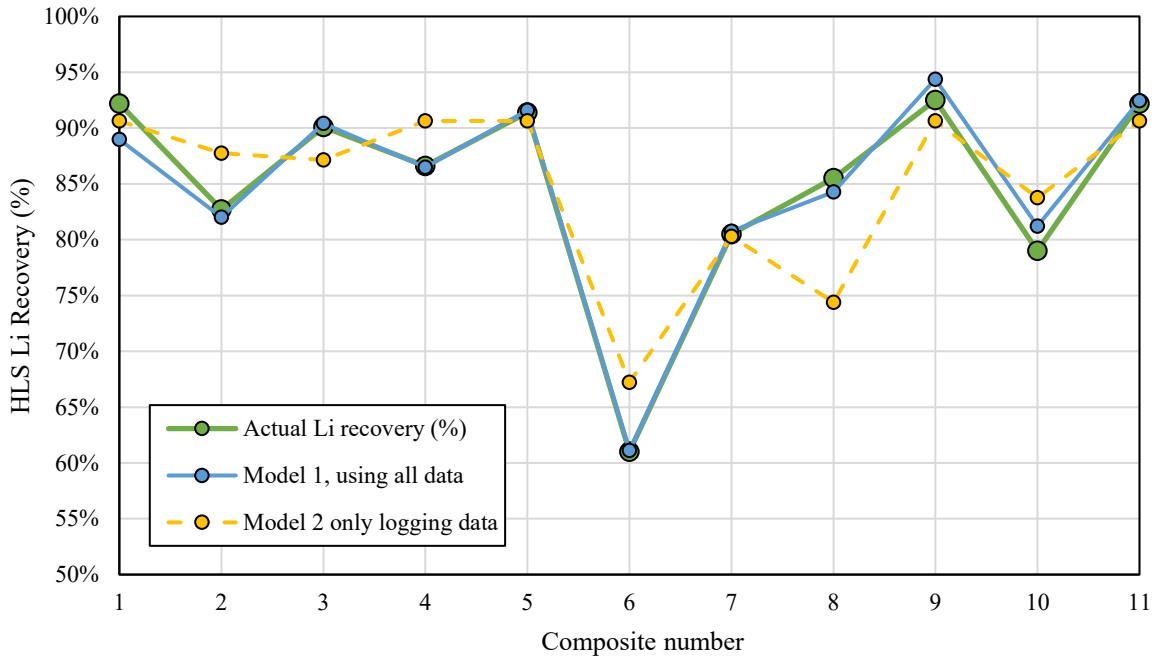

Figure 4.1 Difference between actual Li recovery and two different models using only statistically significant variables.

Figure 4.2 compares the predicted lithium recovery values of both models to the actual HLS Li recovery. Model 1 (eq. 4.1), which uses all available data including laboratory analyses, shows an excellent relationship ($R^2 = 0.976$), indicating high predictive accuracy. Model 2, based solely on the proportion of coarse spodumene grains (Spd > 7 mm), achieves a lower but still meaningful correlation ($R^2 = 0.718$). While less precise, Model 2 highlights the potential of using simple logging data for recovery prediction at the exploration stage.

Interestingly, when applying data from the PBM test work (three different samples: composite, LG and HG)[1], which come from a different location within the same CV5 deposit than the other 11 variability samples, the performance of these models can still be validated. As shown in Figure 4.2, red squares represent the validation points of model 1, whereas yellow triangles represent those of model 2. When including these data points, the R^2 value for model 1 is 81.42% and for model 2, 62.11%. Although these values are slightly lower than those reported earlier, they are still significantly high, indicating a strong correlation even when using data from a different part of the

[1] These three samples come from the Zeppelin testwork program (19005-02A) as mentioned in the NI 43-101 submitted to SEDAR+ by Patriot Battery Metals on August 28th 2025.

deposit. One note is that the second set of data appears to be consistently below the 1:1 line, indicating a slight but systematic oversestimation of the Li recovery when using the initial model. This may reflect slightly different liberation and HLS behaviour from this group of samples. Overall however, these results tend to validate that the variables used in each model remain significant for predicting HLS test recovery.

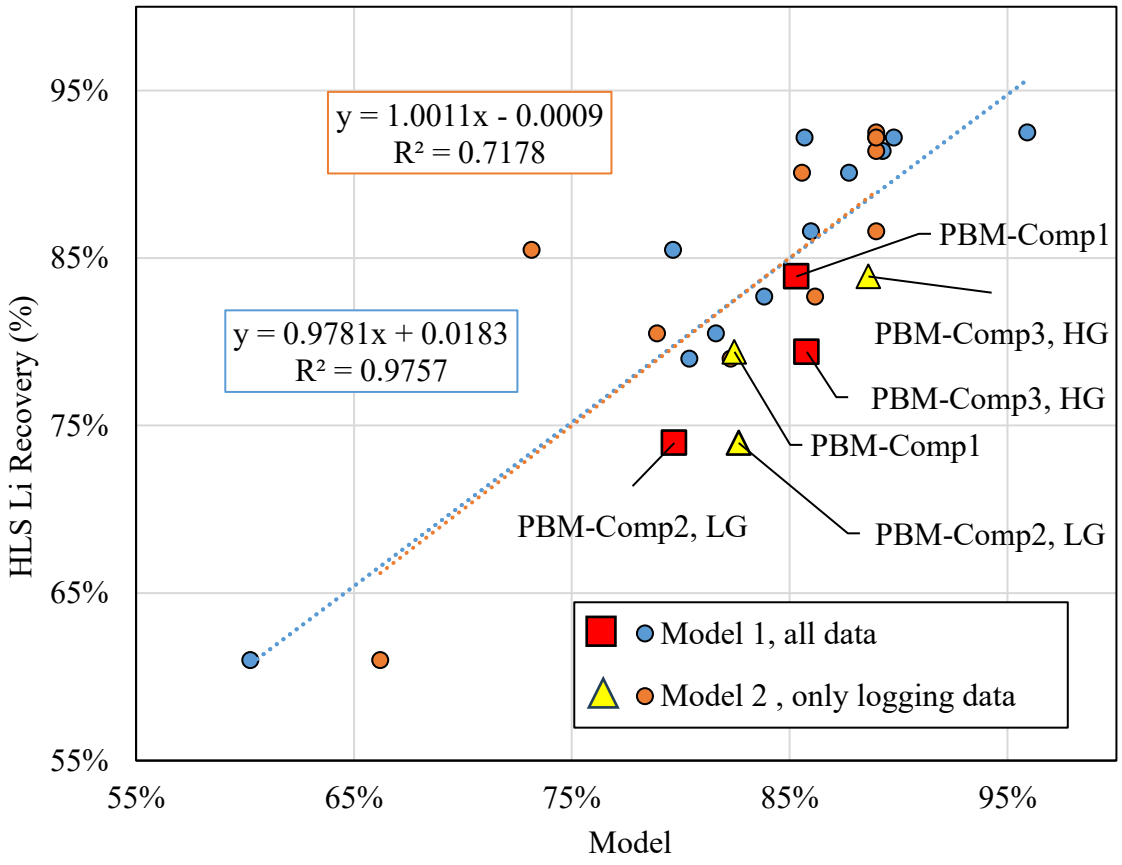

Figure 4.2 Correlation between model predictions (using only significant variables) and the actual HLS Li recovery (%). Blue and orange circles represent the individual data points used to build Model 1 (all data) and Model 2 (only logging data), respectively. Yellow triangles and red squares indicate independent validation points from PBM test work.

4.2 RESULTS OF EXTERNAL SIZE-BY-SIZE HLS TEST WORK

A total of 16 composite samples of variable grades were submitted by Patriot Battery Metals to SGS Lakefield in 2022 for an HLS test program, called Patriot Battery Metals (PBM) test work, aimed at evaluating how geological variation within the deposit affects metallurgical performance. The test program included sample preparation, mineralogical analysis, HLS testing, and dry magnetic separation. Its main goal was to provide a preliminary understanding of the lithium beneficiation variability of samples collected from the CV5 Pegmatite at the Shaakichiuwaanaan Property (Aghamirian & Imeson, 2023). Table 4.3 illustrates size-by-size lithium distribution by S.G. obtained from these HLS tests. As an example, the last column of the first row in Table 4.3 indicates that, for PBM-Comp001 at particle size 0.6 to 1.7 mm and using a HL at S.G. of 3.0 g/cm³, 78.2% of the lithium content is recovered in the sink fraction. Moving left from the last column, the same principle applies for each size fraction and for each sample. Lastly, 1.35% of the lithium content ended up in the float fraction while using HL at an S.G. of 2.65 g/cm³. Table 4.3 shows samples PBM-Comp001 to PBM-Comp003, where PBM-Comp001 is a composite sample made from both low- and high-grade material, and PBM-Comp002 and PBM-Comp003 represent low-grade and high-grade samples, respectively.

Initial spodumene grain sizes of these three samples were evaluated from the drill cores by geologists at PBM using the aforementioned classification system (see section 3.1). The table also presents the average proportion of spodumene grains falling into each size category (<2 mm, 2–7 mm, >7 mm), as visually estimated from drill core inspection. It can be observed that a greater proportion of the high-grade material consists of coarse spodumene grains larger than 7 mm, while the low-grade material has a more balanced distribution, with a notable portion also falling into the 2–7 mm range. The composite sample lies between these two. This trend supports the general correlation that higher-grade material tends to contain coarser spodumene grains, showing the connection between grade and grain size.

Table 4.3 Lithium distribution by SG for composite, low-grade, and high-grade samples. The table also includes the estimated average proportions (%) of spodumene grains falling into each size category (<2, 2–7, >7 mm), as visually assessed by PBM geologists from drill core samples.

	Test work ID	Top Size (mm)	Bottom Size (mm)	Spodumene distribution by grain size			Recovery to each S.G. cut point							
				<2mm	2-7mm	>7mm	2.6	2.65	2.7	2.8	2.85	2.9	2.95	3
Composite	PBM-Comp001	1.7	0.6	0.70	5.01	94.16	1.35 %	0.72 %	2.29 %	2.79 %	3.24 %	2.29 %	8.50 %	78.82 %
	PBM-Comp001	3.3	1.7				1.63 %	1.30 %	3.94 %	2.84 %	3.27 %	3.60 %	11.90 %	71.51 %
	PBM-Comp001	6.3	3.3				2.27 %	1.77 %	5.80 %	4.30 %	6.11 %	5.55 %	16.14 %	58.06 %
	PBM-Comp001	9.5	6.3				1.12 %	2.27 %	7.06 %	5.54 %	5.33 %	6.30 %	18.49 %	53.90 %
Low-grade	PBM-Comp002	1.7	0.6	1.40	9.68	88.64	2.58 %	1.64 %	6.91 %	3.03 %	2.47 %	3.06 %	8.04 %	72.26 %
	PBM-Comp002	3.3	1.7				4.02 %	3.61 %	5.38 %	4.64 %	6.05 %	5.75 %	10.28 %	60.26 %
	PBM-Comp002	6.3	3.3				5.74 %	5.95 %	9.82 %	7.09 %	8.24 %	9.56 %	11.23 %	42.37 %
	PBM-Comp002	9.5	6.3				4.76 %	7.61 %	12.05 %	10.37 %	8.70 %	9.48 %	11.43 %	35.61 %
High-grade	PBM-Comp003	1.7	0.6	0.00	0.09	99.91	0.90 %	0.93 %	2.41 %	2.21 %	1.41 %	2.30 %	6.29 %	83.55 %
	PBM-Comp003	3.3	1.7				1.09 %	1.62 %	3.97 %	2.70 %	1.89 %	3.73 %	8.27 %	76.73 %
	PBM-Comp003	6.3	3.3				1.11 %	2.27 %	6.08 %	3.62 %	3.68 %	4.41 %	9.77 %	69.06 %
	PBM-Comp003	9.5	6.3				1.65 %	2.81 %	6.17 %	4.38 %	5.20 %	6.04 %	10.57 %	63.19 %

Careful consideration of the data in Table 4.3 shows that as the particle size class increases, the percentage of lithium in the sink fraction at an HL of 3.0 g/cm³ tends to decrease. This is an expected observation since the liberation of lithium is likely to be improved for smaller particles, and thus more lithium particles should be recovered in the sink fraction. Figure 2.11, presented earlier, illustrates this phenomenon. Thus, the lithium distribution shows that when using a HL at a density of 3.0 g/cm³, most of the lithium ends up in the sink fraction, although the percentage of lithium in this sink fraction decreases as particle size increases. Figure 4.3 clearly shows the decreasing recovery trend on each sample when the particle size is increasing.

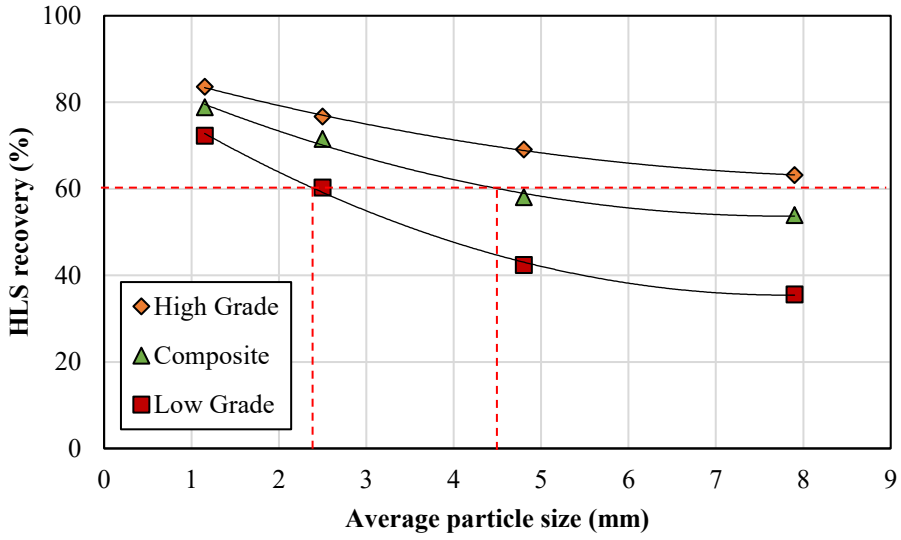

Figure 4.3 The effect of grain size on HLS recovery. X-axis refers to average particle size since samples were sieved into 4 size classes. PBM-Comp001 is a composite sample (green) made from both low (red)- and high-grade (orange) material, and PBM-Comp002 and PBM-Comp003 represent low-grade and high-grade samples, respectively.

As an example, Figure 4.3 also shows that high-grade sample processing results in 83% of the lithium reporting to the sink fraction at HL of 3.0 g/cm³, while low-grade samples result only in 72%, an 11% decrease. As samples are compared for the same particle size fractions, one can infer that the higher grade sample is associated to the coarser spodumene grains which are easier to liberate. This is also in agreement with the physical reality of liberation in the literature (Wills & Finch, 2016).

Thus, it appears likely that the particle size required to achieve optimal recovery without over crushing the sample can be different for high- and low-grade materials. This can be reworded the following way: higher-grade material requires less crushing while low-grade samples need to be crushed finer in order to achieve the same lithium recovery in the sink fraction. This important observation not only warrants the use of caution when picking a crushing size but could even go against the usual practice of blending low- and high-grade materials, which is conducted in an effort to stabilize feed grades. Rather, processing these materials separately and using different crusher settings may lead to improved recoveries through reductions in over and under crushing.

Furthermore, as stated before, high-grade material typically contains larger spodumene grains, which can already be identified at the core logging stage through visual inspection or even image analysis based on RGB-images. This provides an early indication of how much crushing may be needed. However, estimating liberation at such coarse sizes presents challenges, as techniques like SEM-based automated mineralogy only assess small surfaces at a time, making it difficult to obtain a statistically significant number of grains. An alternative method worth considering is micro-XRF, which can analyse much larger surfaces (up to 10 cm × 10 cm) on certain instruments if a large polished section is prepared. Additionally, Al/Si ratios can be used to distinguish spodumene from other silicates that contain Na or K. This can result in either over- or underestimating liberation depending on the sample subset analyzed. Therefore, complementary laboratory HLS testing is crucial to provide a more comprehensive understanding of spodumene liberation and the extent of attached gangue minerals across different density fractions. Such data would help evaluate how different crushing strategies influence liberation and recovery, help with decisions on optimal crusher settings, and support the development of material separation strategies. This further highlights why it is important to combine core logging, image analysis, and laboratory testing, as done in this study.

4.3 LABORATORY TEST WORK RESULTS

The laboratory test work in this study included sample preparation and HLS testing, as described in Chapter 3. The purpose of this testing was to better understand spodumene liberation and evaluate the crushability of spodumene relative to quartz and other gangue minerals. Additionally, the tests aimed to identify how lithium is distributed across different size fractions after crushing. This section presents the results of the crushing tests as well as the initial HLS outcomes conducted in the laboratory.

4.3.1 Crushing

As explained earlier (3.3.1), the four sample groups (Table 3.3) studied are: 1) liberated spodumene (LS) with nearly 100% spodumene content, 2) liberated quartz (LQ) with low spodumene content, 3) mixed spodumene (MS) containing a dominant (visually ≈75%) portion of spodumene and 4) mixed quartz (MQ) containing a dominant (visually ≈75%) portion of quartz. These samples were manually sorted from the PBM-comp003 material, (99.67% of the grains >7mm) based on visual mineral estimate. The samples were all first crushed to a top size of 9.5 mm (see Figure 3.5) to prepare them for HLS testing. Prior to HLS, sieve analysis was performed on each sample to assess breakage behavior through particle size distribution.

Figure 4.4 provides valuable information about how different samples respond to the crushing process. For the same crusher setting resulting in 100% passing 9.5mm, liberated spodumene sample, represented by purple squares, shows the lowest percentage passing at all size ranges, meaning it remains coarser compared to the other samples. This indicates that samples rich in spodumene may be more resistant to crushing or, at least, produce relatively coarser fragments compared to other minerals (Cunningham, 2025). Comparatively, liberated quartz, marked by green triangles, has a slightly higher percentage passing than liberated spodumene, meaning it breaks more easily or is already smaller in the beginning before crushing.

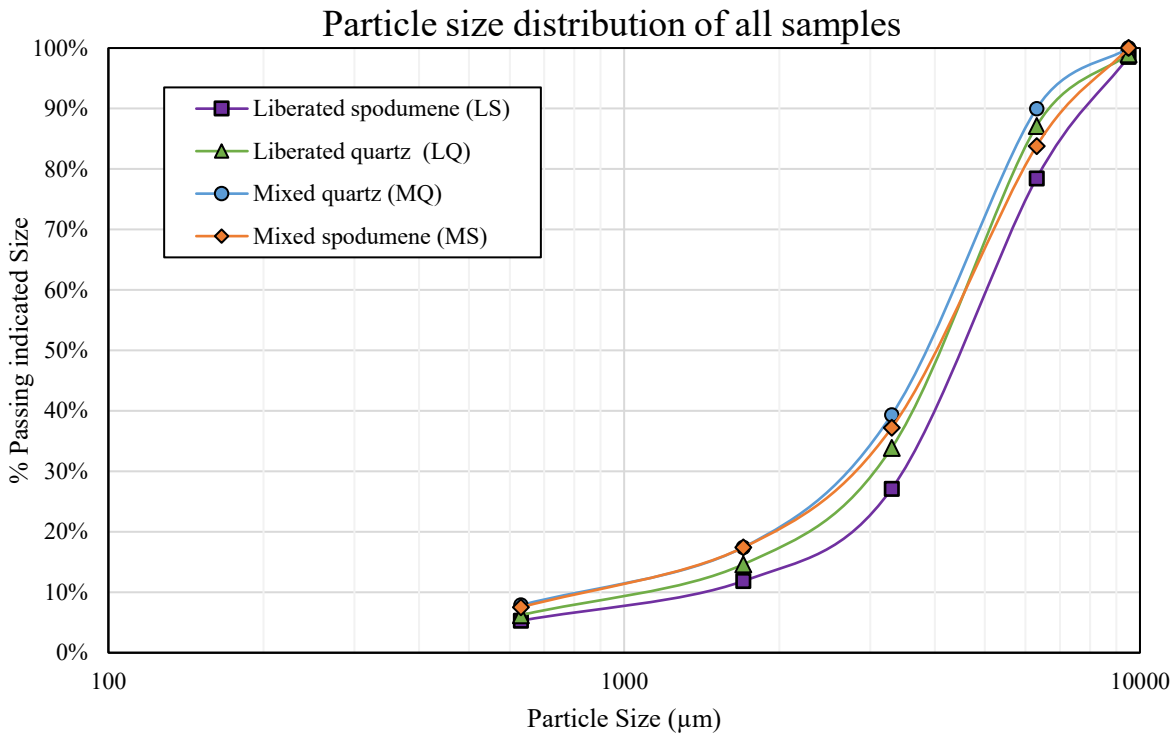

Figure 4.4 Particle size distribution of all samples.

The mixture containing dominant quartz grains (MQ), represented by blue circles, shows the highest percentage passing at all size fractions, meaning it is the most fragmented material after crushing. The presence of large quartz grains might have influenced fracture patterns, allowing easier breakage. Meanwhile, the mixture containing dominant spodumene grains (MS), shown by orange diamonds, follows a distribution similar to the MQ mixture but remains slightly coarser. This suggests that spodumene's presence in the mixture may contribute to a higher resistance to breakage compared to mixed quartz sample.

The fact that the liberated spodumene (LS) showed the coarsest particles after crushing may seem surprising since spodumene is actually "softer", with a lower Bond Work Index (BWI) than quartz (11.3 vs. 22.3 kWh/t) (Kohitlhetse et al., 2023; Mama, 2023), This is consistent with the Mohs hardness scale, which indicates that quartz is slightly harder than spodumene. The liberated spodumene sample formed coarser particles with fewer fines compared to liberated quartz. This difference is not explained by hardness alone, as spodumene and quartz have similar Mohs hardness (6.5–7), but rather by cleavage: spodumene tends to break along cleavage planes, producing longer fragments that may slide through the crusher if oriented favorably. These particles

would, however, not necessarily be screened down as easily. Quartz, on the other hand, is more brittle and lacks cleavage, so it may shatter into more regular particles (Acke et al., 2023). This highlights that factors beyond hardness, such as cleavages but also alteration and inclusion%, may play a significant role in the breakage behavior of these minerals.

The resulting size distributions were modelled using G-G-S and R-R modes as described in chapter 3. Both models were developed by adjusting the parameters to minimize the sum of least-squares between the original measured data (cumulative passing percentages) and the modeled data. The model performances are shown in Figure 4.5 for LS, LQ, MS and MQ. Overall, the Gates-Gaudin-Schuhmann model provided a slightly better fit across all sample types, particularly for LS, as indicated by the higher R^2 values.

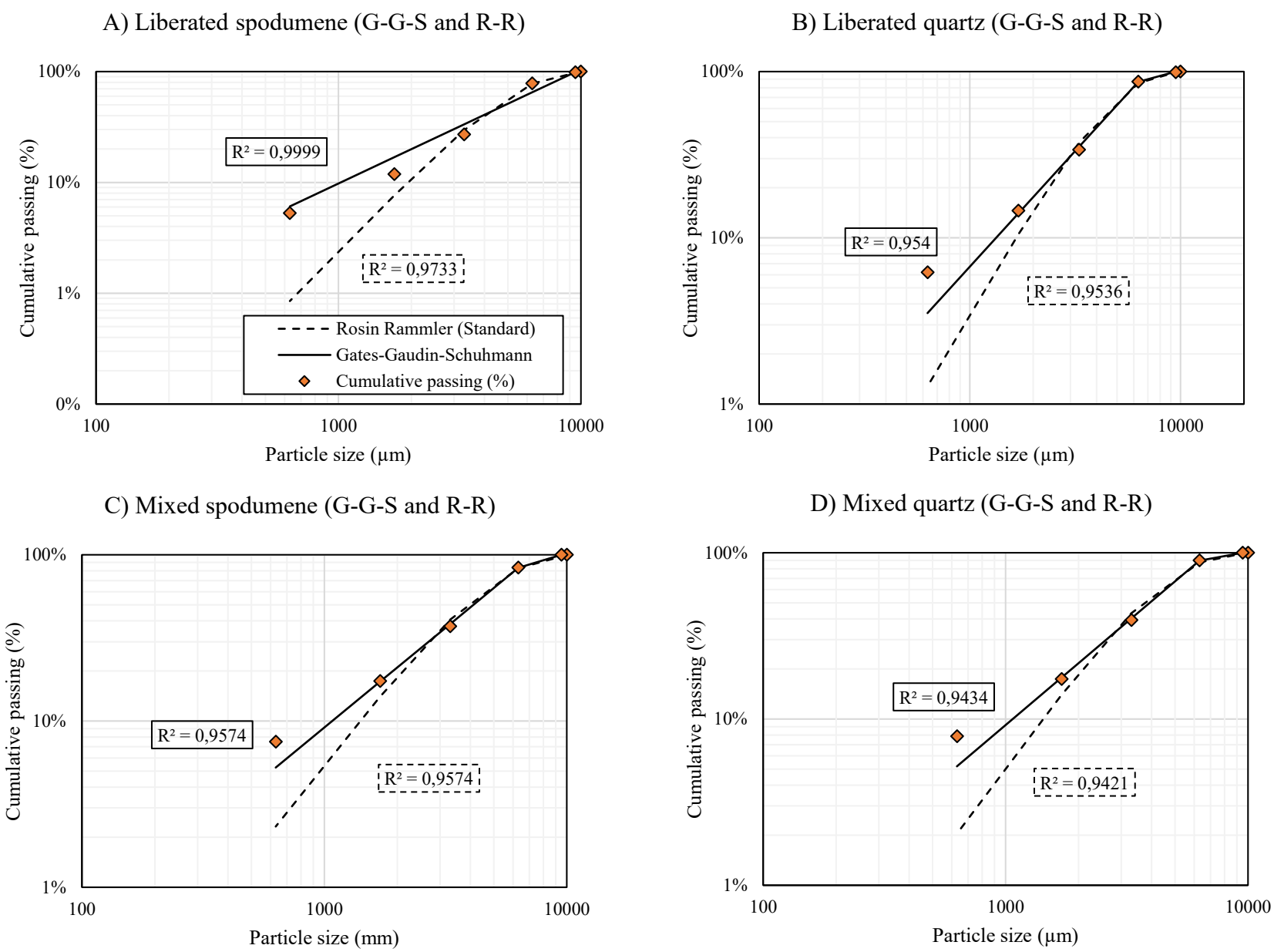

Figure 4.5 Modelling crushability (orange diamonds) of liberated spodumene (A), liberated quartz (B), mixed spodumene (C) and mixed quartz (D) samples by using GGS (black line) and RRS (dotted line) methods.

While the basic GGS model relies on a maximum particle size, in this study, a modified approach was used to improve model accuracy, applying a cap above which the cumulative passing value is 100%. This modification ensures that the calculated cumulative passing percentage does not exceed 100%. While this approach provides a more accurate fit, it introduces certain limitations in interpreting model parameters. For instance, when using the Solver in Excel to minimize the sum of squared errors between the GGS model and the original data points, the model suggests an optimal K value of 7 407.58 µm, despite the actual top size being 10 000 µm. However, using the original equation at the same particle resulted in unrealistic values exceeding 158% cumulative passing. This discrepancy highlights a trade-off where the modified GGS approach improves fitting accuracy but compromises the physical meaning of the parameter.

The RRS model employs logarithmic transformations to fit particle size distributions. While widely used for general assessments, it has known limitations, particularly in predicting fine fractions, as mentioned by Wills & Finch (2016). Consequently, although the RRS model performs reasonably well for coarser fractions, its accuracy is highly reduced for finer grain sizes.

The size distribution parameters of the four samples analyzed using the Gates-Gaudin-Schuhmann (GGS) and Rosin-Rammler-Sperling (RRS) models are summarized in Table 4.4. The models' parameters quantify the differences in particle size distribution. Parameters α and n illustrate the width of the distribution meaning the spread of particle size. High values indicate narrower distributions and fewer fine particles produced, whereas low values mean wider distribution and more fine particles. The K-value (GGS), on the other hand, stands for the top size, meaning the higher the value, the coarser the material. Finally, the X_0 indicates the particle size at which 63.2% of the material passes through the sieve. Again, higher X_0 values mean coarser material and vice versa. Table 4.4 represents these parameters on each sample.

Table 4.4 Parameters used in Gates-Gaudin-Schuhmann and Rosin-Rammler-Sperling models to present the crushing behavior of the ore.

	GGS		RRS	
	α	K	n	X_0
Liberated quartz	1.39	6980.05	2.17	4680.30
Liberated spodumene	1.53	7407.58	2.25	5242.77
Mixed quartz	1.24	6882.16	2.00	4378.04
Mixed spodumene	1.20	7327.76	1.88	4656.44

Interestingly, the mixed samples demonstrate lower α and n values, indicating broader size distributions with a higher proportion of fines. Among these, the sample with mixed spodumene grains (with small quartz inclusions) exhibits the lowest α and n values. The mixed quartz grains also show a broad distribution but retain slightly coarser particles compared to mixed spodumene. These findings imply that predicting the breakage behavior of mixed samples may be more complex than just considering the behavior of the minerals present but likely involves interaction between the species present. Among the tested models, the GGS model provided a notably better fit across all particle size ranges, especially for fine particles, making it more suitable for predicting fines generation.

Overall, while both models provide valuable insights, the GGS model outperforms the RRS model in representing the full particle size distribution of the spodumene sample. The primary purpose of applying these general models (GGS and RRS) was to validate the reliability of the experimental particle size data obtained in this study. By demonstrating that the generated data aligns well with well-established and commonly known models, it provides additional confidence in the quality and consistency of the breakage and size distribution results. This fit confirms that the breakage behavior of spodumene in this test work follows typical mineral processing trends, supporting the robustness of the experimental approach. Consequently, the use of these models serves as an

additional layer of verification that the findings are credible and applicable within the broader context of mineral processing research.

4.3.2 HLS Test Work

The traditional HLS tests (as explained in section 3.3.2), conducted using a beaker setup, produced three sink fractions (> 3.0, > 2.85 and > 2.7 g/cm^3) and one float fraction (< 2.7 g/cm^3) for each sample. These fractions were further sieved into five different particle size classes (9.5 - 6.3, 6.3 - 3.3, 3.3 - 1.7, 1.7 - 0.63 and <0.63 mm) with measured mass recoveries and calculated weight % for each size fraction. In addition, based on the ICP chemistry results of these tests, and more specifically the Li assays, the percentage of spodumene was calculated by simply dividing the Li% by 0.0373 (assuming the spodumene contains its theoretical value 3.37% of lithium and that all lithium is in spodumene). The percentage of non-spodumene minerals was then obtained by subtracting the calculated spodumene% from 100% representing the amount of non-spodumene material. All these values are presented in Table 4.5.

The spodumene distribution (%) was calculated to determine how the total recovered spodumene was distributed among the various HLS products. The calculation was based on the spodumene content (wt%) of each individual fraction, divided by the total recovered spodumene across all fractions in the HLS test. Similarly, the non-spodumene distribution was calculated using the percentage of non-spodumene instead of spodumene. Some of the samples did not have a minimal amount of mass, and thus ICP analyses were not possible, explaining why some samples have no spodumene values in Table 4.5.

Table 4.5 Outcome of HLS test work on liberated spodumene (LS), liberated quartz (LQ), mixed spodumene grains with a dominant spodumene component (MS) and mixed quartz grains with a dominant gangue component (MQ).

Tag	HL SG	Weight g	Weight %	Li %	Spd %	Non-spd %	Spd distribution %	Non-spd distribution %
LS Sink -9.5 +6.3mm	3.00	1.32	14.0	2.70	72.39	27.61	70.88	9.27
LS Sink -9.5 +6.3mm	2.85	0.78	8.3	1.10	29.49	70.51	28.88	23.67
LS Sink -9.5 +6.3mm	2.70	2.27	24.0					
LS Float -9.5 +6.3mm	-2.70	5.08	53.8	0.01	0.24	99.76	0.24	33.49
LS Feed -9.5 +6.3mm		**9.45**	**100.0**	**0.47**	**12.67**	**87.33**	**12.41**	**29.32**
LS Sink -6.3 +3.3mm	3.00	1.59	6.4	2.60	69.71	30.29	55.13	11.07
LS Sink -6.3 +3.3mm	2.85	4.02	16.3	1.50	40.21	59.8	31.81	21.85
LS Sink -6.3 +3.3mm	2.70	4.58	18.5	0.59	15.82	84.18	12.51	30.77
LS Float -6.3 +3.3mm	-2.70	14.54	58.8	0.03	0.70	99.30	0.55	36.30
LS Feed -6.3 +3.3mm		**24.73**	**100.0**	**0.54**	**14.36**	**85.64**	**11.36**	**31.31**
LS Sink -3.3 +1.7mm	3.00	0.59	8.3	2.30	61.66	38.34	60.32	12.87
LS Sink -3.3 +1.7mm	2.85	1.17	16.4	1.50	40.21	59.79	39.34	20.08
LS Sink -3.3 +1.7mm	2.70	1.31	18.4					
LS Float -3.3 +1.7mm	-2.70	4.05	56.9	0.01	0.35	99.65	0.34	33.47
LS Feed -3.3 +1.7mm		**7.12**	**100.0**	**0.44**	**12.67**	**87.33**	**12.39**	**29.33**
LS Sink -1.7 +0.63mm	3.00	0.3	12.2	2.10	56.30	43.70	98.96	12.74
LS Sink -1.7 +0.63mm	2.85	0.44	18.0					
LS Sink -1.7 +0.63mm	2.70	0.3	12.2					
LS Float -1.7 +0.63mm	-2.70	1.41	57.6	0.02	0.59	99.41	1.04	28.97
LS Feed -1.7 +0.63mm		**2.45**	**100.0**	**0.27**	**7.23**	**92.77**	**12.71**	**27.04**
Total LS Feed		**43.75**		**0.49**	**13.20**	**86.80**	**0.28**	**0.25**

Table 4.5 Outcome of HLS test work on liberated spodumene (LS), liberated quartz (LQ), mixed spodumene grains with a dominant spodumene component (MS) and mixed quartz grains with a dominant gangue component (MQ) (continued).

Tag	HL SG	Weight g	Weight %	Li %	Spd %	Non-spd %	Spd distribution %	Non-spd distribution %
MS Sink -9.5 +6.3mm	3.00	0.25	2.2	2.10	56.30	43.70	61.22	14.19
MS Sink -9.5 +6.3mm	2.85	4.6	39.8	1.30	34.85	65.15	37.90	21.15
MS Sink -9.5 +6.3mm	2.70	2.69	23.3					
MS Float -9.5 +6.3mm	-2.70	4.02	34.8	0.03	0.80	99.20	0.87	32.20
MS Feed -9.5 +6.3mm		**11.56**	**100.0**	**0.57**	**15.37**	**84.63**	**16.71**	**27.47**
MS Sink -6.3 +3.3mm	3.00	3.6	12.8	2.60	69.71	30.29	62.85	10.48
MS Sink -6.3 +3.3mm	2.85	4.75	16.8	1.50	40.21	59.8	36.26	20.68
MS Sink -6.3 +3.3mm	2.70	7.33	26.0					
MS Float -6.3 +3.3mm	-2.70	12.55	44.5	0.04	0.99	99.01	0.89	34.25
MS Feed -6.3 +3.3mm		**28.23**	**100.0**	**0.60**	**16.10**	**83.90**	**14.51**	**29.02**
MS Sink -3.3 +1.7mm	3.00	1.26	10.8	2.40	64.34	35.66	64.27	11.89
MS Sink -3.3 +1.7mm	2.85	2.42	20.8	1.30	34.85	65.15	34.82	21.72
MS Sink -3.3 +1.7mm	2.70	2.64	22.7					
MS Float -3.3 +1.7mm	-2.70	5.31	45.7	0.03	0.91	99.09	0.91	33.04
MS Feed -3.3 +1.7mm		**11.63**	**100.0**	**0.55**	**12.67**	**87.33**	**12.66**	**29.12**
MS Sink -1.7 +0.63mm	3.00	0.71	13.6	2.20	58.98	41.02	66.07	13.20
MS Sink -1.7 +0.63mm	2.85	1.11	21.2	1.10	29.49	70.51	33.03	22.69
MS Sink -1.7 +0.63mm	2.70	1.31	25.0					
MS Float -1.7 +0.63mm	-2.70	2.1	40.2	0.03	0.80	99.20	0.90	31.92
MS Feed -1.7 +0.63mm		**5.23**	**100.0**	**0.54**	**14.59**	**85.41**	**16.34**	**27.49**
Total MS Feed		**56.65**		**0.58**	**15.51**	**84.49**	**0.26**	**0.25**

Table 4.5 Outcome of HLS test work on liberated spodumene (LS), liberated quartz (LQ), mixed spodumene grains with a dominant spodumene component (MS) and mixed quartz grains with a dominant gangue component (MQ) (continued).

Tag	HL SG	Weight g	Weight %	Li %	Spd %	Non-spd %	Spd distribution %	Non-spd distribution %
MQ Sink -9.5 +6.3mm	3.00	0	0.0					
MQ Sink -9.5 +6.3mm	2.85	0.5	11.2					
MQ Sink -9.5 +6.3mm	2.70	1.2	26.9					
MQ Float -9.5 +6.3mm	-2.70	2.76	61.9	0.01	0.25	99.75	100.00	24.95
MQ Feed -9.5 +6.3mm		**4.46**	**100.0**	**0.01**	**0.15**	**99.85**	**61.88**	**24.98**
MQ Sink -6.3 +3.3mm	3.00	1.4	4.4	2.50	67.02	32.98	56.34	11.73
MQ Sink -6.3 +3.3mm	2.85	5.06	16.1	1.60	42.90	57.1	36.06	20.32
MQ Sink -6.3 +3.3mm	2.70	7.46	23.7	0.30	8.04	91.96	6.76	32.72
MQ Float -6.3 +3.3mm	-2.70	17.6	55.8	0.04	0.99	99.01	0.83	35.23
MQ Feed -6.3 +3.3mm		**31.52**	**100.0**	**0.46**	**12.32**	**87.68**	**10.36**	**31.20**
MQ Sink -3.3 +1.7mm	3.00	0.86	6.7	2.40	64.34	35.66	58.11	12.33
MQ Sink -3.3 +1.7mm	2.85	1.86	14.6	1.40	37.53	62.47	33.90	21.59
MQ Sink -3.3 +1.7mm	2.70	2.47	19.3	0.30	8.04	91.96	7.26	31.79
MQ Float -3.3 +1.7mm	-2.70	7.59	59.4	0.03	0.80	99.20	0.73	34.29
MQ Feed -3.3 +1.7mm		**12.78**	**100.0**	**0.44**	**12.67**	**87.33**	**11.44**	**30.19**
MQ Sink -1.7 +0.63mm	3.00	0.52	10.9					
MQ Sink -1.7 +0.63mm	2.85	0.57	12.0					
MQ Sink -1.7 +0.63mm	2.70	1.17	24.6					
MQ Float -1.7 +0.63mm	-2.70	2.5	52.5	0.02	0.56	99.44	100.00	24.89
MQ Feed -1.7 +0.63mm		**4.76**	**100.0**	**0.01**	**0.30**	**99.70**	**52.52**	**24.96**
Total MQ Feed		**53.52**		**0.38**	**10.12**	**89.88**	**0.40**	**0.24**

Table 4.5 Outcome of HLS test work on liberated spodumene (LS), liberated quartz (LQ), mixed spodumene grains with a dominant spodumene component (MS) and mixed quartz grains with a dominant gangue component (MQ) (continued).

Tag	HL SG	Weight g	Weight %	Li %	Spd %	Non-spd %	Spd distribution %	Non-spd distribution %
LQ Sink -9.5 +6.3mm	3.00	0.41	5.6	3.30	88.47	11.53	95.65	3.75
LQ Sink -9.5 +6.3mm	2.85	0	0.0					
LQ Sink -9.5 +6.3mm	2.70	2.84	38.8					
LQ Float -9.5 +6.3mm	-2.70	4.07	55.6	0.15	4.02	95.98	4.35	31.21
LQ Feed -9.5 +6.3mm		**7.32**	**100.0**	**0.27**	**7.19**	**92.81**	**7.78**	**30.18**
LQ Sink -6.3 +3.3mm	3.00	1.54	5.1	1.10	29.49	70.51	38.99	21.74
LQ Sink -6.3 +3.3mm	2.85	2.17	7.2	1.30	34.85	65.1	46.08	20.08
LQ Sink -6.3 +3.3mm	2.70	6.18	20.4	0.36	9.65	90.35	12.76	27.85
LQ Float -6.3 +3.3mm	-2.70	20.38	67.3	0.06	1.64	98.36	2.16	30.32
LQ Feed -6.3 +3.3mm		**30.27**	**100.0**	**0.26**	**7.07**	**92.93**	**9.35**	**28.65**
LQ Sink -3.3 +1.7mm	3.00	0.75	6.8	0.91	24.40	75.60	53.69	21.32
LQ Sink -3.3 +1.7mm	2.85	0.69	6.3	0.75	20.11	79.89	44.25	22.53
LQ Sink -3.3 +1.7mm	2.70	1.27	11.6					
LQ Float -3.3 +1.7mm	-2.70	8.24	75.3	0.04	0.94	99.06	2.06	27.94
LQ Feed -3.3 +1.7mm		**10.95**	**100.0**	**0.14**	**12.67**	**87.33**	**27.88**	**24.63**
LQ Sink -1.7 +0.63mm	3.00	0.3	6.9					
LQ Sink -1.7 +0.63mm	2.85	0.55	12.6	0.68	18.23	81.77	94.58	21.48
LQ Sink -1.7 +0.63mm	2.70	0.61	14.0					
LQ Float -1.7 +0.63mm	-2.70	2.9	66.5	0.04	1.05	98.95	5.42	25.99
LQ Feed -1.7 +0.63mm		**4.36**	**100.0**	**0.11**	**3.00**	**97.00**	**15.54**	**25.48**
Total LQ Feed		**52.90**		**0.23**	**6.04**	**93.96**	**0.20**	**0.25**

Table 4.5 provides information about the HLS tests and overall Li grades in each size and density fraction. When looking at the Li grade at each four samples, it can be seen that surprisingly the highest Li feed grade is seen for MS (0.58%) sample instead of LS (0.49%), which would have been more probable. The second highest Li% is in LS followed by MQ (0.38%) and lastly LQ (0.23%). This observation indicates firstly, that all of the samples contain lithium and secondly, that the MS sample contains more Li than LS even if the goal of the grain picking was opposite. This highlights the difficulty of visually distinguishing the spodumene grains from other gangue minerals and indicates that this goal was not quite achieved.

Another point that can be made by looking at the data from Table 4.5 is that the Li grades of the < 2.7 g/cm^3 density fractions are very low (between 0.01% and 0.15%) and represent less than 1% of the Li contained for the LS and MS samples in all size fractions. This indicates that lithium is almost never present as small inclusions in light minerals or as substitution in light minerals. Thus, it can be concluded that the light fraction represents mostly gangue material without significant Li-bearing phase. In the denser fractions (>3 g/cm³), the spodumene grade typically ranges between 50% and 70%, which suggests that other minerals are still attached to the spodumene. Additionally, suspiciously high Fe values were observed, suggesting that the iron grinding media and excessively long grinding time mentioned in section 3.3.2 have likely caused contamination. A substantial portion of the remaining impurity, however, is likely due to attached silicates, such as quartz, emphasizing that liberation is not yet complete in these samples.

Based on the data from Table 4.5, two types of graphs can be created. The first one, called mass distribution, represents how the mass of each sample is distributed among the different size and density classes. The second way to plot the data is to create 3D bar charts where the Li distribution %, particle size classes and different density fractions are shown indicating how the spodumene and therefore lithium is distributed within the different size and density classes.

Figure 4.6 presents the first type of these graphs for the four different samples, highlighting the mass distribution of the entire sample across various particle size classes and HLS specific gravity products. The X-axis displays the SG cut points (3.00, 2.85, 2.70, and <2.70 g/cm^3), while the color-coded bars represent different particle size fractions (+6.3 mm, +3.3 mm, +1.7 mm, +0.63 mm, and <0.63 mm). The Y-axis shows the proportion of total sample mass recovered in each SG

fraction. This visualization allows the assessment of how the overall sample mass is distributed across density fractions and particle sizes.

In Figure 4.6A, the bimodality of the finest size class (red bar) is clearly seen, with little mass content in the density classes between 2.7 and 3.0 g/cm^3, indicating higher liberation in this class. The red bar has the highest "peaks" at density class of 3 and -2.7 g/cm^3. This observation is consistent with the expectation that the finest class should have the best liberation, with liberated spodumene (ρ=3.2 g/cm^3), reporting in the sink at 3.0 g/cm^3 and the -2.7 g/cm^3 containing mostly liberated gangue. This bimodality appears reduced for coarser fractions, in agreement with a reduced liberation. A similar trend of increased bimodality (reduced amounts in the middle density fractions) is noticeable in the mixed spodumene sample (Figure 4.6C), lending more credit to the above observation.

Figure 4.6B, on the other hand, does not show obvious signs of increased bimodality for finer fractions, possibly due to the fact that the sample is mostly composed of gangue (quartz), with small amounts of spodumene and heavy minerals. The small amount of heavy minerals presents limits the ability to notice changes and may also indicate that the grains of spodumene are smaller and may not be significantly more liberated in the size classes characterized here. A similar behavior can be seen in Figure 4.6D where the mixed quartz (MQ) sample, which has a high portion of gangue minerals (mainly quartz), is presented. In this graph most of the mass is shifted (the highest bars) towards the right side of the graph. However, middle classes as well as the density class of 3.0 g/cm^3 contain more mass compared to the LQ sample, indicating that this sample contains a little bit more heavier particles which are likely to be spodumene. The reason why a clear bimodal pattern is not visible can be simply due to the lack of spodumene in the sample since this sample is supposed to contain only a small portion of spodumene. This is in agreement with the feed grades shown in Table 4.5.

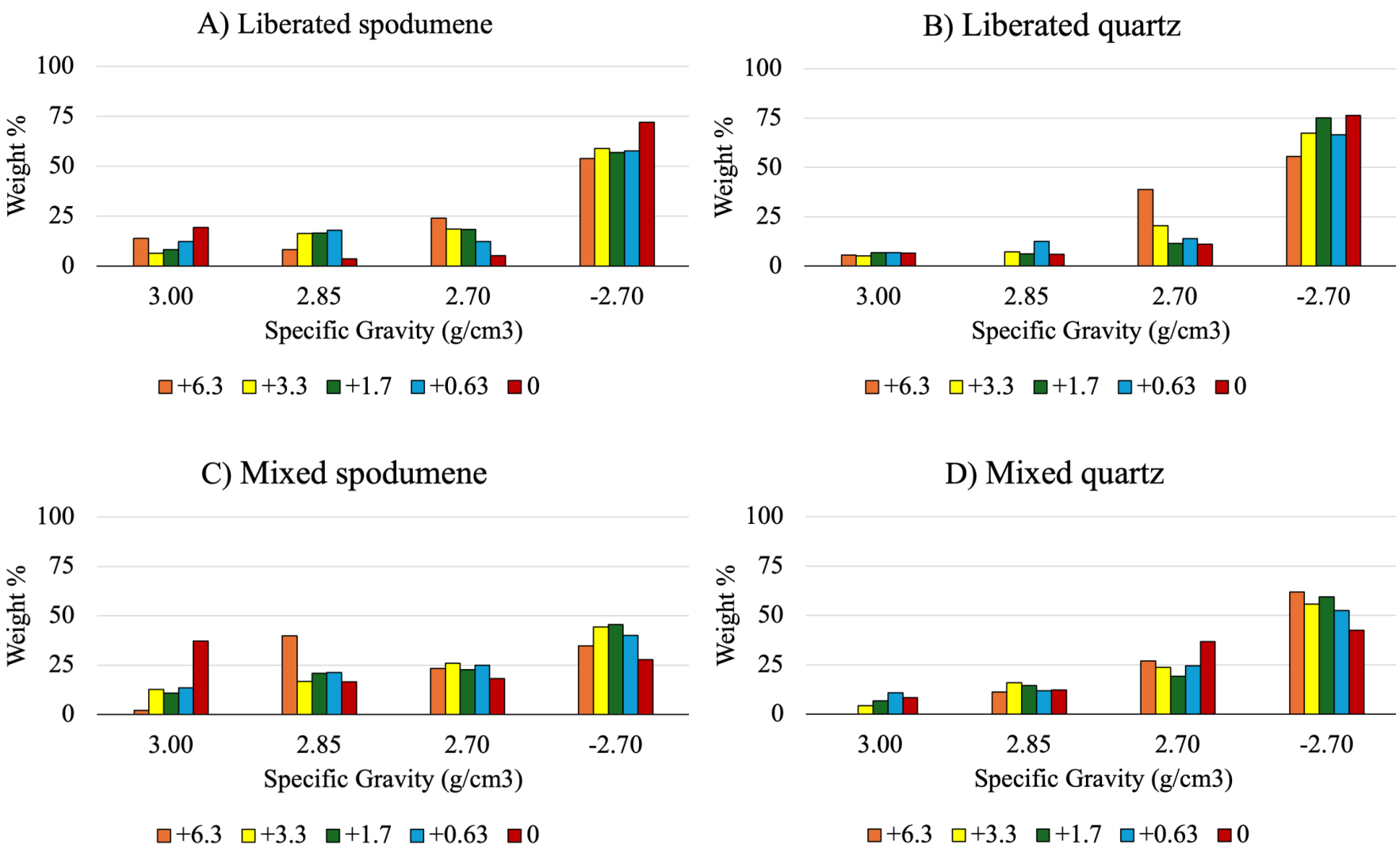

Figure 4.6 Mass distribution (%) of the samples across different S.G. fractions (3.00, 2.85, 2.70, and <2.70 g/cm³) and particle size classes. Each color represents a distinct size fraction, and the height of each bar indicates the proportion of the total sample mass recovered in the

Mass by density/size fraction data, however, remains limited in its ability to explain the relationships. Hence, in addition to weight % analysis, Table 4.5 includes data of spodumene and non-spodumene distributions. These columns provide more detailed information about how the spodumene is distributed among the different density fractions and particle size classes. Figure 4.7A illustrates this data for the liberated spodumene (LS) sample. A clear split is seen where the highest bars are located on the left side of the graph regardless of particle size class, meaning almost all the Li has sunk into the sink fraction when using HL densities 2.85 g/cm^3 or higher, in agreement with results from section 4.2. Another observation from this graph is that a decreasing trend is seen in each particle size class when the density is decreasing. This indicates that the less dense the heavy liquid used, the less likely it is for Li to report to the sink fraction, which is consistent if incomplete liberation of the material is at stake and increases as size decreases. Furthermore, when looking at the weight % data (Figure 4.6A) for this same sample, a small mass can also be seen in the middle-density fractions, with slightly more mass present in the 2.85 g/cm^3 density fraction than in the 2.7 g/cm^3 fraction. This could indicate that Li may also be present in the intermediate fractions.

Figure 4.7C presents the same data, but for the mixed spodumene (MS) sample. In this case, the main observation compared to Figure 4.7A is that the bars in each size class are more evenly distributed. This is consistent with the expected lower level of liberation of the sample, with this mixed spodumene sample containing more particles where quartz is attached to spodumene, compared to the liberated spodumene (LS) sample. Also, barely any effect of size class is noticeable in this sample, which indicates that the liberation pattern may differ from that of the LS sample.

This same difference in variation can also be seen in Figure 4.7B and Figure 4.7C, which present liberated quartz (LQ) and mixed quartz (MQ) samples respectively. Despite some lack of data points, among all four samples, the decrease of Li% seems to be following a more or less linear trend when shifting towards the low-density fractions. Table 4.6 shows R^2 values of this linear trend, between Li distribution % and different HL density fractions. In almost each size class, the correlation is over 90%, indicating a quasi-linear relation exists between density class and Li distribution.

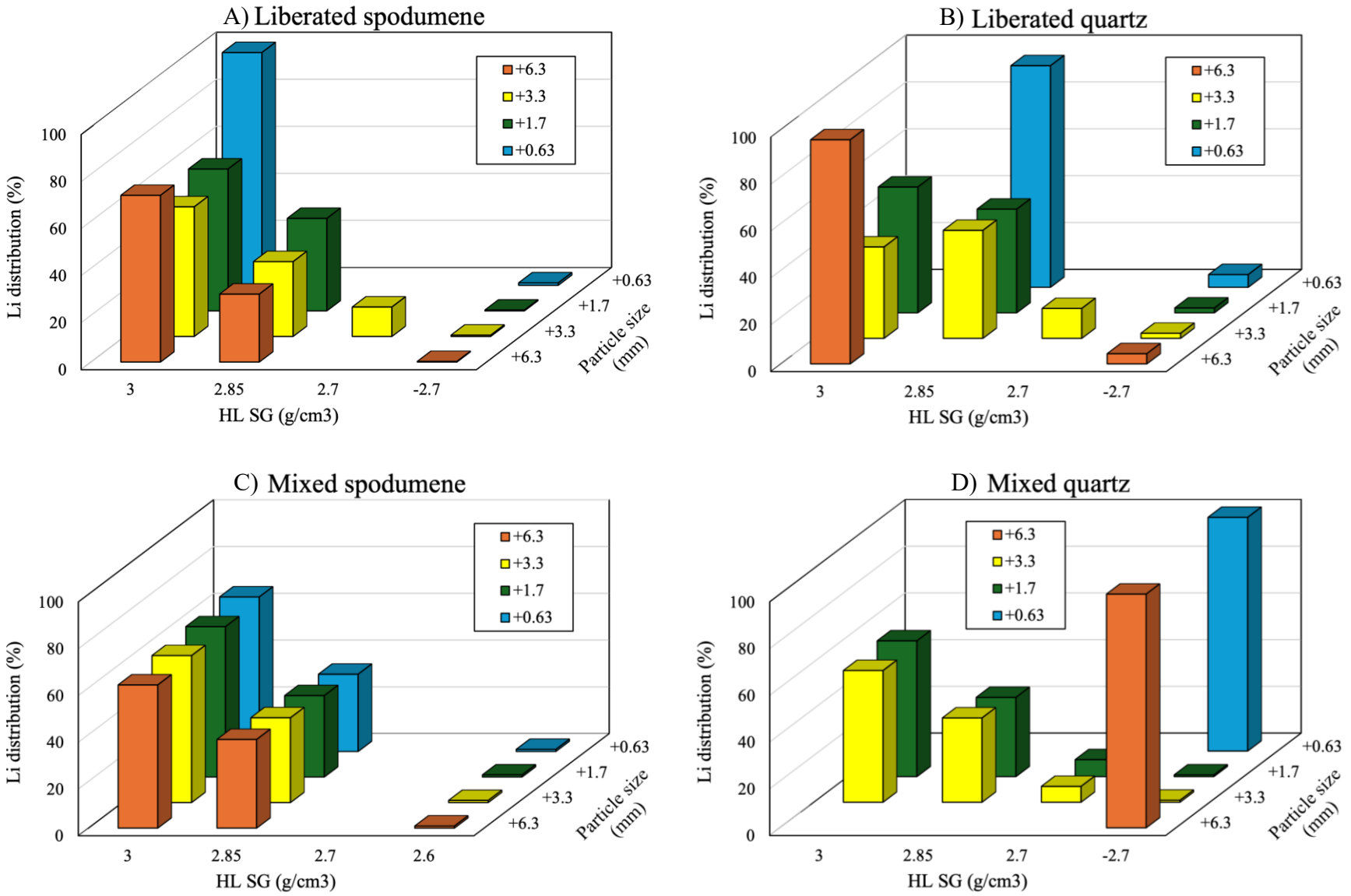

Figure 4.7 3D graph where different density fractions and particle size classes are plotted against Li distribution. A) liberated spodumene, B) liberated quartz, C) mixed spodumene and D) mixed quartz.

Table 4.6 Correlation between Li distribution % and density fraction for each particle size class.

Sample	Particle size (mm)	R^2
Liberated spodumene	+6.3	91.33%
	+3.3	98.08%
	+1.7	99.97%
	+0.63	-
Mixed spodumene	+6.3	99.64%
	+3.3	98.83%
	+1.7	97.78%
	+0.63	96.13%
Mixed quartz	+6.3	-
	+3.3	94.86%
	+1.7	95.02%
	+0.63	-
Liberated quartz	+6.3	-
	+3.3	78.84%
	+1.7	97.43%
	+0.63	-

Using this aforementioned observation, the linear relationship could be used to predict the portion of Li which reports to certain density classes. This information would enable better understanding prediction of DMS recovery. This means that if the correlation between Li distribution percent and density fraction is known, it becomes possible to estimate how much of the lithium content of particles in certain density class will report to the sink or float fraction during DMS processing. For example, if a particle is classified into a specific density class, one could predict that a certain proportion will end up in the sink fraction while the remainder will report to the float.

With more refinement in the grain size estimated from core samples and better understanding of the link with liberation, DMS performance may be predictable from drill core data without the need for extensive laboratory testing. As discussed earlier (section 4.1), the most significant variable influencing HLS Li recovery is the spodumene grain size interpreted from drill cores. This opens promising opportunities for automation by applying machine learning and image analysis techniques as it would be possible to objectively and more consistently evaluate grain size directly from drill core images. Such a system could significantly enhance geometallurgical modelling by providing fast, reproducible, and operator-independent estimates of spodumene liberation and expected DMS performance

Another interesting observation which can be made, after calculating a theoretical spodumene weight percentage, is the comparison between the actual spodumene content determined by chemical assay (ICP) and the maximum spodumene content that could theoretically exist in a given density fraction. This theoretical spodumene percentage was calculated based on the assumption that the particles in each density fraction consist of only spodumene and gangue (other minerals) and that these two components mix proportionally to achieve the average density.

Specifically, using the known densities of pure spodumene and gangue (assumed to be 3.2 g/cm³ and 2.65 g/cm³ respectively), it is possible to calculate the proportion of spodumene, and gangue required to reach the average density of a given fraction (for example, 2.925 g/cm³ for the 2.85–3.0 g/cm³ fraction). This is done by solving a mass balance equation where the weighted sum of the component densities equals the average density of the fraction:

$$\rho_{fraction} = x \cdot \rho_{Spd} + (1 - x) \cdot \rho_{Gangue} \quad 4.4$$

where $\rho_{fraction}$ is the measured average density of the density fraction, ρ_{Spd} and ρ_{Gangue} are the assumed densities of spodumene (3.2 g/cm³) and gangue (2.65 g/cm³), and x is the proportion of spodumene. Solving for x gives the theoretical spodumene percentage in that fraction.

The resulting theoretical spodumene percentage thus represents the theoretical maximum spodumene grade achievable if the particles in that density class were made up of only 3.2 g/cm³ spodumene and 2.65 g/cm³ gangue. Lastly, dividing the ICP assessed spodumene content (spd%) by this theoretical spodumene fraction (theoretical spd%), a "relative" spodumene content (relative spd%) is obtained. This value gives an indication of how close the spodumene content of the sample is to the maximum spodumene concentration possible in that density fraction, thereby reflecting the degree of spodumene purity or the extent to which the particles are composed of spodumene attached to gangue material vs. other minerals of this density. In other words, by comparing this theoretical maximum to the ICP-determined spodumene content, it can be seen if the class is made up of spodumene grains with gangue minerals attached to them or respectively, whether high-S.G. gangue minerals (such as tourmaline and garnet) are present. Table 4.7 presents both the ICP calculated spodumene percentages, the calculated theoretical maximum and the relative spd% value for each particle size and density fraction.

Table 4.7 Comparison between spodumene percentage determined by chemical assay (ICP) and the theoretical (calculated) maximum spodumene content for each density fraction and particle size class.

		3.0 g/cm^3 = 84.46% spd.max		2.85g/cm^3 = 54.70% spd.max		2.7g/cm^3 = 26.21% spd.max		-2.7g/cm^3 = 5.44% spd.max	
Sample	Size (mm)	Spd% (ICP)	Relative spd%	Spd% (ICP)	Relative spd%	Spd% (ICP)	Relative spd%	Spd% (ICP)	Relative spd%
Liberated spodumene	+6.3	72.39	85.70	29.49	53.91	-	-	0.24	4.44
	+3.3	69.71	82.53	40.21	73.52	15.82	60.35	0.70	12.81
	+1.7	61.66	73.01	40.21	73.52	-	-	0.35	6.41
	+0.63	56.30	66.66	-	-	-	-	0.59	10.84
Mixed spodumene	+6.3	56.30	66.66	34.85	63.72	-	-	0.80	14.78
	+3.3	69.71	82.53	40.21	73.52	-	-	0.99	18.23
	+1.7	64.34	76.18	34.85	63.72	-	-	0.91	16.76
	+0.63	58.98	69.83	29.49	53.91	-	-	0.80	14.78
Mixed quartz	+6.3	-	-	-	-	-	-	0.25	4.58
	+3.3	67.02	79.36	42.90	78.42	8.04	30.69	0.99	18.23
	+1.7	64.34	76.18	37.53	68.62	8.04	30.69	0.80	14.78
	+0.63	-	-	-	-	-	-	0.56	10.35
Liberated quartz	+6.30	88.47	104.75	-	-	-	-	4.02	73.92
	+3.30	29.49	34.92	34.85	63.72	9.65	36.82	1.64	30.06
	+1.70	24.40	28.89	20.11	36.76	-	-	0.94	17.25
	+0.63	-	-	18.23	33.33	-	-	1.05	19.22

For the mixed spodumene (MS) sample (+6.3 mm) in the 2.85–3.0 g/cm³ density fraction from Table 4.7, the ICP chemistry indicates that the actual spodumene content in this fraction is 34.85%, while the theoretical maximum spodumene content (assuming particles are composed solely of spodumene and attached gangue minerals with an average density of 2.925 g/cm³) is 54.7%. This suggests that 64% (34.85%/54.7%) of the particles are composed spodumene attached to light gangue, while 36% by mass is made up of mixtures of or pure high S.G. minerals. This supports the interpretation that most of the material is spodumene which is not fully liberated but that a minor amount of other dense minerals may be present.

One factor increasing the confidence in these results is that all measured ICP values fall below their respective theoretical maximum spodumene percentages, as expected. Only one value (LQ, +3.0 g/cm^3, +6.3mm) slightly exceeded its theoretical maximum, which is likely due to random variability or analytical uncertainty. This confirms that the theoretical calculations provide reasonable upper boundaries and that the ICP-based methodology produces results within logical limits, without overestimation of spodumene content.

Furthermore, in Table 4.7, relative spd % values, for the +3 g/cm^3 and +2.85 g/cm^3 fractions, tend to go down with size. This means that coarse sizes contain larger proportions of attached (unliberated spodumene), whereas finer sizes contain more other «heavy» minerals. Again, this is consistent with improved liberation at finer sizes and also supports the "selective" nature of spodumene liberation (Cunningham, 2025). Also, the relative spd% are rarely above 70-80%, which either means that there are always some 20-30% of other heavy minerals present, even in the +0.63mm fraction, of that the lithium was underestimated in some samples, or that using the average SG of the fraction 2.925 g/cm^3 in one instance is not quite accurate.

An optical microscopy was used for visual observations of the particles in order to compare the visual nature of the particles to chemical data. As seen from Figure 4.8, spodumene, the most abundant mineral, appears light gray and is characterized, at least in the Shaakichiuwaanaan deposit, by black tourmaline inclusions (Zhang et al., 2008). In the grain on the left side of the image, the black inclusions tend to be oriented, which is another feature suggesting that they are mostly aligned with the cleavage planes of spodumene. Some white albite and quartz mixture can also be seen, particularly on the right side of the image. This image again shows how visual estimation of minerals from microscopy images is difficult, even for large grains. Moreover,

surface examination of these large grains does not show what is on the other side of the grain nor whether some mineral inclusions lie inside the particle.

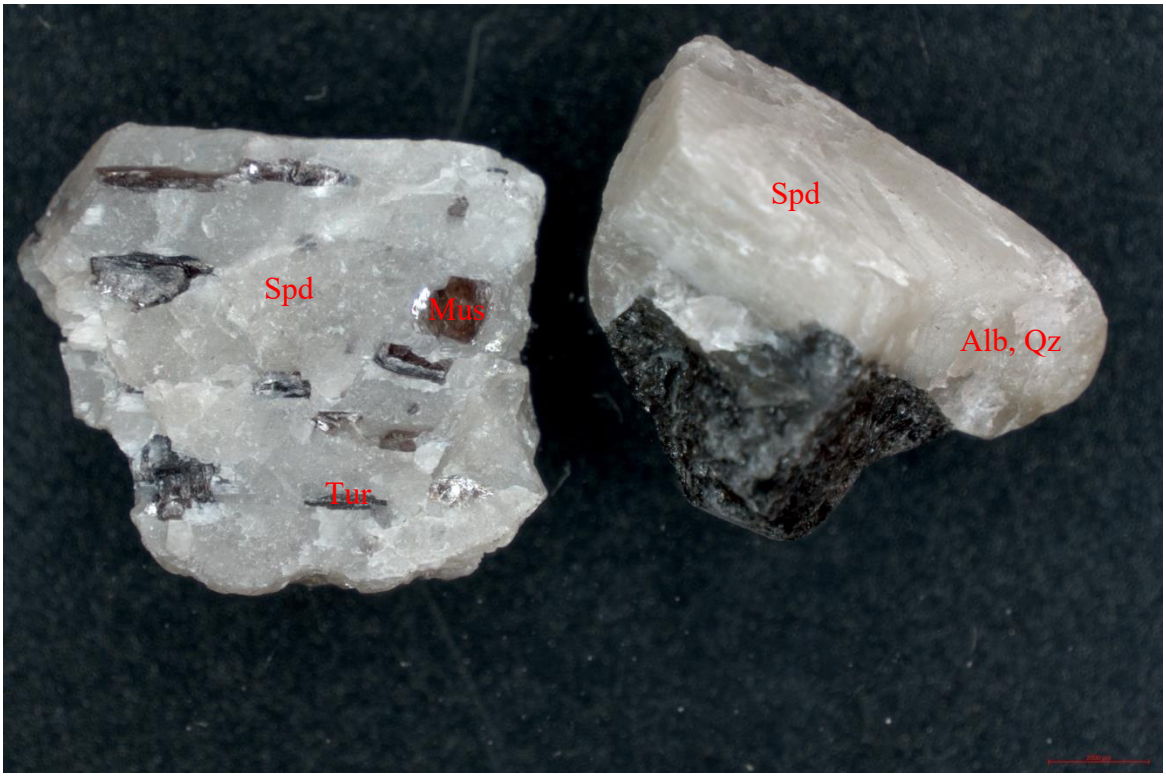

Figure 4.8 Optical microscopy image on the mixed spodumene sample (+6.3mm, 2.85g/cm3). Spodumene (spd), muscovite (Mus), tourmaline (Tur), albite (Alb), and quartz (Qz) are marked in the image.

Lastly, in an effort to improve the completeness of the data in terms of size fractions, exploratory centrifugation testing was attempted on the -630 µm fraction in a HL with a density of 2.85 g/cm^3. The visual outcome of the centrifuge test is shown in Figure 4.9, where sink (dark color) and float (light color) are clearly shown. This observation shows that it is possible to separate spodumene from the gangue by using HL in the centrifuge. This approach may facilitate bulk HL testing where the presence of excessive amounts of fine particles can complicate the procedure due to incomplete separation.

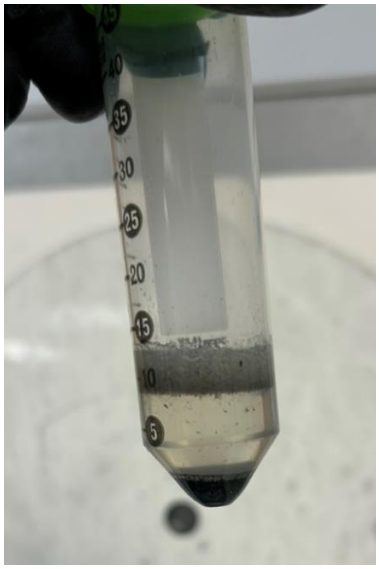

Figure 4.9 After centrifugation of fines, two clearly separated phases were present.

As Figure 4.10 shows, the separation appeared successful, since the color of the sink fraction is more gray/light greenish with some dark/black particles, which could point to spodumene and tourmaline, respectively. On the other hand, the float fraction is clearly whiter, indicating the presence of feldspar and quartz. The actual chemical composition of the sink and float fractions, shown in Table 4.8, reveals that the % Li is almost 30 times higher in the sink fraction than in the float fraction, confirming that separation by centrifugation worked well decreased the separation time compared to traditional HLS test for fine particles. The low amount of lithium in the float fraction also indicates a very high degree of liberation in this fraction. While current DMS methods do not allow for separation in these particle size classes, this analysis reveals that the degree of liberation will not be an impediment, should developments in fine DMS methods or other means allow for their recovery.

Figure 4.10 Sink (left) and float (right) fraction of fine particle (-0.6mm) centrifugation under the optical microscopy. 1 cm in the image represents 5000 μm in reality.

Table 4.8 Chemical assay results of fine fraction (-0.6mm) centrifugation testwork.

Fraction	Mass %	Li (%)
Float	44.4	0.049
Sink	55.6	1.4

In summary, the laboratory HLS tests provide valuable insight into spodumene liberation, which has been identified as the key factor controlling lithium recovery in gravity separation. The test results highlight that effective separation is directly linked to achieving sufficient spodumene liberation, as reflected by the strong correlation between grain size, density fractions, and Li recovery. Furthermore, as discussed in the previous sections (see section 4.2), high-grade material tends to deliver better recovery because it typically requires less crushing to achieve the necessary liberation. This is attributed to the fact that high-grade material often contains larger initial spodumene grain sizes, which can already be observed at the core logging stage (see Table 4.3). However, the current grain size estimation method lacks sufficient resolution, making accurate grain size determination difficult. Nonetheless, since 94%, 88% and 99% of the grains in the samples PBM-comp001, PBM-comp002 and PBM-comp003, respectively, are larger than 7 mm, these observations strongly suggest that spodumene grain size, visible during core logging, is a critical parameter for predicting lithium recovery. Although geological logging remains a subjective method, the results show it performs adequately in predicting recovery potential. This

supports the need for grain size estimation methods including those in the next section which utilize image analysis and machine learning to create more objective and consistent evaluations of spodumene grain size directly from core image, in order to support better recovery predictions.

4.4 MACHINE LEARNING AND IMAGE PROCESSING

A machine learning algorithm was applied to estimate spodumene grain size based on RGB images of the 11 composite samples from PBM's Shaakichiuwaanaan deposit. This section presents and discusses these results. Most importantly, the estimation of spodumene grain size and evaluation of the model's performance are covered and the new correlation coefficients and R^2 values of the new models are compared to the previous models based solely on the geologists' estimations (section 4.1).

The performance of each ML classification model is presented as a confusion matrix in Figure 4.11, where Y-axes refer to manually labeled classes by PhD student in geology (true class) while the X-axes show the predicted classes by machine (predicted class). In the diagonal, the confusion matrices show the percentages of superpixels which the machine has classified correctly. A color code was implemented for clarity, meaning that the darker blue on the diagonal, the more accurate the classification process has been. Other, non-diagonal, elements (orange/brownish color) represent incorrectly identified superpixels. The percentage on each square indicates the total percentage of superpixels classified into each predicted class, relative to the total number of true samples in that row. High non-diagonal values indicate confusion between classes, whereas higher diagonal values (blue) reflect accurate predictions.

The different ML models can be compared based on the confusion matrices shown in Figure 4.11. All three models CART (A), Random Forest (B), and k-NN (C) demonstrate relatively high accuracy in identifying the "Undetermined" class, containing mostly dark shadow and edge areas, with over 90% correct classification. This is likely due to the high number of labelled training data and the obvious features differing clearly from other classes. Notable differences arise in the classification of spodumene superpixels however. The Random Forest model achieves the highest accuracy for spodumene (51.6%), slightly outperforming CART (43.5%) and k-NN (50.2%). Despite this, all models exhibit significant confusion between spodumene and gangue, as indicated by high non-diagonal values (e.g., 46.2% of spodumene was misclassified as gangue in Random

Forest). The confusion between the gangue and spodumene classes is likely due to the similarity of their extracted features. Additionally, the training data labeling process may have introduced some bias: the focus was primarily on identifying spodumene, and any superpixel that was not spodumene was automatically labeled as gangue. This resulted in a broad and heterogeneous range of superpixels being assigned to the gangue class, making it more difficult for the model to learn distinct and consistent characteristics for gangue. This suggests that while Random Forest performs slightly better overall, the overlapping visual or textural features between spodumene and gangue remain a challenge for accurate classification. Additionally, marker class identification is relatively weak across all models, with high misclassification rates, particularly into spodumene. This behavior can be explained simply by the lack of training data making the classification challenging.

Despite the confusion between spodumene and gangue, the MATLAB-based code performs as intended, demonstrating that fully automated, machine learning–based superpixel classification is technically feasible. However, as previously stated, the primary objective of this study is not to develop a finalized machine learning tool. The results presented here are based on a manually labeled dataset, where classification was performed by human interpretation rather than an automated algorithm. This approach aligns with the proof-of-concept nature of the work, aiming to evaluate the potential and limitations of such a system. The findings of this thesis serve as a foundation for future development, where the focus can shift toward building a more automated and robust machine learning framework.

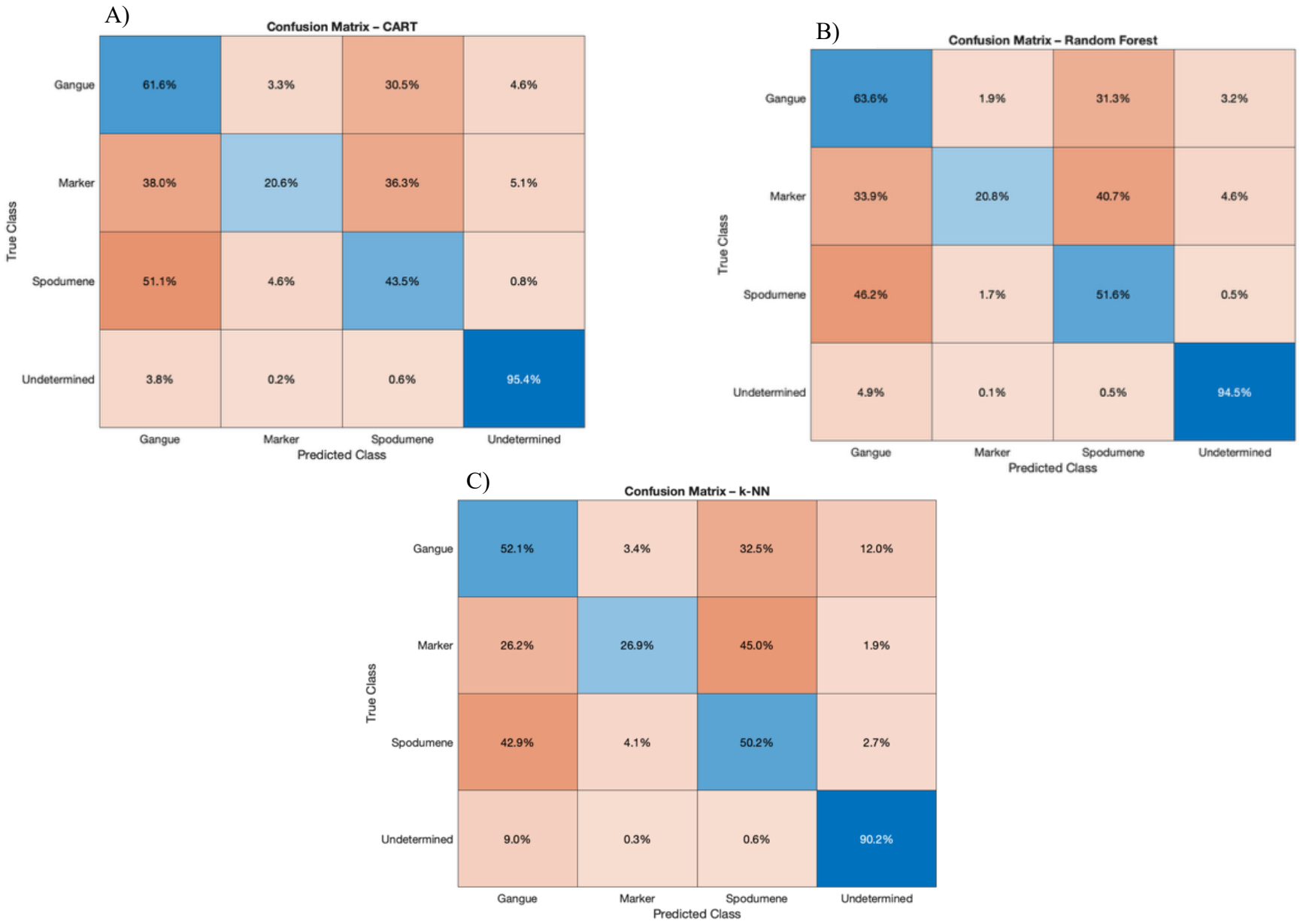

Figure 4.11 Confusion matrices for each ML model. Y-axes represents the actual True Classes determined by geologiests whereas X-axes shows the predicted classes by the ML algorithm. A) CART, B) Random Forest and C) k-NN.

Different grain size metrics were obtained, as explained in Chapter 3.4.3, from spodumene grains identified by a geology PhD student Neila Seray. The average grain sizes (eight metrics) for each of the 11 composite samples are presented in Table 4.9. The table also includes the original Li recovery % from HLS testing and the percentage of spodumene grains larger than 7 mm (%Spd grains > 7 mm), as estimated by geologists at PBM. In addition, a volume-weighted average equivalent diameter (deq) is shown to better illustrate the distribution of different grain sizes. Lastly, the P80 value indicates the particle size below which 80% of the sample's mass is contained.

As shown in Table 4.9, samples with a higher percentage of coarse (>7 mm) spodumene grains, such as Composites 1, 4, 9, and 11, also exhibit higher recovery rates, due to the fact that coarser particles settle much faster than fines because terminal settling velocity increases strongly with particle size (for small particles this follows Stokes' law). Faster settling lets the density contrast control the separation and gives a sharper split, so misplacement drops. Fines increase slurry viscosity, stay in suspension longer, and are easily carried into the wrong product. Therefore, coarse spodumene grains are typically recovered more efficiently in DMS/HLS than fine ones. Therefore, composites 6 and 10, which have both lower %Spd grains > 7 mm and smaller average grain size values across multiple metrics (e.g., d_{eq}, d_{ins}, and d_{Fmax}), demonstrate lower recovery. This reinforces the previously mentioned relationship between grain coarseness and separation performance. In addition, each grain's equivalent diameter (d_{eq}) can be multiplied by its respective grain volume, and the total divided by the sum of all volumes, to weight the contributions and ensure that larger grains, which represent a larger mass have a greater influence on the final average than if grains are simply weighted on a unit-basis. As can be expected, these weighted d_{eq} and P_{80} values follow a similar pattern.

Table 4.9 Mean grain size metrics and corresponding HLS recovery by interval group.

Metric	Comp1	Comp2	Comp3	Comp4	Comp5	Comp6	Comp7	Comp8	Comp9	Comp10	Comp11
HLS Li Recovery (%)	92.20	82.70	90.10	86.60	91.40	61.00	80.50	85.50	92.50	79.00	92.20
% spd grains >7mm	100.00	97.44	96.90	100.00	100.00	81.00	91.11	86.39	100.00	94.00	100.00
%Li (ICP)	0.61	0.57	0.46	0.59	0.78	0.26	0.75	0.70	0.89	0.47	1.21
Mean deq (mm)	39.80	34.27	21.00	19.00	28.00	16.53	34.00	20.00	19.00	41.00	35.90
Mean dins (mm)	29.32	25.08	29.54	28.63	31.44	13.92	25.92	29.12	33.95	20.45	28.84
Mean dFmax (mm)	133.32	87.31	21.04	20.82	22.66	30.75	22.93	17.18	26.91	16.09	114.83
Mean Area (mm^2)	1559.67	1273.41	59.45	73.17	73.97	256.52	54.65	65.53	79.16	41.81	1473.35
Mean lell (mm)	145.38	90.95	826.96	846.14	991.52	28.46	701.89	801.37	1202.68	363.55	124.85
Mean sell (mm)	42.11	37.10	58.19	75.61	76.52	21.86	54.82	66.02	82.23	41.21	37.46
Mean wrec (mm)	126.26	79.89	34.36	32.21	33.37	24.00	30.21	30.46	37.56	24.45	106.72
Mean hrec (mm)	37.95	34.47	50.03	66.62	66.54	21.25	46.34	60.19	70.98	35.26	35.18
Weighted d_{eq}*	60.36	65.38	33.49	30.32	32.00	26.71	29.87	30.49	35.47	23.61	78.87
P_{80}	57.02	47.62	47.79	54.11	56.37	22.52	49.73	45.42	58.34	26.19	54.16

* Weighted d_{eq} is calculated by weighting each grain's equivalent diameter (d_{eq}) by its volume, ensuring that larger grains have a proportionally greater influence on the average.

To better understand the data shown in Table 4.9, Table 4.10 presents the R^2 and correlation coefficient values between the various metrics and the HLS Li recovery for each composite, both with and without applying a logarithmic scale. This table provides valuable guidance for selecting the most suitable metrics for grain size estimation and Li HLS recovery prediction. As seen in Table 4.10, the highest R^2 value (75%) is obtained using the average height of the bounding rectangle (h_{rec}) in relation to HLS Li recovery. The second strongest relationship (R^2 = 72%) is achieved using the average equivalent area diameter (d_{eq}). When applying a logarithmic scale (log_{10}), the R^2 values increase significantly, and the prediction ability of d_{eq} exceeds that of h_{rec} with the strongest observed relationship (80%) to HLS Li recovery.

Table 4.10 R^2 values between grain size metrics and HLS Li recovery, with and without logarithmic transformation.

Metric	R^2	R^2 log_{10}
Mean d_{eq} (mm)	0.72	0.80
Mean d_{ins} (mm)	0.55	0.61
Mean d_{Fmax} (mm)	0.50	0.68
Mean Area (mm^2)	0.59	0.75
Mean l_{ell} (mm)	0.48	0.68
Mean s_{ell} (mm)	0.69	0.75
Mean w_{rec} (mm)	0.49	0.68
Mean h_{rec} (mm)	0.75	0.78
Weighted d_{eq}	0.53	0.60
P_{80}	0.62	0.70

One of the main advantages of using machine-based grain size detection is that it enables access to grain size distribution, adding a whole new dimension to the characterization of drill cores and the extracted data. While average grain size analysis provides a single numerical value, grain size distributions offer a more comprehensive view, revealing the distribution of grain sizes. This is especially important because a sample composed of a single large grain and many small grains can have the same average grain size as a sample with uniform mid-size grains, but very different separation performance. Since processing depends on mass, the use of cumulative volume fraction helps capture how grain mass is actually distributed within the sample.

Figure 4.12 presents the grain size distribution curves for composite samples, based on the equivalent-area diameter (d_{eq}) of individual grains. These cumulative curves reveal not only the

average grain size but also the full internal variability of each sample. This type of data is currently unattainable through visual geological logging, where grain size is estimated visually and typically reported as a single value or a few approximate ranges. Machine-based analysis enables the extraction of full distributions, allowing more robust comparisons between samples. For example, composites 2 and 11 exhibit a broader grain size range and higher maximum diameters, while composites 6 and 10 remain consistently finer across all percentiles. This highlights the potential of using grain size distribution instead of a single average, especially when correlating mineral characteristics to process behavior such as HLS Li recovery.

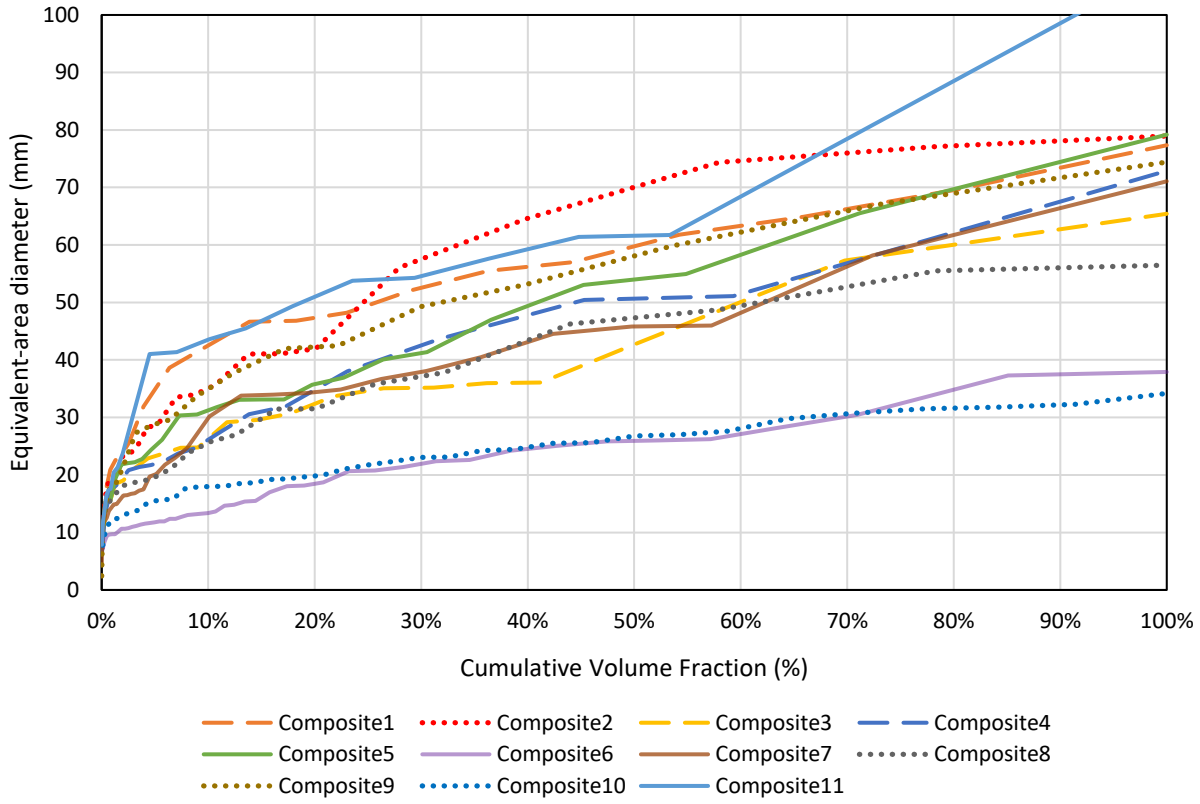

Figure 4.12 Spodumene grain size distribution curves for composite samples.

In Table 4.11, the grain size distribution values (D_{10}, D_{50}, and D_{90}) are presented for the various composite samples. The D_{50} refers to the grain size at which 50% of the sample's mass is smaller, while the same principle applies to D_{10} and D_{90} for the 10% and 90% thresholds, respectively. Notably, samples of composites 6 and 10 exhibit the lowest HLS Li recoveries, 61% and 79%, respectively, and at the same time have the smallest D_{10} values: 13.34 mm and 17.97 mm. This observation supports the hypothesis that finer grain sizes are associated with reduced recovery

efficiency, possibly due to insufficient liberation or challenges in separation. In addition, the ratio between D_{90} and D_{10} and the spodumene % estimation based on the computer image analysis (discussed with more details later in Figure 4.15) is presented in the table.

Table 4.11 Grain size distribution and image analysis estimated spodumene concentration for 11 composite samples.

Sample	HLS Li Recovery (%)	D_{10} (mm)	D_{50} (mm)	D_{90} (mm)	D_{90} / D_{10} (mm)	Actual Spd %	Image analysis estimated spd %
Comp1	92.20	42.54	59.75	73.44	1.73	17	25.43
Comp2	82.70	35.06	70.03	78.09	2.23	14	20.57
Comp3	90.10	26.30	42.71	62.74	2.39	14	11.09
Comp4	86.60	26.12	50.64	67.53	2.59	17	11.09
Comp5	91.40	31.25	53.98	74.43	2.38	21	19.00
Comp6	61.00	13.34	25.93	37.49	2.81	8	2.78
Comp7	80.50	29.84	45.84	66.40	2.22	20	10.03
Comp8	85.50	25.56	47.31	56.04	2.19	17	12.87
Comp9	92.50	34.93	58.10	71.68	2.05	25	18.51
Comp10	79.00	17.97	26.76	32.19	1.79	15	7.29
Comp11	92.20	61.60	98.55	98.55	1.60	34	35.06

Using the data obtained from the geologist team at PBM (percentage of spodumene grains >7 mm), the current spodumene grain size estimation procedure results in an R^2 of 71.05% in relation to the HLS Li recovery when applying a linear model, and 71.78% when using a logarithmic trendline, the latter being shown in Figure 4.13A). As a result of the third sub-objective (see chapter 1.2), a new grain size estimation was provided by using RGB images and machine learning. Figure 4.13B) shows the correlation between the new estimated size of spodumene grains (d_{eq}) and the HLS Li recovery. The R^2 value is increased to 79.72% when using machine-based grain size estimation, meaning the use of machine learning can provide results which are more closely relatable to processing performance. Both trendlines were selected to be logarithmic, which reflects the existence of a plateau *i.e.* even if the grain size increases indefinitely, the HLS Li recovery cannot exceed 100%. In addition, it is worth testing these new image-based variables in order to evaluate their power of prediction in models 1 and 2. All these variables were $\log_{10}$-normalized prior to model fitting. In model 1, adding new machine-derived variables like D_{90} or D_{90}/D_{10} did not change performance or significance. In model 2, "Computer estimated spd%" yielded a higher R^2 (77.88%) than "Spodumene grains > 7 mm" (71.78%). Both machine-derived variables, image-based grain size and estimated spodumene percentage, resulted in higher R^2 values than visual grain size assessment, highlighting the benefits of automated image analysis over traditional logging.

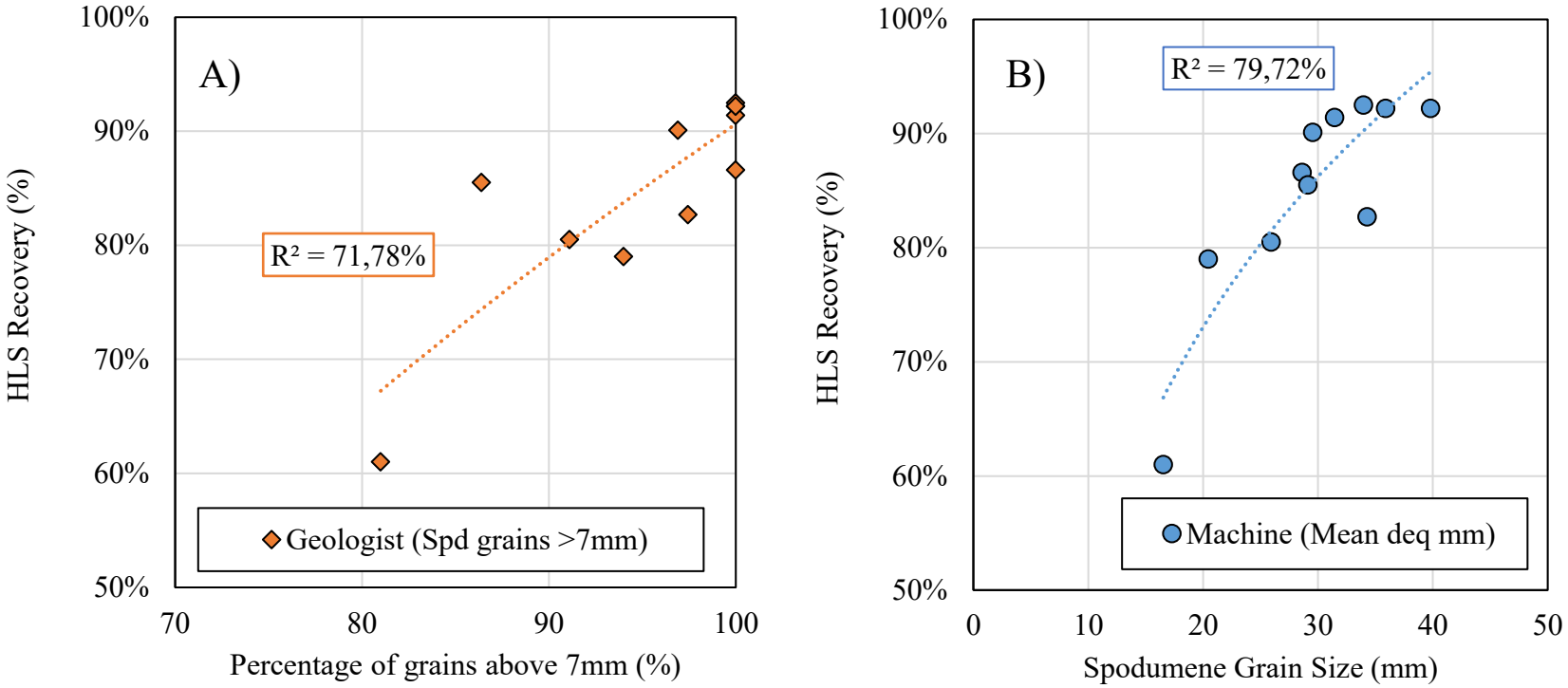

Figure 4.13 Relationship between spodumene grain size and HLS recovery.

Figure 4.14 shows a fitted grain size distribution curve of a spodumene-rich composite sample, modeled using two commonly applied functions in mineral processing: the Gates-Gaudin-Schuhmann (GGS) and the Rosin-Rammler-Sperling (RRS) distributions (see chapter 3.3.1). These theoretical models are compared against the actual cumulative volume data obtained from image analysis. Both models demonstrate a good fit, particularly in the mid-range grain sizes, with the RRS model aligning more closely at the finer end whereas GGS performs better at the coarse end. Although these models are traditionally used for estimating grain size distributions of crushed material, their application here serves primarily to validate the reliability and consistency of the image-derived grain size data. The fact that the machine-based grain size distribution follows these classical models reasonably well adds credibility to the approach, as it indicates that the data behaves in a way that is consistent with established patterns in mineral processing. This improves confidence in the image analysis method and supports its integration into process simulation and design. While these models are useful for simplifying complex grain size distributions, they may miss small variations or multiple grain size peaks. Hence, using them together with the full measured data remains important to ensure clarity and accuracy in mineral characterization.

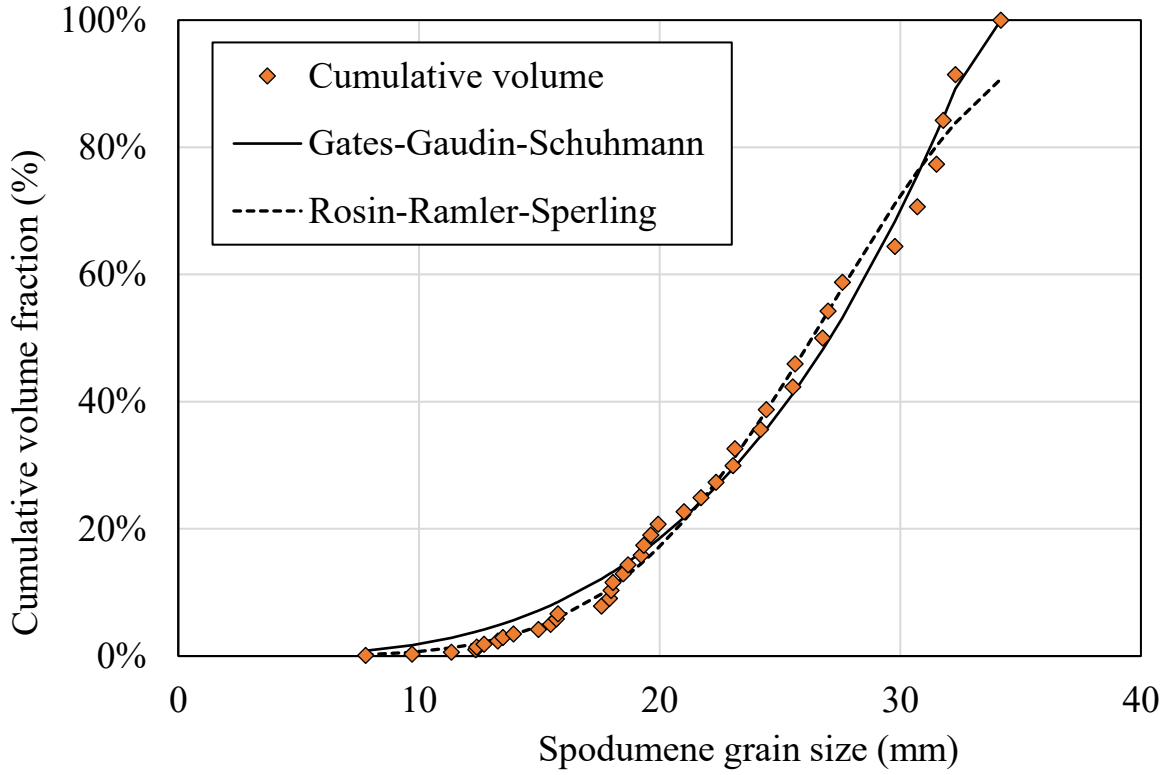

Figure 4.14 Grain size distribution fitted with Gates-Gaudin-Schuhmann and Rosin-Rammler-Sperling models, compared to actual cumulative volume data of a liberatede spodumene-rich drill core interval (composite 10).

Another capability sought by such an image processing approach is to estimate the spodumene percentage of each drill core interval based on images. Since the software detects spodumene superpixels within each core interval, using either manual labeling or potentially machine-based labeling in the future, the corresponding area (and volume) can then be calculated. The software calculates also the area of the whole drill core image, using pixels as a unit. Since the focus is on the ratio between the area of spodumene and the area of the whole drill core, the units in question are not important as long as they are the same. Then this ratio can easily be converted into percentages which represent the "coverage %" of spodumene in each drill core. The geologists at PBM use the same approach but conduct it manually, relying on the human eye and brain, which provide a first impression of the spodumene grade (spodumene %) in each particular drill core interval. After, half of the core is sent to the laboratory where it undergoes more detailed analysis, such as XRD and ICP analysis, resulting in an accurate evaluation of the spodumene content. Lastly, the comparison between the estimation by geologists and the measured spodumene % can be made. According to the core logging data provided by the company, the geologists' visual

estimation of spodumene percentage yielded R^2 values of 33.3% with ICP results and 36.7%, with XRD results, respectively.

Figure 4.15 below illustrates the improvement to the accuracy and representativeness which the use of machine learning enables. Orange diamonds represent the spodumene % estimated by geologists whereas the blue diamonds refer to the same estimation done by machine learning supported image analysis. The new approach provides almost double the R^2 value, reaching almost 63%. Specifically,

Figure 4.15 shows how the new method appears less prone to error in high grade samples, which could also be explained by the added difficulty of visually differentiating and averaging spodumene content at such high grades. However, neither approach goes through the origin, showing that both may be prone to underestimation of low spodumene grades (<10%). It also seems that visual estimation overestimates the amount of spodumene in the drill core. In addition, such a figure ideally should produce a 1:1 line as shown in red in Figure 4.15. The trend line of computer image analysis (dotted line) follows the red line with a same slope, just a little off set whereas the visual assessment (full line) has a different slope and does not fit as nicely. This observation supports the fact that the computer image analysis outperformed the visual assessment.

Overall, the ML approach enables more accurate spodumene grade estimation than the current method provides. The upside of the machine-based estimation is not only better accuracy but also the possibility to get information on other minerals than spodumene, as the same procedure can be applied for gangue minerals in case some of them are of interest. In addition, if the machine learning algorithm can be fully automated, the assistance for geologists can result in real time savings.

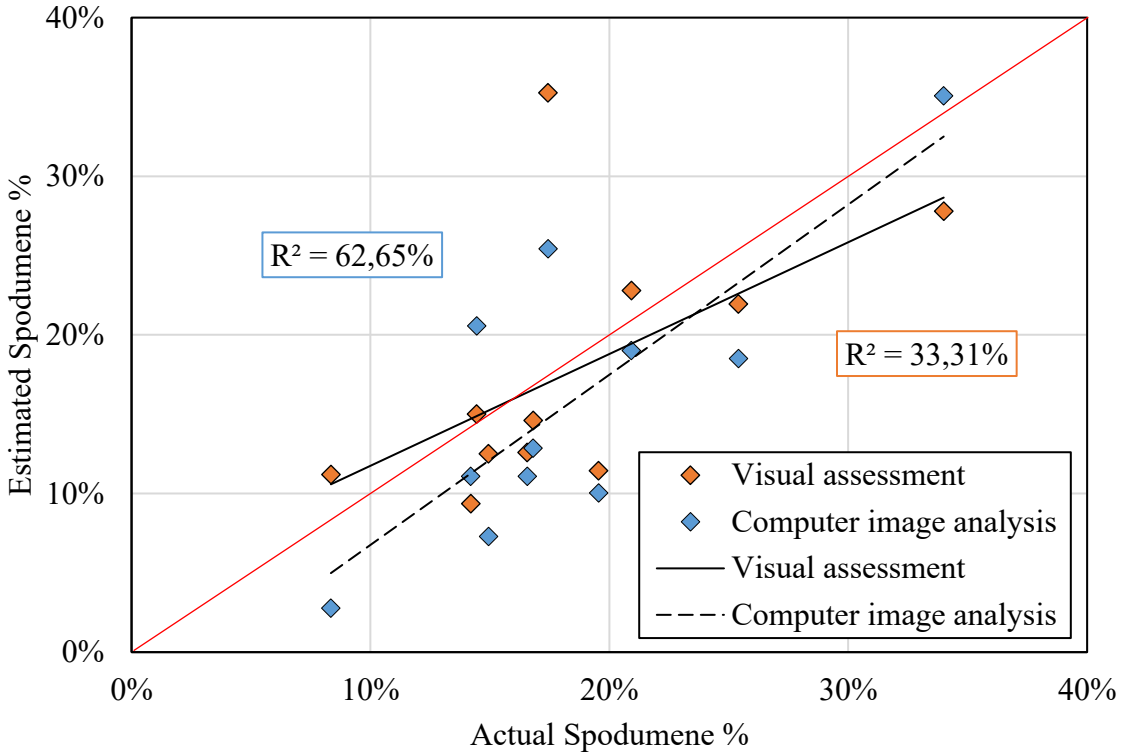

Figure 4.15 Comparison between visual and computer-estimated spodumene contents and actual ICP-measured values using Li2O content.

The strong potential in using image analysis and AI applications can improve the objectivity of core logging. As mentioned earlier, the current logging protocol at PBM classifies grain sizes into <2 mm, 2–7 mm, and >7 mm categories. Image analysis produced an average spodumene grain size (average d_{eq}) of approximately 30 mm, which is significantly larger than 7 mm breaking point used. Even though this value appears high, it should be noted that the apparent grain size is constrained by the size of the core and the orientation of the elongated spodumene crystals within it, as these factors can lead to an underestimation or overestimation of true grain dimensions. According to Wills & Finch (2016), to achieve a high level of liberation (around 75%), the sample should be crushed so that the resulting particle size is about one-tenth of the original grain size. Considering this and the average grain size obtained from image analysis, the product size after crushing should be approximately 3 mm to achieve roughly 75% liberation. However, such an intensive size reduction can be problematic in DMS process where the goal is to have as large particles as possible to avoid losing the recovery of Li to fines. Specifically, crushing the material to $1/10^{th}$ of the original grain size is likely to produce too much fine material which will not be

going to the DMS process but to tailings or, in the best of cases, to a flotation circuit. Keeping this in mind, the more optimal crush size is likely to be more than 3 mm value stated above. This may explain the choice for PBM to target a crush size of 9.5mm which corresponds to a 0.316 particle to grain size ratio (assuming grain size around 30mm). This would mean roughly 40% fraction of liberated minerals. Therefore, as in many cases, the selected crush size is a compromise between liberation and recovery.

This aligns with the observations from Section 4.3.2, where the liberation of the high-grade spodumene sample (PBM test work) was studied using size by size HLS testing. Although the material was not exactly the same as that used in image analysis, the results provide a good indication and confirmation that the theoretical methodology works. Assuming that the original grain size of the PBM samples was similar to that obtained from image analysis, the 75% liberation rate was achieved in the +1.7–3.3 mm particle size class. As discussed in Section 4.3.2, liberation in that class was not complete but was likely at the 75% level. Even in the finer class (+0.63–1.7 mm), liberation was not 100%, although it was clearly higher than in the coarser class.

CHAPTER 5 CONCLUSION

This study set out to explore how geological data, particularly visual spodumene grain size estimations, can be integrated into a geometallurgical framework to improve the prediction of spodumene gravity separation performance. The main objective was to enhance the understanding of how mineralogical and geological characteristics influence HLS spodumene recovery, using cost-effective and accessible data sources. To support this, drill core logging data was compared with HLS test results to establish correlations and a predictive model.

Laboratory HLS test work provided validation for these observations. The tests suggest that spodumene liberation is the key factor for lithium recovery in gravity separation. A strong correlation was observed between grain size, density fraction, and Li recovery, highlighting the impact that liberation has on separation performance. The results showed that high-grade material, typically containing larger spodumene grains, achieves better recovery because it requires less crushing to reach the desired liberation level. This supports the conclusion that spodumene grain size, visible even at the core logging stage, is the most significant parameter affecting Li recovery.

In addition, since spodumene grain size has such a strong influence on lithium recovery, the study also investigated how image analysis could improve the consistency and objectivity of visual core logging. Although a fully automated image analysis method was not implemented, the developed workflow demonstrated that optical image-based methods can produce reliable grain size distribution data without destructive testing or intensive laboratory work.

This research demonstrates that spodumene grain size, particularly the mean equivalent diameter (d_{eq}), is a strong predictor of spodumene recovery in HLS tests. Notably, the ML model achieved an R^2 value of 79.72% for the correlation between machine-estimated d_{eq} and HLS spodumene recovery at an SG of 2.85 g/cm^3, compared to 71.78% for the geologists' visual estimates. These findings show that grain sizes, which are in the cm range for spodumene samples investigated, can be measured from images and used to estimate how easily the ore can be processed, especially when mineral liberation plays a key role in separation efficiency.

In addition to single-value grain size estimates, this study introduced the use of grain size distribution curves derived from the RGB images. These distributions provide a more detailed

picture of the internal heterogeneity within each sample and were found to follow established particle size models such as Gates-Gaudin-Schuhmann and Rosin-Rammler-Sperling. This opens possibilities for using image-based grain size distributions in other process modeling contexts. Furthermore, the possibility of estimating spodumene percentages based on the relative superpixel area offers another layer of interpretability. When compared to visual estimates, the machine-based spodumene percentage prediction achieved a correlation coefficient of 79.2% and an R^2 of 62.65%, almost doubling those performance indicators compared to manual logging. These findings create a foundation for future tools that could help geologists make more consistent and data-based interpretations across larger datasets.

5.1 RECOMMENDATIONS

The results of this research support several practical recommendations for future work and application. The main recommendations are as follows:

1) Maximize image resolution: The quality of feature extraction and machine learning model training is highly dependent on image resolution.
2) Optimize lighting conditions: Ensure even, diffused lighting with appropriate angles to minimize shadows and reflections, especially on wet core surfaces.
3) Use closed photographic systems: Enclosed systems (e.g., like those by Kore Geosystems Inc) can improve image consistency and quality.
4) Capture images before logging: Photographing cores before adding annotations or tags could produce cleaner data for machine learning.
5) Consider switching to Python: Converting the code to Python would allow use of advanced tools like Meta AI's Segment Anything Model for better segmentation.

5.2 FUTURE WORK

This research has proved the concept of applying machine learning in a geometallurgical framework and has shown an improvement in accuracy and reproducibility when compared to visual estimation by humans. However, automatization and optimization of this methodology should be done in the future to realize the full potential of this approach. The future focus should be on developing autonomous drill core grain detection and segmentation to replace the current manual process of selecting regions of interest (ROI) from the core images. Moreover, optimizing the training data collection and its use for training the ML models. Also, the code for superpixel prediction using CART, k-NN and RF needs to be optimized in order to achieve the best possible outcome.

As stated above, the best possible outcome may not be achievable using traditional machine learning models such as CART, k-NN, and Random Forest. Instead, the use of deep learning methods may be more suitable for this type of classification task. For instance, Convolutional Neural Network (CNN) could potentially yield better results, as it is capable of learning and recognizing complex patterns in image data more effectively than conventional models (Latif et al., 2022).

In order to fully integrate this methodology into an industrial-scale operation, where economic feasibility and profitability play an increasingly important role, a direct link between HLS performance and actual DMS outcomes should also be established. This likely would result from a detailed liberation study involving several samples, crushed at different sizes, in order to establish the breakage patterns and their variations. Once such relationships are established and the code is further developed to enable full automation, it may be valuable to test whether the algorithm can also be applied to crushed samples i.e. to see if grain size and liberation can be estimated from photos of crushed samples. Although such an approach may require the use of other detection methods such as LIBS or Raman spectroscopy (Laitinen et al., 2024) to confirm whether a grain is spodumene or not, if successful, it could be implemented directly on a conveyor belt, where images of the crushed material are captured in real time. This setup could serve as an early-stage prediction tool for spodumene recovery, offering rapid and non-destructive feedback on ore quality during processing.

REFERENCES

Abdullah, A. A., Oskierski, H. C., Altarawneh, M., Senanayake, G., Lumpkin, G., & Dlugogorski, B. Z. (2019). Phase transformation mechanism of spodumene during its calcination. *Minerals Engineering*, *140*. https://doi.org/10.1016/j.mineng.2019.105883

Achanta, R., Shaji, A., Smith, K., Lucchi, A., Fua, P., & Süsstrunk, S. (2010). *SLIC Superpixels*.

Acke, J., Kwizera, D., Goodship, A., Dewaele, S., Barros, R., Burlet, C., Nachtergaele, S., & Borst, A. (2023). *Spodumene textural variations in a deformed LCT-type pegmatite. A case study from the Musha-Ntunga area, Rwanda*.

Acosta, I. C. C., Khodadadzadeh, M., Tolosana-Delgado, R., & Gloaguen, R. (2020). Drill-core hyperspectral and geochemical data integration in a superpixel-based machine learning framework. *IEEE Journal of Selected Topics in Applied Earth Observations and Remote Sensing*, *13*, 4214–4228. https://doi.org/10.1109/JSTARS.2020.3011221

Aghamirian, M., & Imeson, D. (2023). *An investigation into variability heavy liquid separation testwork on samples from the Corvette property, James Bay, Quebec prepared for Patriot Battery Metals Inc*.

Aha, D. W., Kibler, D., Albert, M. K., & Quinian, J. R. (1991). Instance-Based Learning Algorithms. *Machine Learning*, *6*, 37–66.

Ait-Khouia, Y., Benzaazoua, M., & Demers, I. (2021). Environmental desulfurization of mine wastes using various mineral processing techniques: Recent advances and opportunities. *Minerals Engineering*, *174*. https://doi.org/10.1016/j.mineng.2021.107225

Alderliesten, M. (2013). Mean particle diameters. Part VII. the Rosin-Rammler size distribution: Physical and mathematical properties and relationships to Moment-Ratio defined mean particle diameters. *Particle and Particle Systems Characterization*, *30*(3), 244–257. https://doi.org/10.1002/ppsc.201200021

Ambrós, W. M. (2023). Gravity Concentration in Urban Mining Applications—A Review (CC by 4.0). *Recycling*, *8*(6). https://doi.org/10.3390/recycling8060085

Aylmore, M. G., Merigot, K., Rickard, W. D. A., Evans, N. J., McDonald, B. J., Catovic, E., & Spitalny, P. (2018). Assessment of a spodumene ore by advanced analytical and mass

spectrometry techniques to determine its amenability to processing for the extraction of lithium. *Minerals Engineering*, *119*, 137–148. https://doi.org/10.1016/j.mineng.2018.01.010

Back, A. L., Kana Tepakbong, C., Bédard, L. P., & Barry, A. (2025). From rocks to pixels: a comprehensive framework for grain shape characterization through the image analysis of size, orientation, and form descriptors. *Frontiers in Earth Science*, *13*. https://doi.org/10.3389/feart.2025.1508690

Bae, H., & Kim, Y. (2021). Technologies of lithium recycling from waste lithium ion batteries: A review. *Materials Advances*, *2*(10), 3234–3250. https://doi.org/10.1039/d1ma00216c

Barton, N., Lienand, R., & Lunde, J. (1974). Engineering classification of rock masses for the design of tunnel support. *Rock Mechanics*, *6*, 189–236.

Baruya, P. (2012). *Losses in the coal supply chain*. https://doi.org/10.13140/RG.2.2.19769.26727

Becker, M., Miller, J. A., Becker, M., & Harris, M. (2016, June 15). *X-ray Computed Tomography-a Geometallurgical Tool for 3D Textural Analysis of Drill Core?* http://www.microtec.eu

Benchmark Mineral Intelligence. (2025). *Lithium Prices, Forecasts & Market Analysis | Benchmark Mineral Intelligence*. https://www.benchmarkminerals.com/lithium

Biau, G., & Scornet, E. (2016). A random forest guided tour. *Test*, *25*(2), 197–227. https://doi.org/10.1007/s11749-016-0481-7

Bieniawski, Z. (1973). Engineering classification of jointed rock masses. *The Journal of the South African Institution of Civil Engineering*, *15*, 333–343.

Bons, P. D., Elburg, M. A., & Gomez-Rivas, E. (2012). A review of the formation of tectonic veins and their microstructures. *Journal of Structural Geology*, *43*, 33–62. https://doi.org/10.1016/j.jsg.2012.07.005

Brandt, F., & Haus, R. (2010). New concepts for lithium minerals processing. *Minerals Engineering*, *23*(8), 659–661. https://doi.org/10.1016/j.mineng.2010.03.021

Breiman, L. (2001). Random Forests. *Machine Learning*, *45*, 5–32.

Bright, S., Conner, G., Turner, A., & Vearncombe, J. (2014). Drill core, structure and digital technologies. *Transactions of the Institutions of Mining and Metallurgy, Section B: Applied Earth Science*, *123*(1), 47–68. https://doi.org/10.1179/1743275814Y.0000000051

Bulatovic, S. (2015). *Handbook of Flotation Reagents: Chemistry, Theory and Practice, Beneficiation of Lithium Ores* (S. Bulatovic, Ed.; Vol. 3). Elsevier. https://doi.org/10.1016/B978-0-444-53083-7.00003-8

Cacciari, P. P., & Futai, M. M. (2019). Effects of mica content on rock foliation strength. *International Journal of Rock Mechanics and Mining Sciences*, *124*. https://doi.org/10.1016/j.ijrmms.2019.104143

Central Chemical Consulting. (2024, May 28). *LST Heavy Liquid for float sink separations*. https://www.chem.com.au/heavy_liquid.html#sds

Charoy, B., Noronha, F., & Lima, A. (2001). Spodumene-petalite-eucryptite: mutual relationships and pattern of alteration in Li-rich aplite-pegmatite dykes from northern Portugal. *The Canadian Mineralogist*, *39*, 729–746.

Chauhan, S., Rühaak, W., Khan, F., Enzmann, F., Mielke, P., Kersten, M., & Sass, I. (2016). Processing of rock core microtomography images: Using seven different machine learning algorithms. *Computers and Geosciences*, *86*, 120–128. https://doi.org/10.1016/j.cageo.2015.10.013

Chischi, J. (2023). *Alteration of spodumene (LiAlSi2O6) and its impact on the recovery of lithium*. Murdoch University.

Chornkrathok, S., Dera, P., Nguyen, P. Q. H., & Downs, R. T. (2024). Heavy Liquid Separation Method for Enhancement of Trace Asbestos Detection. *Crystals*, *14*(2). https://doi.org/10.3390/cryst14020127

Choubey, P. K., Kim, M. S., Srivastava, R. R., Lee, J. C., & Lee, J. Y. (2016). Advance review on the exploitation of the prominent energy-storage element: Lithium. Part I: From mineral and brine resources. *Minerals Engineering*, *89*, 119–137. https://doi.org/10.1016/j.mineng.2016.01.010

Colton, J. W. (1957). Recovery of Lithium from Complex Silicates. In *Advances in Chemistry* (Vol. 19, pp. 3–8). American Chemical Society. https://doi.org/10.1021/ba-1957-0019.ch001

Contreras, C., Khodadadzadeh, M., Ghamisi, P., Gloaguen, R., & Dresden-Rossendorf, H.-Z. (2019, July 28). *Mineral mapping of drill core hyperspectral data with extreme learning*.

Cook, B. K., Aghamirian, M., & Gibson, C. E. (2023). Optimization of spodumene flotation with a fatty acid collector. *Minerals Engineering*, *204*. https://doi.org/10.1016/j.mineng.2023.108412

Cracknell, M. J., & Reading, A. M. (2014). Geological mapping using remote sensing data: A comparison of five machine learning algorithms, their response to variations in the spatial distribution of training data and the use of explicit spatial information. *Computers and Geosciences*, *63*, 22–33. https://doi.org/10.1016/j.cageo.2013.10.008

Cunningham, P., Cord, M., & Delany, S. J. (2008). Supervised Learning. In P. Cunningham, M. Cord, & S. J. Delany (Eds.), *Machine Learning Techniques for Multimedia* (1st ed., pp. 21–49). Springer Verlag GmbH. https://doi.org/https://doi.org/10.1007/978-3-540-75171-7_2

Cunningham, R. (2025, January 21). Dense medium separation performance estimation from heavy liquid separation results. *57th CMP Annual Meeting Proceedings 2025*.

Dana, E. S. (1922). *A text book of Mineralogy with an extended treatise on crystallography and physical minealogy* (W. Ford, Ed.; 3rd ed.). John Wiley & Sons.

David, D. M. (2019). Geometallurgy. In C. Young (Ed.), *SME mineral processing & extractive metallurgy handbook* (p. 2019). Society for Mining, Metallurgy & Exploration (SME). http://ebookcentral.proquest.com/lib/ulaval/detail.action?docID=5649299.

Deere, D. (1963). Technical Description of Rock Cores for Engineering Purposes. *Rock Mechanics and Engineering Geology*, *1*(1), 16–22.

Dessemond, C., Lajoie-Leroux, F., Soucy, G., Laroche, N., & Magnan, J. F. (2019). Spodumene: The lithium market, resources and processes. *Minerals*, *9*(6). https://doi.org/10.3390/min9060334

Dominy, S. C., O'connor, L., Parbhakar-Fox, A., Glass, H. J., & Purevgerel, S. (2018). Geometallurgy—A route to more resilient mine operations. *Minerals*, *8*(12). https://doi.org/10.3390/min8120560

Ertel, W. (2024). Introduction (N. T. Black, Trans.). In *Introduction to Artificial Intelligence* (3rd ed., pp. 1–23). Springer Wiesbaden. https://doi.org/10.1007/978-3-658-43102-0_1

Ferrari, F., Apuani, T., & Giani, G. P. (2014). Rock Mass Rating spatial estimation by geostatistical analysis. *International Journal of Rock Mechanics and Mining Sciences*, *70*. https://doi.org/10.1016/j.ijrmms.2014.04.016

Filippov, L., Farrokhpay, S., Lyo, L., & Filippova, I. (2019). Spodumene flotation mechanism. *Minerals*, *9*(6). https://doi.org/10.3390/min9060372

Frenzel, M., Baumgartner, R., Tolosana-Delgado, R., & Gutzmer, J. (2023, December 1). Geometallurgy: Present and Future. *Elements*, *19*(6), 345–351. https://doi.org/10.2138/gselements.19.6.345

Gao, T. ming, Fan, N., Chen, W., & Dai, T. (2023). Lithium extraction from hard rock lithium ores (spodumene, lepidolite, zinnwaldite, petalite): Technology, resources, environment and cost. *China Geology*, *6*(1), 137–153. https://doi.org/10.31035/cg2022088

Gibson, C., Aghamirian, M., & Grammatikopoulos, T. (2017). The beneficiation of lithium minerals from hard rock deposits. *Mining Engineering*, *69*(8). www.miningengineeringmagazine.com

Gibson, C. E., Aghamirian, M., Grammatikopoulos, T., Smith, D. L., & Bottomer, L. (2021). The recovery and concentration of spodumene using dense media separation. *Minerals*, *11*(6). https://doi.org/10.3390/min11060649

Glacialle, T. (2017). *Classification of Drill Core Textures for Process Simulation in Geometallurgy*. Luleå University of Technology.

Gohau, G., Carozzi, A. V, & Carozzi, M. (1990). *A History of Geology*. Rutgers University Press. https://books.google.ca/books?id=GBG7XDS5CbwC

Gonzalez, R. C. ., & Woods, R. E. . (2018). *Digital image processing* (4th ed.). Pearson.

Grew, E. S. (2020). The minerals of lithium. *Elements*, *16*(4), 235–240. https://doi.org/10.2138/GSELEMENTS.16.4.235

Grosjean, C., Herrera Miranda, P., Perrin, M., & Poggi, P. (2012). Assessment of world lithium resources and consequences of their geographic distribution on the expected development of the electric vehicle industry. In *Renewable and Sustainable Energy Reviews* (Vol. 16, Issue 3, pp. 1735–1744). https://doi.org/10.1016/j.rser.2011.11.023

Guiral, J. S. (2018). *Textural and mineralogical characterization of Li-pegmatite deposit: Using microanalytical and image analysis to link micro and macro properties of Spodumene in drill cores*. https://doi.org/10.13140/RG.2.2.20597.22243

Gutiérrez, R., Vergani, G., De La Hoz, M., & Rodríguez, L. G. (2022). *Potential resources of lithium from oilfield brines in Neuquén Basin, Argentina*. 215. http://www.e3metalscorp.

Halder, R. K., Uddin, M. N., Uddin, M. A., Aryal, S., & Khraisat, A. (2024). Enhancing K-nearest neighbor algorithm: a comprehensive review and performance analysis of modifications. *Journal of Big Data*, *11*(1). https://doi.org/10.1186/s40537-024-00973-y

Harvey, A. S., & Fotopoulos, G. (2016). Geological mapping using machine learning algorithms. *International Archives of the Photogrammetry, Remote Sensing and Spatial Information Sciences - ISPRS Archives*, *41*, 423–430. https://doi.org/10.5194/isprsarchives-XLI-B8-423-2016

Hauff, P. L., & Airey, J. (1980). *The Handling, Hazards, and Maintenance of Heavy Liquids in The Geologic Laboratory*.

Hodgman, C., Coolbaugh, M., & Senseman, C. (2014). *CRC Handbook of Chemistry and Physics* (W. M. Haynes, D. R. Lide, & T. J. Bruno, Eds.; 95th ed.). Taylor and Francis.

Hood, S. B., Cracknell, M. J., & Gazley, M. F. (2018). Linking protolith rocks to altered equivalents by combining unsupervised and supervised machine learning. *Journal of Geochemical Exploration*, *186*, 270–280. https://doi.org/10.1016/j.gexplo.2018.01.002

Janiesch, C., Zschech, P., & Heinrich, K. (2021). Machine learning and deep learning. *Electronic Markets*, *31*, 685–695. https://doi.org/10.1007/s12525-021-00475-2/Published

Jaskula, B. (2024). *Mineral Commodity Summaries*. https://pubs.usgs.gov/periodicals/mcs2024/mcs2024-lithium.pdf

Jeppson, D., Ballif, J., Yuan, W., & Chou, B. (1978). *Lithium literature review: lithium's properties and interactions*.

Kaplan, U. E., & Topal, E. (2020). A new ore grade estimation using combine machine learning algorithms. *Minerals*, *10*(10), 1–17. https://doi.org/10.3390/min10100847

Kawatra, S. K. (2019). Physical Separations. In C. Young (Ed.), *SME mineral processing & extractive metallurgy handbook*. Society for Mining, Metallurgy & Exploration (SME). http://ebookcentral.proquest.com/lib/ulaval/detail.action?docID=5649299.

Kirillov, A., Mintun, E., Ravi, N., Mao, H., Rolland, C., Gustafson, L., Xiao, T., Whitehead, S., Berg, A. C., Lo, W.-Y., Dollár, P., & Girshick, R. (2023). *Segment Anything*. https://segment-anything.com.

Koch, E.-C., & Jennings-White, C. (2009, August 23). Is it possible to Obtain a Deep Red Pyrotechnic Flame Based on Lithium? *36th International Pyrotechnics Seminar*.

Koch, P. H., Lund, C., & Rosenkranz, J. (2019). Automated drill core mineralogical characterization method for texture classification and modal mineralogy estimation for geometallurgy. *Minerals Engineering*, *136*, 99–109. https://doi.org/10.1016/j.mineng.2019.03.008

Koch, P.-H. (2019). *Computational Methods and Strategies for Geometallurgy* [Luleå University of Technology]. www.ltu.se

Kohitlhetse, I., Rutto, H., Motsetse, K., & Manono, M. (2023). Grindability, Energy Requirements and Gravity Separation of Quartz from Blast Furnace Ironmaking Slag by Shaking Table and Falcon Concentrator. *Engineering Proceedings*, *37*(1). https://doi.org/10.3390/ECP2023-14691

Krivovichev, V. G., Charykova, M. V., & Krivovichev, S. V. (2018). The concept of mineral systems and its application to the study of mineral diversity and evolution. *European Journal of Mineralogy*, *30*(2), 219–230. https://doi.org/10.1127/ejm/2018/0030-2699

Kundu, T., Dash, N., Parhi, P. K., Sangurmath, P., & Angadi, S. I. (2023). Characterization and gravity concentration studies on spodumene bearing pegmatites of India. *Separation Science and Technology (Philadelphia)*, *58*(13), 2331–2343. https://doi.org/10.1080/01496395.2023.2258273

Kunii, D., & Levenspiel, O. (1991). *Butterworth-Heinemann Series in Chemical Engineering SERIES EDITOR Chemical Process Structures and Information Flows* (2nd ed.). Butterworth-Heinemann.

Laitinen, T., Legault, M., Ojala, S., & Boulanger, J. (2024). Assessment of Time-Gated Raman Spectroscopy for Online Mineralogy of a Spodumene Ore. *Journal of Raman Spectroscopy*. https://doi.org/10.1002/jrs.6748

Latif, G., Bouchard, K., Maitre, J., Back, A., & Bédard, L. P. (2022). Deep-Learning-Based Automatic Mineral Grain Segmentation and Recognition. *Minerals*, *12*(4). https://doi.org/10.3390/min12040455

Leite, E. P., & de Souza Filho, C. R. (2009). Artificial neural networks applied to mineral potential mapping for copper-gold mineralizations in the Carajás Mineral Province, Brazil. *Geophysical Prospecting*, *57*(6), 1049–1065. https://doi.org/10.1111/j.1365-2478.2008.00779.x

Lemy, F., Hadjigeorgiou, J., Côté, P., & Maldague, X. (2013). Image analysis of drill core. *Institution of Mining and Metallurgy. Transactions. Section A: Mining Technology*, *110*(SEPT/DEC). https://doi.org/10.1179/mnt.2001.110.3.172

Lewis, R. J. (2000). *An Introduction to Classification and Regression Tree (CART) Analysis Introduction to CART*. 419–608.

Li, Z., & Chen, J. (2015). Superpixel Segmentation using Linear Spectral Clustering. *Proceedings of the IEEE Conference on Computer Vision and Pattern Recognition (CVPR)*, 1356–1364.

London, D. (1984). Experimental phase equilibria in the system LiAlSiO4–SiO2–H2O: a petrogenetic grid for lithiumx-rich pegmatites. *American Mineralogist*, *69*(11–12), 995–1004.

London, D. (2017). Reading Pegmatites: Part 3—What Lithium Minerals Say. *Rocks and Minerals*, *92*(2), 144–157. https://doi.org/10.1080/00357529.2017.1252636

LST Heavy Liquid SDS. (2016).

Luong, V. T., Kang, D. J., An, J. W., Kim, M. J., & Tran, T. (2013). Factors affecting the extraction of lithium from lepidolite. *Hydrometallurgy*, *134–135*, 54–61. https://doi.org/10.1016/j.hydromet.2013.01.015

Mahesh, B. (2020). Machine Learning Algorithms - A Review. *International Journal of Science and Research (IJSR)*, *9*(1), 381–386. https://doi.org/10.21275/art20203995

Maitre, J., Bouchard, K., & Bédard, L. P. (2019). Mineral grains recognition using computer vision and machine learning. *Computers and Geosciences*, *130*, 84–93. https://doi.org/10.1016/j.cageo.2019.05.009

Mama, A. (2023). *Determination Of Work Index of Spodumene from Kenticha Ore, Southern Ethiopia Graduate Project*. Addis Ababa institute of technology.

Marcinov, V., Klimko, J., Takáčová, Z., Pirošková, J., Miškufová, A., Sommerfeld, M., Dertmann, C., Friedrich, B., & Oráč, D. (2023). Lithium Production and Recovery Methods: Overview of Lithium Losses. *Metals*, *13*(7). https://doi.org/10.3390/met13071213

Marion, A. (1991). Introduction to Image Processing (C. Polley, Trans.). In *Introduction to Image Processing* (1st ed.). Springer US. https://doi.org/10.1007/978-1-4899-3186-3

Mathieu, L. (2018). Quantifying hydrothermal alteration: A review of methods. *Geosciences (Switzerland)*, *8*(7). https://doi.org/10.3390/geosciences8070245

May, J. T., Witkowsky, D. S., & Seidel, D. C. (1980). *Extracting Lithium From Clays by Roast-Leach Treatment* (Vol. 8523). U.S. Department of the Interior, Bureau of Mines.

McMillan, G. (1999). *Process/ industrial instruments and controls handbook gregory k. mcmillan editor-in-chief fifth edition mcgraw-hill* (D. Considine, Ed.; 5th ed.).

Meshram, Pandey, B. D., & Mankhand, T. R. (2014). Extraction of lithium from primary and secondary sources by pre-treatment, leaching and separation: A comprehensive review. *Hydrometallurgy*, *150*, 192–208. https://doi.org/10.1016/j.hydromet.2014.10.012

Meshram, R. R., Singh, B., Mishra, M. K., Hrushikesh, H., Siddiqui, A., Shukla, D., Akhtar, R., & Meshram, T. M. (2021). Petrological and Geochemical Studies of Lepidolite (LCT Type) and Non-Lepidolite Pegmatite's from Chakrasila, Dhubri District, Assam, North East India. *Open Journal of Geology*, *11*(03), 81–104. https://doi.org/10.4236/ojg.2021.113006

Milne, D., Hadjigeorgiou, J., & Pakalnis, R. (1998). Rock Mass Characterization for Underground Hard Rock Mines. *Tunnelling and Underground Space Technology*, *13*(4), 383–391.

Montgomery, D. C. . (2017). *Design and analysis of experiments* (9th ed.). John Wiley & Sons, Inc.

Mounteney, I. (2011). *The use of lithium heteropolytungstate as an alternative to bromoform for heavy media separations*.

Napier-Munn, T. (2018). The dense medium cyclone – past, present and future. *Minerals Engineering*, *116*, 107–113. https://doi.org/10.1016/j.mineng.2017.10.002

Naseri, A., & Rezaei Nasab, A. (2023). Automatic identification of minerals in thin sections using image processing. *Journal of Ambient Intelligence and Humanized Computing*, *14*(4), 3369–3381. https://doi.org/10.1007/s12652-021-03474-5

Natural Resources Canada. (2025, December 20). *Lithium facts, Government of Canada*. https://natural-resources.canada.ca/our-natural-resources/minerals-mining/mining-data-statistics-and-analysis/minerals-metals-facts/lithium-facts/24009#L5

Ogorodova, L. P., Kiseleva, I. A., Melchakova, L. V., & Schuriga, T. N. (2005). Thermodynamic properties of lithium mica: Lepidolite. *Thermochimica Acta*, *435*(1), 68–70. https://doi.org/10.1016/j.tca.2005.04.026

Okubo, C. H. (2010). Structural geology of Amazonian-aged layered sedimentary deposits in southwest Candor Chasma, Mars. *Icarus*, *207*(1), 210–225. https://doi.org/10.1016/j.icarus.2009.11.012

Oliazadeh, M., Aghamirian, M., Ali, S., Legault, E., & Gibson, C. (2018). *Flowsheet Development for Benefication of Lithium Minerals from Hard Rock Deposits* (pp. 2293–2307). https://doi.org/10.1007/978-3-319-95022-8_192

Opoku, P. A., Tadesse, B., Albijanic, B., & Nikoloski, A. N. (2025). An overview of coarse particle beneficiation of lithium ores. *Scientific Reports*, *15*(1). https://doi.org/10.1038/s41598-025-14059-z

Ordóñez-Calderón, J. C., & Gelcich, S. (2018). Machine learning strategies for classification and prediction of alteration facies: Examples from the Rosemont Cu-Mo-Ag skarn deposit, SE Tucson Arizona. *Journal of Geochemical Exploration*, *194*, 167–188. https://doi.org/10.1016/j.gexplo.2018.07.020

Ouanan, H., & Abdelwahed, E. H. (2019, December 1). Image processing and machine learning applications in mining industry: Mine 4.0. *Proceedings - 2019 International Conference on Intelligent Systems and Advanced Computing Sciences, ISACS 2019*. https://doi.org/10.1109/ISACS48493.2019.9068884

Parmar, A., Katariya, R., & Patel, V. (2018). A Review on Random Forest: An Ensemble Classifier. In J. Hemanth, X. Fernando, P. Lafata, & Z. Baig (Eds.), *Lecture Notes on Data Engineering and Communications Technologies* (Vol. 26, pp. 758–763). Springer Cham. https://doi.org/10.1007/978-3-030-03146-6_86

Patriot Battery Metals. (2024). *PEA Highlights Shaakichiuwaanaan Project as a Potential North American Lithium Raw Materials Supply Base*.

Phillips, G. N., & Powell, R. (2010). Formation of gold deposits: A metamorphic devolatilization model. *Journal of Metamorphic Geology*, *28*(6), 689–718. https://doi.org/10.1111/j.1525-1314.2010.00887.x

Qazi, A., & Singh, K. (2023). Rock Mass Classification Techniques and Parameters: a Review. *Journal of Mining and Environment*, *14*(1), 155–178. https://doi.org/10.22044/jme.2023.12618.2292

Ralph, J., Von Bargen, D., Martynov, P., Zhang, J., Que, X., Prabhu, A., Morrison, S. M., Li, W., Chen, W., & Ma, X. (2025). Mindat.org: The open access mineralogy database to accelerate data-intensive geoscience research. *American Mineralogist*, *110*(6), 833–844. https://doi.org/10.2138/am-2024-9486

Robinson, D. (2024). *15 Biggest Environmental Problems of 2024*. Earth.Org. https://earth.org/the-biggest-environmental-problems-of-our-lifetime/

Rodriguez-Galiano, V., Sanchez-Castillo, M., Chica-Olmo, M., & Chica-Rivas, M. (2015). Machine learning predictive models for mineral prospectivity: An evaluation of neural networks, random forest, regression trees and support vector machines. *Ore Geology Reviews*, *71*, 804–818. https://doi.org/10.1016/j.oregeorev.2015.01.001

Sahoo, S. K., Tripathy, S. K., Nayak, A., Hembrom, K. C., Dey, S., Rath, R. K., & Mohanta, M. K. (2024). Beneficiation of lithium bearing pegmatite rock: a review. *Mineral Processing and Extractive Metallurgy Review*, *45*(1), 1–27. https://doi.org/10.1080/08827508.2022.2117172

Salakjani, N. K., Singh, P., & Nikoloski, A. N. (2016). Mineralogical transformations of spodumene concentrate from Greenbushes, Western Australia. Part 1: Conventional heating. *Minerals Engineering*, *98*, 71–79. https://doi.org/10.1016/j.mineng.2016.07.018

Scott, D. M., & McCann, H. (2005). *Process Imaging For Automatic Control* (D. M. Scott & H. McCann, Eds.; 1st ed.). Taylor and Francis.

Séguret, S. A., Guajardo Moreno, C., Seguret, S. A., & Guajardo, C. (2015, September 5). *Geostatistical Evaluation of Rock-Quality Designation and its link with Linear Fracture Frequency*. https://minesparis-psl.hal.science/hal-01187731v1

Sepro Mineral Systems Corp. (n.d.). *COARSE AND FINE PRECIOUS METAL RECOVERY*. www.seprosystems.com

Shi, F. (2016). Determination of ferrosilicon medium rheology and stability. *Minerals Engineering*, *98*, 60–70. https://doi.org/10.1016/j.mineng.2016.07.016

Skipp, G. L., & Brownfield, I. (1993). *Improved density gradient separation techniques using Sodium Polytungstate and a comparison to the use of other heavy liquids*.

Song, Q., Liu, X., & Yang, L. (2015). The Random Forest Classifier Applied In Droplet Fingerprint Recognition. In Z. Tang, J. Du, S. Yin, L. He, & R. Li (Eds.), *2015 12th International Conference on Fuzzy Systems and Knowledge Discovery (FSKD)* (pp. 722–726). IEEE.

Stempkowska, A. (2021). Characteristics of thermal parameters and some physical properties of mineral eutectic type: Petalite–alkali feldspars. *Materials*, *14*(23). https://doi.org/10.3390/ma14237321

Stringfellow, W. T., & Dobson, P. F. (2021). Technology for the recovery of lithium from geothermal brines. *Energies*, *14*(20). https://doi.org/10.3390/en14206805

Stuhlman, O. (1929). The thermophosphorescent radiations of hiddenite and kunzite. *Optical Society of America and Review of Scientific Instruments*, *18*(5).

Suyal, M., & Goyal, P. (2022). A Review on Analysis of K-Nearest Neighbor Classification Machine Learning Algorithms based on Supervised Learning. *International Journal of Engineering Trends and Technology*, *70*(7), 43–48. https://doi.org/10.14445/22315381/IJETT-V70I7P205

Svarovsky, L. (2001). *6 Hydrocyclones*.

Swain, B. (2016). Separation and purification of lithium by solvent extraction and supported liquid membrane, analysis of their mechanism: a review. *Journal of Chemical Technology and Biotechnology*, *91*(10), 2549–2562. https://doi.org/10.1002/jctb.4976

Swain, B. (2017). Recovery and recycling of lithium: A review. *Separation and Purification Technology*, *172*, 388–403. https://doi.org/10.1016/j.seppur.2016.08.031

Tadesse, B., Makuei, F., Albijanic, B., & Dyer, L. (2019). The beneficiation of lithium minerals from hard rock ores: A review. *Minerals Engineering*, *131*, 170–184. https://doi.org/10.1016/j.mineng.2018.11.023

Talens Peiró, L., Villalba Méndez, G., & Ayres, R. U. (2013). Lithium: Sources, production, uses, and recovery outlook. *JOM*, *65*(8), 986–996. https://doi.org/10.1007/s11837-013-0666-4

Ulusay, R. (2015). The ISRM Suggested Methods for Rock Characterization, Testing and Monitoring: 2007-2014. In R. Ulusay (Ed.), *The ISRM Suggested Methods for Rock Characterization, Testing and Monitoring: 2007-2014* (1st ed.). Springer Cham. https://doi.org/10.1007/978-3-319-07713-0

Viklund, A., & Aquilina, J. (2018). *LST Heavy Liquid - Technical Data*. https://www.heavyliquids.com/techdata.html

Viles, H., Goudie, A., Grab, S., & Lalley, J. (2011). The use of the Schmidt Hammer and Equotip for rock hardness assessment in geomorphology and heritage science: A comparative analysis. *Earth Surface Processes and Landforms*, *36*(3), 320–333. https://doi.org/10.1002/esp.2040

Waanders, F. B., & Mans, A. (2003). Characterisation of ferrosilicon dense medium separation material. *Hyperfine Interactions*, *148–149*(1), 325–329.

Wang, Y., & Fu-Shun, Y. U. (2007). Effects of Metallic Ions on the Flotation of Spodumene and Beryl. *Journal of China University of Mining & Technology*, *17*(1).

Wang, Y., Lin, C. L., & Miller, J. D. (2015). Improved 3D image segmentation for X-ray tomographic analysis of packed particle beds. *Minerals Engineering*, *83*, 185–191. https://doi.org/10.1016/j.mineng.2015.09.007

Wang, Y., Zhou, Y., & Yang, J. (2017). Structure and Optimization of a Two-Stage Equal-Density Dense Medium Cyclone. *Energy and Fuels*, *31*(7), 7662–7672. https://doi.org/10.1021/acs.energyfuels.7b00690

Welham, N. J. (2019a). CHAPTER 12.20 Lithium. In *Welham Metallurgical Services*. SME. http://ebookcentral.proquest.com/lib/ulaval/detail.action?docID=5649299.

Welham, N. J. (2019b). Lithium. In C. Young (Ed.), *SME mineral processing & extractive metallurgy handbook* (pp. 2019–2031). Society for Mining, Metallurgy & Exploration (SME). http://ebookcentral.proquest.com/lib/ulaval/detail.action?docID=5649299.

Wells, Martin., Aylmore, Mark., & McInnes, Brent. (2022). *The geology, mineralogy and geometallurgy of EV materials deposits in Western Australia*. Geological Survey of Western Australia.

Wills, B. A., & Finch, J. A. (2016a). Chapter 1 - Introduction. In B. A. Wills & J. A. Finch (Eds.), *Wills' Mineral Processing Technology* (8th ed., pp. 1–27). Butterworth-Heinemann. https://doi.org/https://doi.org/10.1016/B978-0-08-097053-0.00001-7

Wills, B. A., & Finch, J. A. (2016b). Chapter 4 - Particle Size Analysis. In *Wills' Mineral Processing Technology* (pp. 91–107). Butterworth-Heinemann.

Wills, B. A., & Finch, J. A. (2016c). Chapter 10 - Gravity Concentration. In B. A. Wills & J. A. Finch (Eds.), *Wills' Mineral Processing Technology* (8th ed., pp. 223–244). Butterworth-Heinemann. https://doi.org/10.1016/B978-0-08-097053-0.00010-8

Wills, B. A., & Finch, J. A. (2016d). Chapter 11 - Dense Medium Separation (DMS). In B. A. Wills & J. A. Finch (Eds.), *Wills' Mineral Processing Technology* (8th ed., pp. 245–264). Butterworth-Heinemann.

Xie, M., Liu, F., & Zhao, H. (2023). Study on phase transformation and lithium extraction of amblygonite using low temperature acid free roasting method. *Journal of Cleaner Production*, *421*. https://doi.org/10.1016/j.jclepro.2023.138547

Xie, Zhu, Y., Liu, J., Li, Y., Wang, X., & Shumin, Z. (2021). Research Status of Spodumene Flotation: A Review. *Mineral Processing and Extractive Metallurgy Review*, *42*(5), 321–334. https://doi.org/10.1080/08827508.2020.1776278

Yan, Q., Li, X., Wang, Z., Wu, X., Guo, H., Hu, Q., Peng, W., & Wang, J. (2012). Extraction of valuable metals from lepidolite. *Hydrometallurgy*, *117–118*, 116–118. https://doi.org/10.1016/j.hydromet.2012.02.004

Zhang, A. C., Wang, R. C., Jiang, S. Y., Hu, H., & Zhang, H. (2008). Chemical and textural features of tourmaline from the spodumene-subtype Koktokay No. 3 pegmatite, Altai, northwestern China: A record of magmatic to hydrothermal evolution. *Canadian Mineralogist*, *46*(1), 41–58. https://doi.org/10.3749/canmin.46.1.41

Zhang, L. (2016). Determination and applications of rock quality designation (RQD). *Journal of Rock Mechanics and Geotechnical Engineering*, *8*(3), 389–397. https://doi.org/10.1016/j.jrmge.2015.11.008

Zhou, H., Cao, Z., Ma, B., Wang, C., & Chen, Y. (2024). Selective and efficient extraction of lithium from spodumene via nitric acid pressure leaching. *Chemical Engineering Science*, *287*. https://doi.org/10.1016/j.ces.2024.119736

Zhou, Q., Ma, X., & Xiong, X. (2024). Extraction of lithium and phosphorus from amblygonite using calcium sulfate roasting and water leaching. *Hydrometallurgy*, *225*. https://doi.org/10.1016/j.hydromet.2024.106282

Zhu, T. (2020). Analysis on the applicability of the random forest. *Journal of Physics: Conference Series*, *1607*(1). https://doi.org/10.1088/1742-6596/1607/1/012123

Zuo, R. (2017). Machine Learning of Mineralization-Related Geochemical Anomalies: A Review of Potential Methods. *Natural Resources Research*, *26*(4), 457–464. https://doi.org/10.1007/s11053-017-9345-4

Zuo, R., & Xiong, Y. (2018). Big Data Analytics of Identifying Geochemical Anomalies Supported by Machine Learning Methods. *Natural Resources Research*, *27*(1), 5–13. https://doi.org/10.1007/s11053-017-9357-0

APPENDICES

APPENDIX A HLS Li Recovery data both models 1 and 2.

Table A.1 HLS LI Recovery data for Model 1 (all data).

SGS Sample ID	Actual Li recovery (%)		Spd >7mm	Ni Final ppm	W Final ppm	Co Final ppm	Th Final ppm	Spodumene %	Model 1, using all data	Error
Composite 1	92%	1	2.00	0.94	0.59	-0.39	0.65	35.26	90%	0.04%
Composite 2	83%	1	1.99	1.04	0.84	-0.29	0.24	15.00	83%	0.00%
Composite 3	90%	1	1.99	0.84	0.50	-0.50	0.36	9.36	89%	0.01%
Composite 4	87%	1	2.00	0.95	0.73	-0.30	0.24	12.58	86%	0.01%
Composite 5	91%	1	2.00	0.65	0.44	-0.56	0.47	22.80	92%	0.00%
Composite 6	61%	1	1.91	0.61	0.32	-0.46	0.57	11.20	61%	0.00%
Composite 7	81%	1	1.96	0.86	0.62	-0.56	0.35	11.44	82%	0.01%
Composite 8	86%	1	1.94	1.33	0.33	-0.26	0.64	14.61	84%	0.01%
Composite 9	93%	1	2.00	1.10	0.55	-0.45	0.84	21.94	94%	0.02%
Composite 10	79%	1	1.97	1.09	0.60	-0.21	0.48	12.51	80%	0.01%
Composite 11	92%	1	2.00	1.12	0.56	-0.10	0.16	27.80	93%	0.01%
		b_0	b_1	b_2	b_3	b_4	b_5	b_6	Sum	0.13%
		-5.07	2.85	0.31	-0.28	-0.33	-0.14	0.07		

Table A.2 HLS LI Recovery data for Model 2 (only logging data).

SGS Sample ID	Actual Li recovery (%)		Spd >7mm	Spd Alteration Intensity	Average Natural Fractures	Average Fracture Frequency	Average ISRM Rock Strength	Average RQD (Sum> 10 cm)	Model 2 only logging data	Error
Composite 1	92%	1.00	2.00	1.19	-0.70	0.00	0.60	0.47	90%	0.04%
Composite 2	83%	1.00	1.99	0.82	0.51	0.04	0.60	0.46	85%	0.06%
Composite 3	90%	1.00	1.99	0.16	0.36	-0.14	0.70	0.47	88%	0.05%
Composite 4	87%	1.00	2.00	1.00	0.73	0.26	0.60	0.47	85%	0.02%
Composite 5	91%	1.00	2.00	0.70	0.00	0.00	0.60	0.48	90%	0.02%
Composite 6	61%	1.00	1.91	0.68	0.36	-0.22	0.70	0.48	61%	0.00%
Composite 7	81%	1.00	1.96	0.35	0.65	0.08	0.60	0.46	79%	0.02%
Composite 8	86%	1.00	1.94	-0.58	-0.35	-0.65	0.48	0.48	85%	0.01%
Composite 9	93%	1.00	2.00	0.65	-0.22	-0.52	0.70	0.46	93%	0.01%
Composite 10	79%	1.00	1.97	0.70	0.00	0.00	0.60	0.47	82%	0.11%
Composite 11	92%	1.00	2.00	0.00	0.00	0.00	0.60	0.47	95%	0.06%
		b0	b1	b2	b3	b4	b5	b6	Sum	0.39%
		-4.51	2.97	-0.06	-0.03	-0.05	-0.13	-0.84		

APPENDIX B Raw data of particle size distribution (first grinding test)

Table B.1 Raw data of particle size distribution for liberated spoduemene sample.

Liberated Spodumene			
Total mass (g)	Mass of cup (g)	Mesh (µm)	Cumulative Grams (g)
104.71	6.61	10000	0
		9500	1.44
		6300	21.16
		3300	71.51
		1700	86.48
		630	92.91
		-630	97.91

Table B.2 Raw data of particle size distribution for mixed spoduemene sample.

Mixed Spodumene			
Total mass (g)	Mass of cup (g)	Mesh (µm)	Cumulative Grams (g)
105.01	6.95	10000	0
		9500	0
		6300	15.9
		3300	61.6
		1700	81.01
		630	90.7
		-630	98.09

Table B.3 Raw data of particle size distribution for mixed quartz sample.

Mixed Quartz			
Total mass (g)	Mass of cup (g)	Mesh (µm)	Cumulative Grams (g)
105.07	6.63	10000	0
		9500	0
		6300	9.87
		3300	59.72
		1700	81.3
		630	90.7
		-630	98.28

Table B.4 Raw data of particle size distribution for liberated quartz sample.

Liberated Quartz			
Total mass (g)	Mass of cup (g)	Mesh (µm)	Cumulative Grams (g)
103.11	6.77	10000	0
		9500	0.99
		6300	12.44
		3300	63.71
		1700	82.28
		630	90.36
		-630	96.34

APPENDIX C Sieve data after hls tests (raw data, sieve fractions are in grams)

Table C.1 Sieve data after HLS tests (raw data, sieve fractions are in grams)

Sample	Fraction	Density (g/cm3)	Mass g (sample + bag)	Mass bag (g)	Sieve sizes (mm)					
					-9.50	-6.30	-3.35	-1.70	-0.63	+0.63
Liberated Spodumene	Sink	3.00	15.22	1.24	1.4	4.57	5.37	1.93	0.62	0.09
	Sink	2.85	7.63	1.22	0	0.5	4.94	0.8	0.18	0.01
	Sink	2.70	2.66	1.25	0	0	1.01	0.31	0.06	0.03
	Float	2.70	26.73	1.24	0	5.08	14.54	4.05	1.41	0.39
Mixed Spodumene	Sink	3.00	11.06	1.22	0	1.09	4.42	2.72	1.28	0.31
	Sink	2.85	11.22	1.23	1.69	0.97	5.11	1.72	0.52	0.04
	Sink	2.70	1.91	1.23	0	0	0.41	0.15	0.13	0.02
	Float	2.70	25.58	1.25	0	4.02	12.55	5.31	2.1	0.47
Mixed quartz	Sink	3.00	6.52	1.23	0	0	3.43	1.23	0.49	0.1
	Sink	2.85	8.77	1.22	0	0	5.39	1.73	0.36	0.05
	Sink	2.70	3.77	1.22	0	0	1.66	0.6	0.23	0.02
	Float	2.70	32.16	1.26	0	2.76	17.6	7.59	2.5	0.39
Liberated Quartz	Sink	3.00	5.91	1.23	0	1.51	1.92	0.63	0.53	0.04
	Sink	2.85	7.31	1.27	0	1.78	2.76	1.1	0.4	0.07
	Sink	2.70	4.13	1.25	0	0.23	2.16	0.34	0.12	0.02
	Float	2.70	37.89	1.27	0	4.07	20.38	8.24	2.9	0.97

APPENDIX D ICP chemistry results for all samples.

Table D.1 ICP chemistry results of liberated spodumene sample. Concentrations are in µg/g.

Name of the sample	Li	Ag	Al	As	Ba	Be	Bi	Ca	Cd	Ce	Co	Cr	Cs	Cu	Dy	Er	Eu	Fe	Ga	Gd	Ge	Hf	Ho	In	K	La	Lu
Centrifuge_float_-0.63mm	490	< 0.5	45000	21	14	58	8	990	0.05	0.59	2.8	67	420	20	0.16	0.036	0.02	20000	35	0.2	< 0.3	2.1	0.02	0.04	18000	0.26	0.008
Centrifuge_sinkt_-0.63mm	14000	< 0.5	92000	163	34	40	35	5000	0.74	6.41	36	2100	1200	155	2.44	0.42	0.13	66000	92	2.79	1	11	0.22	0.22	7600	3.02	0.055
LS_sink_3.0_+9.5mm	23000	< 0.5	99000	31	2	3.1	1.3	250	0.08	0.49	32	1400	350	152	0.22	0.061	0.006	58000	95	0.17	0.6	3.1	0.026	0.07	600	0.25	0.29
LS_sink_3.0_+6.3mm	27000	< 0.5	100000	51	3	2.8	< 0.09	260	0.05	0.14	4.1	180	1500	22	0.018	0.008	0.002	38000	120	0.02	0.6	0.4	0.002	0.08	930	0.075	0.004
LS_sink_3.0_+3.35mm	26000	< 0.5	100000	41	11	2.8	0.12	370	0.11	0.16	2.3	56	1800	20	0.018	0.006	0.006	37000	130	0.024	0.6	0.4	0.002	0.11	1300	0.082	0.004
LS_sink_3.0_+1.7mm	23000	< 0.5	96000	35	24	48	0.1	1000	0.26	1.15	43	2500	2200	188	0.19	0.052	0.022	92000	110	0.21	1.5	0.7	0.024	0.16	1800	0.62	0.008
LS_sink_3.0_+0.63mm	21000	< 0.5	93000	36	15	2.9	0.55	8700	0.45	3.84	14	610	1300	88	2.39	0.34	0.071	120000	97	2.39	1.6	2.2	0.18	0.19	1700	1.67	0.2
LS_sink_2.85_+9.5mm																											
LS_sink_2.85_+6.3mm	11000	< 0.5	93000	9	120	17	0.66	700	0.2	0.8	8.9	420	430	59	0.13	0.053	0.03	80000	83	0.12	1	1.3	0.018	0.24	20000	0.45	0.16
LS_sink_2.85_+3.35mm	15000	< 0.5	77000	13	64	16	0.87	1500	0.19	0.31	1.4	36	25000	12	0.28	0.042	0.016	19000	90	0.27	< 0.3	2.8	0.022	0.14	9000	0.13	0.006
LS_sink_2.85_+1.7mm	15000	< 0.5	86000	16	91	20	0.2	1700	0.28	1.02	9.6	610	1300	61	0.76	0.1	0.033	76000	89	0.74	1.2	1.7	0.057	0.21	12000	0.49	0.098
LS_sink_2.85_+0.63mm																											
LS_sink_2.7_+9.5mm																											
LS_sink_2.7_+6.3mm																											
LS_sink_2.7_+3.35mm	5900	< 0.5	55000	13	110	11	2.6	980	0.14	0.69	6.7	340	740	54	0.15	0.041	0.039	51000	79	0.17	0.7	0.9	0.016	0.34	19000	0.34	0.065
LS_sink_2.7_+1.7mm																											
LS_sink_2.7_+0.63mm																											
LS_float_2.7_+9.5mm																											
LS_float_2.7_+6.3mm	90	< 0.5	81000	12	13	8.6	9	1100	0.16	1.1	1.9	68	380	15	0.47	0.073	0.02	15000	44	0.67	< 0.3	4.2	0.037	0.02	27000	0.43	0.008
LS_float_2.7_+3.35mm	260	< 0.5	71000	11	39	24	3.2	1000	0.06	0.37	0.92	35	540	7.6	0.19	0.02	0.016	7400	42	0.22	< 0.3	1.4	0.012	0.03	31000	0.16	0.006
LS_float_2.7_+1.7mm	130	< 0.5	68000	14	19	35	2.2	920	0.05	0.44	1.1	26	590	17	0.26	0.037	0.016	15000	39	0.3	< 0.3	2.1	0.024	0.02	35000	0.2	0.03
LS_float_2.7_+0.63mm	220	< 0.5	68000	24	14	49	1.8	1000	0.08	0.78	25	1500	440	137	0.2	0.036	0.016	37000	40	0.26	0.5	2.8	0.02	0.04	25000	0.39	0.01

Table D.2 ICP chemistry results of liberated spodumene sample. Concentrations are in µg/g (continued).

Name of the sample	Mn	Mo	Nb	Nd	Ni	Pb	Pr	Ru	Re	Sc	Sb	Se	Sm	Sn	Sr	Ta	Tb	Te	Ti	Tl	Tm	U	V	Y	Yb	Zn	Zr
Centrifuge_float_-0.63mm	240	4.5	6.7	0.29	120	6	0.11	< 0.01	< 0.05	0.35	4.4	< 0.1	0.16	9	8	26.4	0.047	0.1	49	17	0.016	3.07	8.4	0.5	0.041	33	11
Centrifuge_sinkt_-0.63mm	3100	120	315	3.3	3500	8	0.78	< 0.01	< 0.05	3	10	< 0.1	2.13	50	13	640	0.69	0.1	360	7.5	0.067	9.66	29	7.58	0.46	280	51
LS_sink_3.0_+9.5mm	1600	120	33.8	0.21	3500	2	0.063	< 0.01	< 0.05	0.35	11	< 0.1	0.11	16	0.69	65	0.057	< 0.1	34	0.91	0.02	1.84	21	0.74	0.061	110	11
LS_sink_3.0_+6.3mm	1200	8.5	3.9	0.054	210	2	0.018	< 0.01	< 0.05	4	15	< 0.1	0.018	14	1	16.4	0.012	< 0.1	26	1.5	0.008	0.43	13	0.043	0.012	20	1
LS_sink_3.0_+3.35mm	1000	2.9	6.8	0.06	17	2	0.02	< 0.01	< 0.05	5	12	< 0.1	0.018	23	5	12.4	0.012	< 0.1	26	1.3	0.01	0.37	13	0.047	0.01	29	0.98
LS_sink_3.0_+1.7mm	2000	170	7.4	0.46	4700	2	0.14	< 0.01	< 0.05	3	10	< 0.1	0.17	39	12	22.5	0.06	< 0.1	70	1.6	0.018	0.53	30	0.67	0.052	50	4
LS_sink_3.0_+0.63mm	1600	31	117	1.6	870	5	0.48	< 0.01	< 0.05	3	23	< 0.1	1.8	43	11	437	0.71	< 0.1	53	1.5	0.053	2.49	32	7.73	0.28	82	8
LS_sink_2.85_+9.5mm																											
LS_sink_2.85_+6.3mm	2000	17	9.5	0.34	470	3	0.1	< 0.01	0.05	0.82	3.6	< 0.1	0.1	64	6	25.6	0.034	< 0.1	66	11	0.016	1.31	23	0.48	0.052	230	8
LS_sink_2.85_+3.35mm	1400	2	215	0.16	11	3	0.04	< 0.01	< 0.05	2	5.9	< 0.1	0.19	33	27	206	0.081	< 0.1	42	9.3	0.016	1.91	8.4	0.45	0.046	47	10
LS_sink_2.85_+1.7mm	1400	21	14.2	0.48	580	4	0.13	< 0.01	< 0.05	2	4.3	< 0.1	0.49	51	34	28.2	0.21	< 0.1	48	11	0.024	0.86	25	1.3	0.11	170	6
LS_sink_2.85_+0.63mm																											
LS_sink_2.7_+9.5mm																											
LS_sink_2.7_+6.3mm																											
LS_sink_2.7_+3.35mm	860	15	26.1	0.3	410	5	0.083	< 0.01	< 0.05	2	3.5	< 0.1	0.14	82	79	20.8	0.049	0.1	52	15	0.016	1.98	17	0.14	0.055	180	4
LS_sink_2.7_+1.7mm																											
LS_sink_2.7_+0.63mm																											
LS_float_2.7_+9.5mm																											
LS_float_2.7_+6.3mm	190	4.1	34.7	0.53	100	7	0.14	< 0.01	< 0.05	< 0.03	5.4	< 0.1	0.49	< 6	9	56.2	0.16	< 0.1	7.4	26	0.02	5.43	5.1	1.55	0.071	60	23
LS_float_2.7_+3.35mm	220	1.9	37.1	0.18	43	8	0.046	< 0.01	< 0.05	0.04	5.6	< 0.1	0.17	< 6	15	54.9	0.062	< 0.1	5.3	30	0.012	4.82	3	0.4	0.024	9.2	6
LS_float_2.7_+1.7mm	170	1.6	46.1	0.23	11	9	0.069	< 0.01	< 0.05	0.11	6.1	< 0.1	0.23	< 6	13	74.6	0.087	< 0.1	7.5	38	0.02	4.35	4.7	0.61	0.037	30	8
LS_float_2.7_+0.63mm	660	100	11.6	0.33	2800	8	0.092	< 0.01	< 0.05	0.1	6.7	< 0.1	0.2	7	10	20.9	0.072	< 0.1	23	24	0.018	3.51	15	0.52	0.05	63	13

Table D.3 ICP chemistry results of mixed spodumene sample. Concentrations are in µg/g (continued).

Name of the sample	Li	Ag	Al	As	Ba	Be	Bi	Ca	Cd	Ce	Co	Cr	Cs	Cu	Dy	Er	Eu	Fe	Ga	Gd	Ge	Hf	Ho	In	K	La	Lu
MS_sinkt_3.0_+9.5mm																											
MS_sink_3.0_+6.3mm	21000	< 0.5	95000	59	11	9.6	0.95	410	0.03	0.32	4.4	110	1500	61	0.044	0.018	0.008	62000	130	0.078	1	0.7	0.008	0.15	3300	0.17	0.006
MS_sink_3.0_+3.35mm	26000	< 0.5	99000	25	6	3.2	0.14	1100	0.17	0.28	1.8	44	1500	22	0.44	0.04	0.006	25000	120	0.5	0.4	0.6	0.03	0.13	1400	0.12	0.004
MS_sink_3.0_+1.7mm	24000	< 0.5	98000	35	5	2.8	2.5	2500	0.71	0.52	3.3	130	2000	26	0.43	0.066	0.008	30000	120	0.39	0.5	0.3	0.034	0.11	1600	0.22	0.012
MS_sink_3.0_+0.63mm	22000	< 0.5	100000	45	8	4	2.6	3600	0.75	1.39	33	3100	1400	149	0.77	0.1	0.022	63000	110	0.93	1.1	0.4	0.061	0.13	1700	0.7	0.012
MS_sink_2.85_+9.5mm	28000	< 0.5	91000	13	5	3.8	0.74	540	0.08	0.15	27	1300	1700	124	0.045	0.013	0.003	46000	105	0.028	0.8	2.5	0.004	0.14	4000	0.066	< 0.001
MS_sink_2.85_+6.3mm	13000	< 0.5	95000	21	19	7.2	0.97	1800	0.44	1.43	5.9	160	1300	63	1.22	0.15	0.03	88000	110	1.36	1.8	0.6	0.091	0.21	4000	0.63	0.032
MS_sink_2.85_+3.35mm	15000	< 0.5	54000	26	20	1600	1.6	1500	0.38	0.2	2.2	75	2500	18	0.17	0.028	0.008	21000	82	0.18	0.7	0.8	0.016	0.12	5200	0.091	0.006
MS_sink_2.85_+1.7mm	13000	< 0.5	78000	39	38	330	13	2700	0.34	0.93	4.3	150	3700	33	0.53	0.1	0.024	38000	99	0.5	1	1.1	0.048	0.2	11000	0.43	0.016
MS_sink_2.85_+0.63mm	11000	< 0.5	60000	15	23	180	3.4	770	0.21	0.32	11	520	5600	92	0.23	0.046	0.012	86000	90	0.2	1.8	1.3	0.02	0.33	14000	0.16	0.008
MS_sink_2.7_+9.5mm																											
MS_sink_2.7_+6.3mm																											
MS_sink_2.7_+3.35mm																											
MS_sink_2.7_+1.7mm																											
MS_sink_2.7_+0.63mm																											
MS_float_2.7_+9.5mm																											
MS_float_2.7_+6.3mm	300	< 0.5	61000	10	12	220	59	770	0.06	0.47	2.4	120	480	20	0.14	0.022	0.01	19000	44	0.18	0.9	1.8	0.012	0.04	20000	0.25	0.016
MS_float_2.7_+3.35mm	370	< 0.5	55000	9.6	10	59	12	1200	0.2	0.49	1.2	42	360	11	0.25	0.044	0.016	10000	43	0.29	0.5	4.3	0.022	0.04	16000	0.22	0.008
MS_float_2.7_+1.7mm	340	< 0.5	57000	7.8	9	110	124	840	0.12	0.57	1.4	31	270	12	0.22	0.03	0.014	18000	36	0.28	0.6	2.3	0.018	0.02	14000	0.25	0.006
MS_float_2.7_+0.63mm	300	< 0.5	46000	12	10	27	15	820	0.15	0.52	17	910	220	83	0.17	0.034	0.012	29000	33	0.17	0.7	4.8	0.018	0.03	11000	0.25	0.016

Table D.4 ICP chemistry results of mixed spodumene sample. Concentrations are in µg/g (continued).

Name of the sample	Mn	Mo	Nb	Nd	Ni	Pb	Pr	Ru	Re	Sc	Sb	Se	Sm	Sn	Sr	Ta	Tb	Te	Ti	Tl	Tm	U	V	Y	Yb	Zn	Zr
MS_sinkt_3.0_+9.5mm																											
MS_sink_3.0_+6.3mm	1500	6.3	5.7	0.15	36	1	0.042	< 0.01	< 0.05	2	7.3	< 0.1	0.06	31	8	19.2	0.024	< 0.1	60	6	0.014	0.51	26	0.085	0.022	93	2
MS_sink_3.0_+3.35mm	1200	2.8	4.1	0.15	16	2	0.042	< 0.01	< 0.05	3	9.5	< 0.1	0.28	31	5	20.1	0.15	< 0.1	28	2	0.012	0.58	11	0.67	0.028	24	0.79
MS_sink_3.0_+1.7mm	1500	6.5	19.5	0.21	130	2	0.062	< 0.01	< 0.05	3	11	< 0.1	0.3	25	4	57	0.12	< 0.1	35	2.6	0.022	0.9	14	0.86	0.091	51	0.83
MS_sink_3.0_+0.63mm	2100	130	13.2	0.56	3600	3	0.17	< 0.01	< 0.05	3	11	< 0.1	0.67	33	7	44.6	0.25	< 0.1	51	2	0.028	1.8	24	2.58	0.11	110	8
MS_sink_2.85_+9.5mm	1600	103	8.5	0.068	2900	2	0.019	< 0.01	< 0.05	3	6.4	< 0.1	0.018	36	4	21.8	0.008	< 0.1	36	5.2	0.002	0.64	17	0.1	0.013	97	10
MS_sink_2.85_+6.3mm	2100	8.4	22.2	0.74	61	4	0.21	< 0.01	< 0.05	2	6.3	< 0.1	0.94	50	22	67.9	0.38	< 0.1	290	6.7	0.036	3.86	35	3.07	0.11	820	3
MS_sink_2.85_+3.35mm	1100	4.3	53.9	0.1	77	5	0.026	< 0.01	< 0.05	1	7.8	< 0.1	0.12	31	8	119	0.051	< 0.1	30	5.3	0.012	2.09	9.6	0.49	0.032	70	3
MS_sink_2.85_+1.7mm	1200	9.2	42.6	0.39	200	6	0.11	< 0.01	< 0.05	2	13	< 0.1	0.42	46	11	117	0.14	< 0.1	58	9.7	0.032	5.09	15	1.02	0.13	100	4
MS_sink_2.85_+0.63mm	2500	24	41.8	0.17	630	6	0.046	< 0.01	< 0.05	2	6.3	< 0.1	0.12	76	7	130	0.062	< 0.1	86	15	0.016	2.4	28	0.36	0.052	120	5
MS_sink_2.7_+9.5mm																											
MS_sink_2.7_+6.3mm																											
MS_sink_2.7_+3.35mm																											
MS_sink_2.7_+1.7mm																											
MS_sink_2.7_+0.63mm																											
MS_float_2.7_+9.5mm																											
MS_float_2.7_+6.3mm	230	5.2	38.2	0.2	130	6	0.059	< 0.01	< 0.05	< 0.03	4.8	< 0.1	0.13	9	8	52.9	0.051	< 0.1	14	20	0.012	12	6.1	0.35	0.022	19	7
MS_float_2.7_+3.35mm	320	2.4	64.7	0.25	46	7	0.066	< 0.01	< 0.05	0.17	5.7	< 0.1	0.23	8	7	108	0.082	< 0.1	13	16	0.018	6.72	4.2	0.57	0.05	19	17
MS_float_2.7_+1.7mm	260	2.1	42.7	0.27	13	25	0.075	< 0.01	< 0.05	0.07	11	< 0.1	0.23	< 6	7	51.9	0.073	< 0.1	9.1	11	0.016	6.95	7.3	0.47	0.04	17	11
MS_float_2.7_+0.63mm	500	68	35.1	0.23	1900	8	0.067	< 0.01	< 0.05	0.04	4.6	< 0.1	0.14	7	6	39.5	0.052	< 0.1	19	9.5	0.014	2.37	11	0.43	0.04	21	23

Table D.5 ICP chemistry results of mixed quartz sample. Concentrations are in µg/g (continued).

Name of the sample	Li	Ag	Al	As	Ba	Be	Bi	Ca	Cd	Ce	Co	Cr	Cs	Cu	Dy	Er	Eu	Fe	Ga	Gd	Ge	Hf	Ho	In	K	La	Lu
MQ_sink_3.0_+9.5mm																											
MQ_sink_3.0_+6.3mm																											
MQ_sink_3.0_+3.35mm	25000	< 0.5	97000	50	2	3.5	1.8	370	0.03	0.23	2.8	88	1300	18	0.062	0.016	0.004	30000	120	0.066	0.6	1.6	0.006	0.12	1700	0.12	0.004
MQ_sink_3.0_+1.7mm	24000	< 0.5	97000	39	7	3.6	0.23	490	0.04	0.38	5.1	200	1400	43	0.068	0.022	0.008	46000	110	0.078	1	0.8	0.008	0.13	1600	0.2	0.004
MQ_sink_3.0_+0.63mm																											
MQ_sink_2.85_+9.5mm																											
MQ_sink_2.85_+6.3mm																											
MQ_sink_2.85_+3.35mm	16000	< 0.5	83000	14	23	14	8.6	660	0.11	0.26	2.5	100	860	23	0.1	0.018	0.01	23000	110	0.12	0.7	1.1	0.01	0.21	9800	0.13	0.004
MQ_sink_2.85_+1.7mm	14000	< 0.5	76000	13	28	17	14	3900	0.68	1.34	2.7	59	1000	35	1.66	0.17	0.028	36000	95	1.66	0.7	4.4	0.11	0.26	10000	0.54	0.016
MQ_sink_2.85_+0.63mm																											
MQ_sink_2.7_+9.5mm																											
MQ_sink_2.7_+6.3mm																											
MQ_sink_2.7_+3.35mm	3000	< 0.5	30000	17	16	810	20	640	0.09	0.22	5	220	910	67	0.2	0.035	0.008	41000	62	0.21	1	9	0.018	0.2	14000	0.087	0.01
MQ_sink_2.7_+1.7mm	3000	< 0.5	23000	12	9	1600	97	350	0.18	0.17	6.1	130	670	82	0.32	0.1	0.01	86000	45	0.1	2.1	8.7	0.044	0.13	5400	0.079	0.034
MQ_sink_2.7_+0.63mm																											
MQ_float_2.7_+9.5mm																											
MQ_float_2.7_+6.3mm	93	< 0.5	29000	9.2	3	1.7	13	310	0.03	0.68	4.3	180	77	44	0.11	0.024	0.011	39000	16	0.13	0.6	1	0.011	0.02	3600	0.24	< 0.001
MQ_float_2.7_+3.35mm	370	< 0.5	39000	7	20	12	9.7	550	0.09	0.23	1.2	43	220	13	0.12	0.027	0.013	14000	24	0.18	0.3	4.6	0.013	0.03	12000	0.1	< 0.001
MQ_float_2.7_+1.7mm	300	< 0.5	37000	8.7	9	50	5.6	600	0.08	0.29	9.9	2000	150	49	0.15	0.025	0.007	18000	22	0.24	< 0.3	4.3	0.013	0.02	7800	0.13	< 0.001
MQ_float_2.7_+0.63mm	210	< 0.5	32000	7.9	9	6.1	2.6	450	0.06	0.74	4.6	160	120	52	0.22	0.041	0.009	41000	17	0.23	0.8	3.5	0.018	0.02	6500	0.33	< 0.001

Table D.6 ICP chemistry results of mixed quartz sample. Concentrations are in µg/g (continued).

Name of the sample	Mn	Mo	Nb	Nd	Ni	Pb	Pr	Ru	Re	Sc	Sb	Se	Sm	Sn	Sr	Ta	Tb	Te	Ti	Tl	Tm	U	V	Y	Yb	Zn	Zr
MQ_sink_3.0_+9.5mm																											
MQ_sink_3.0_+6.3mm																											
MQ_sink_3.0_+3.35mm	1200	5.2	6.7	0.098	97	2	0.03	< 0.01	< 0.05	1	10	< 0.1	0.046	27	1	16.1	0.022	< 0.1	56	3	0.012	4.42	12	0.086	0.016	73	4
MQ_sink_3.0_+1.7mm	1200	10	9.1	0.17	200	4	0.064	< 0.01	< 0.05	3	10	< 0.1	0.068	22	3	48.9	0.026	< 0.1	37	2	0.012	2.19	20	0.12	0.024	160	2
MQ_sink_3.0_+0.63mm																											
MQ_sink_2.85_+9.5mm																											
MQ_sink_2.85_+6.3mm																											
MQ_sink_2.85_+3.35mm	1100	4.8	40.1	0.1	93	3	0.03	< 0.01	< 0.05	1	5.5	< 0.1	0.099	51	8	70.3	0.034	< 0.1	61	8.4	0.01	2.42	10	0.11	0.02	93	4
MQ_sink_2.85_+1.7mm	1800	4.1	128	0.64	25	7	0.18	< 0.01	< 0.05	2	6.8	< 0.1	0.94	58	14	288	0.49	< 0.1	61	10	0.03	2.96	16	3.49	0.13	150	15
MQ_sink_2.85_+0.63mm																											
MQ_sink_2.7_+9.5mm																											
MQ_sink_2.7_+6.3mm																											
MQ_sink_2.7_+3.35mm	1200	11	74.2	0.12	250	7	0.033	< 0.01	< 0.05	0.68	8.9	< 0.1	0.13	49	8	109	0.059	< 0.1	90	15	0.014	6.15	15	0.5	0.049	240	42
MQ_sink_2.7_+1.7mm	2000	8.7	16.5	0.075	57	6	0.028	< 0.01	< 0.05	1	7	< 0.1	0.067	26	3	23	0.056	< 0.1	66	5.5	0.03	2.19	31	1.16	0.15	150	43
MQ_sink_2.7_+0.63mm																											
MQ_float_2.7_+9.5mm																											
MQ_float_2.7_+6.3mm	330	7.9	31.5	0.45	170	3	0.099	< 0.01	< 0.05	0.06	7.6	< 0.1	0.14	< 6	2	32	0.024	< 0.1	13	3.5	0.006	10.9	16	0.44	0.037	15	6
MQ_float_2.7_+3.35mm	200	1.7	50.1	0.13	9.8	6	0.034	< 0.01	< 0.05	0.28	6	< 0.1	0.14	< 6	10	77.6	0.044	< 0.1	9	11	0.006	5.7	7.2	0.31	0.028	15	22
MQ_float_2.7_+1.7mm	360	39	67.7	0.15	1100	6	0.038	0.01	< 0.05	0.11	5.7	< 0.1	0.18	< 6	4	80	0.056	< 0.1	10	7.1	0.006	9.42	7.1	0.38	0.032	15	22
MQ_float_2.7_+0.63mm	380	8.9	28.6	0.31	190	5	0.086	< 0.01	< 0.05	0.06	4.7	< 0.1	0.23	< 6	5	45.2	0.054	0.1	11	5.8	0.006	4.55	16	0.76	0.056	27	19

Table D.7 ICP chemistry results of liberated quartz sample. Concentrations are in µg/g (continued).

Name of the sample	Li	Ag	Al	As	Ba	Be	Bi	Ca	Cd	Ce	Co	Cr	Cs	Cu	Dy	Er	Eu	Fe	Ga	Gd	Ge	Hf	Ho	In	K	La	Lu
LQ_sink_3.0_+9.5mm																											
LQ_sink_3.0_+6.3mm	33000	< 0.5	96000	51	8	3.5	0.1	250	0.05	0.059	4.8	190	1500	32	0.017	0.012	0.004	43000	105	0.008	0.6	0.5	0.002	0.08	1000	0.028	< 0.001
LQ_sink_3.0_+3.35mm	11000	< 0.5	87000	24	6	4.7	2.1	940	0.05	0.14	6.3	240	370	40	0.07	0.012	0.008	70000	130	0.11	1.1	0.6	0.006	0.09	1100	0.054	< 0.001
LQ_sink_3.0_+1.7mm	9100	< 0.5	84000	14	2	5.1	20	2800	0.93	0.56	6.3	93	510	69	0.38	0.058	0.019	94000	123	0.44	1.4	1	0.029	0.11	2000	0.21	< 0.001
LQ_sink_3.0_+0.63mm																											
LQ_sink_2.85_+9.5mm																											
LQ_sink_2.85_+6.3mm																											
LQ_sink_2.85_+3.35mm	13000	2.1	90000	50	160	22	2380	1300	0.16	0.31	1.7	35	2000	23	0.18	0.026	0.037	24000	143	0.23	0.5	2.2	0.014	0.47	31000	0.13	< 0.001
LQ_sink_2.85_+1.7mm	7500	0.5	91000	86	270	140	582	2200	0.26	1.06	15	1300	2800	80	0.25	0.054	0.077	34000	165	0.41	0.7	15	0.025	2	33000	0.47	< 0.001
LQ_sink_2.85_+0.63mm	6800	1.8	71000	91	49	209	1848	1000	0.14	0.54	8.7	370	2700	89	0.3	0.059	0.026	75000	123	0.35	1.5	3.1	0.028	0.66	30000	0.24	< 0.001
LQ_sink_2.7_+9.5mm																											
LQ_sink_2.7_+6.3mm																											
LQ_sink_2.7_+3.35mm	3600	< 0.5	70000	87	200	42	86	6200	0.17	6.5	5.2	29	2700	35	0.37	0.15	0.2	23000	91	0.98	0.5	2.7	0.058	0.41	29000	2.88	< 0.001
LQ_sink_2.7_+1.7mm																											
LQ_sink_2.7_+0.63mm																											
LQ_float_2.7_+9.5mm																											
LQ_float_2.7_+6.3mm	1500	< 0.5	38000	9.3	5	26	34	270	0.04	0.11	3.1	260	310	28	0.034	0.013	0.004	28000	40	0.046	0.5	3.5	0.003	0.14	7500	0.052	< 0.001
LQ_float_2.7_+3.35mm	610	< 0.5	20000	16	11	98	27	770	0.09	1.04	12	890	310	51	0.39	0.059	0.026	21000	15	0.5	0.4	2.3	0.033	0.04	4400	0.42	< 0.001
LQ_float_2.7_+1.7mm	350	< 0.5	21000	8.5	6	48	86	950	0.05	1.14	2.1	40	150	15	0.34	0.043	0.03	24000	13	0.53	0.4	1.9	0.022	0.02	2800	0.44	< 0.001
LQ_float_2.7_+0.63mm	390	< 0.5	21000	10	8	5.3	46	810	0.09	0.81	4.1	130	120	29	0.25	0.046	0.02	39000	13	0.37	0.7	2.6	0.021	0.03	2900	0.32	< 0.001

Table D.8 ICP chemistry results of liberated quartz sample. Concentrations are in µg/g (continued).

Name of the sample	Mn	Mo	Nb	Nd	Ni	Pb	Pr	Ru	Re	Sc	Sb	Se	Sm	Sn	Sr	Ta	Tb	Te	Ti	Tl	Tm	U	V	Y	Yb	Zn	Zr
LQ_sink_3.0_+9.5mm																											
LQ_sink_3.0_+6.3mm	1500	9.1	2.3	0.029	180	1	0.006	< 0.01	< 0.05	2	21	< 0.1	0.018	17	2	13.1	0.002	< 0.1	22	0.97	0.002	0.63	20	0.047	0.008	78	2
LQ_sink_3.0_+3.35mm	2300	9.9	4.4	0.09	240	3	0.02	< 0.01	< 0.05	0.94	7.1	< 0.1	0.084	24	7	16.9	0.02	< 0.1	590	0.77	0.002	5.36	18	0.17	0.013	1700	3
LQ_sink_3.0_+1.7mm	2300	6.2	7.1	0.3	39	4	0.077	< 0.01	< 0.05	1	6.3	< 0.1	0.34	24	3	5	0.11	< 0.1	610	1.4	0.01	3.42	27	0.78	0.064	1600	3
LQ_sink_3.0_+0.63mm																											
LQ_sink_2.85_+9.5mm																											
LQ_sink_2.85_+6.3mm																											
LQ_sink_2.85_+3.35mm	2000	2.1	67.8	0.16	13	5	0.04	< 0.01	< 0.05	3	80	0.1	0.16	111	7	154	0.051	2.1	190	29	0.004	7.48	9.6	0.36	0.034	330	7
LQ_sink_2.85_+1.7mm	3100	56	188	0.42	1600	6	0.13	< 0.01	< 0.05	4	27	< 0.1	0.39	379	7	1277	0.087	0.6	310	43	0.01	13.2	12	0.5	0.085	470	32
LQ_sink_2.85_+0.63mm	2300	15	273	0.28	340	9	0.08	< 0.01	< 0.05	3	63	0.1	0.27	155	6	957	0.093	1.5	280	29	0.01	5.26	33	0.6	0.064	340	12
LQ_sink_2.7_+9.5mm																											
LQ_sink_2.7_+6.3mm																											
LQ_sink_2.7_+3.35mm	1200	1.4	93	3.1	20	10	0.79	< 0.01	< 0.05	4	19	< 0.1	1.11	100	81	144	0.12	0.2	1100	33	0.032	12.6	25	1.04	0.15	170	48
LQ_sink_2.7_+1.7mm																											
LQ_sink_2.7_+0.63mm																											
LQ_float_2.7_+9.5mm																											
LQ_float_2.7_+6.3mm	590	5.6	96	0.079	110	3	0.021	< 0.01	< 0.05	0.44	8.1	< 0.1	0.038	36	3	130	0.01	0.1	43	7.1	0.004	5.92	14	0.11	0.016	71	17
LQ_float_2.7_+3.35mm	540	45	43.9	0.48	1300	3	0.13	< 0.01	< 0.05	0.28	8.8	< 0.1	0.36	9	7	31.5	0.11	< 0.1	37	3.5	0.01	4.14	7.4	1.31	0.056	25	14
LQ_float_2.7_+1.7mm	280	2.9	7.8	0.51	16	3	0.14	< 0.01	< 0.05	0.11	9.3	< 0.1	0.46	< 6	8	9	0.1	< 0.1	28	2.3	0.008	3.36	11	0.76	0.044	35	11
LQ_float_2.7_+0.63mm	400	7.3	13.2	0.39	150	5	0.11	< 0.01	< 0.05	0.11	7	< 0.1	0.33	6	7	23.8	0.078	< 0.1	22	2.5	0.01	3.56	16	0.76	0.05	59	14